DYNAMIC MODELING OF EARTHQUAKE CYCLES ON COMPLEX FAULTS, SCENARIO EARTHQUAKES, AND OFF-FAULT DAMAGE

A Dissertation

by

DUNYU LIU

Submitted to the Office of Graduate and Professional Studies of
Texas A&M University
in partial fulfillment of the requirements for the degree of

DOCTOR OF PHILOSOPHY

Chair of Committee,	Benchun Duan
Committee Members,	David Sparks
	Judith Chester
	Mary Beth Hueste
Head of Department,	Michael Pope

December 2018

Major Subject: Geophysics

ABSTRACT

The dissertation is devoted to developments of numerical methodologies to simulate physical processes of various earthquake phenomena and their applications. In the first study, we develop a dynamic earthquake simulator based on finite element methods (FEM) to model dynamics of geometrically complex faults governed by the rate- and state- friction over multiple earthquake cycles. The simulator combines a dynamic FEM code EQdyna for the coseismic dynamic phase and a newly developed static FEM code EQquasi for the quasi-static phases of earthquake nucleation, post-seismic and inter-seismic processes. Both FEM codes are parallelized through MPI to speed up computations. The dynamic earthquake simulator includes fully dynamic rupture propagation and can handle complex fault geometry. Earthquake cycles on a 3D strike-slip fault with a bend are simulated.

In the second study, deterministic ground motions up to 0.5 Hz from a set of spontaneous dynamic ruptures of M_w 7.5 scenario earthquakes on a 160-km right-lateral seismic gap in North China Basin (NCB) have been simulated. Self-similar heterogeneous initial stresses on the fault and a high-resolution 3D velocity structure in NCB have been used. Self-similar stresses result in complex rupture behaviors such as jumped/triggered ruptures due to large stress variations. The directivity effect on peak ground velocity is significantly reduced by self-similar heterogeneous stresses, because of frequent acceleration and deceleration of rupture fronts. Basin induced surface waves from the four bowl-shape basins in the study area amplify and prolongate ground motions, particularly within the one between Tianjin and Beijing.

In the last study, dynamic ruptures of a 3D strike-slip fault with a bend are simulated. Drucker-Prager plasticity is applied to model the off-fault damage associated with stress heterogeneity induced by dynamic ruptures through a bend. Induced/reactivated shear mesoscale

subsidiary faults and microcracks indicated by the beach balls are associated with observed orientations of such features in the Northern Branch of the San Gabriel Fault. The numerical models confirm that dynamic ruptures through the bend will induce the prominent set of subhorizontal fractures at shallow depths near the bend. The direction of rupture propagation determines the locations of the subhorizontal fractures.

DEDICATION

To my dear wife and my loving parents, who have been a constant source of encouragement and support. To my new born baby boy, Jasper, who enlightens my life with the greatest excitement and joy.

ACKNOWLEDGEMENTS

I would like to thank my committee chair, Dr. Benchun Duan, and my committee members, Dr. Judith Chester, Dr. David Sparks, Dr. Mary Beth Hueste for their guidance and support throughout the course of my PhD research. I also want to thank Dr. Zenon Medina-Cetina for his generosity to review my dissertation and to attend my final defense.

Special credits should go to Dr. Benchun Duan, for his generous support, academically, emotionally, and financially, and his clear and straightforward guidance, and his patience to many discussions. Special thanks also go to my colleague Bin Luo, a talented PhD who works out many challenging numerical implementations and shares with me his thoughts and experiences generously.

Thanks go to my dear friends and graduate fellows and the department faculty and staff for making my time at Texas A&M University a great experience.

Finally, thanks to my mother and father for their support and encouragement, to my wife for her love and patience.

CONTRIBUTORS AND FUNDING SOURCES

This work was supported by a dissertation committee consisting of Dr. Benchun Duan, Dr. Judith Chester and Dr. David Sparks of the Department of Geology & Geophysics, and Dr. Mary Beth Hueste and Dr. Zenon Medina-Cetina of the Department of Civil Engineering.

All other work conducted for the dissertation was completed by the student independently.

The numerical implementation of the rate- and state- friction is helped by my colleague, Bin Luo.

Financially, the study in Chapter II is funded by SCEC Award 18220. The work in Chapter III is partially funded by the NSF grant EAR-1524743.

Technically, we appreciate Texas A&M High Performance Research Computing (http://hprc.tamu.edu/) for providing the advanced computing resources used in all the studies.

NOMENCLATURE

FEM	Finite Element Method
RSF	Rate- and State- Friction
SCEC	Southern California Earthquake Center
USGS	United States Geological Survey
NBSGF	North Brach of San Gabriel Fault
TSN	Traction-at-Split-Nodes
PML	Perfectly Matched Layer
CPS	Computer Program for Seismology
TJRS	Tian Jin Railway Station

TABLE OF CONTENTS

LIST OF FIGURES

Page

LIST OF TABLES

Page

CHAPTER I

INTRODUCTION AND OVERVIEW

The dissertation is devoted to developments of numerical methodologies to simulate physical processes of various earthquake phenomena and their applications to earthquake cycles on geometrically complex faults, ground motion from scenario earthquakes, and bend-induced off-fault damage.

Most disastrous earthquakes are reactivation of mature earthquake faults, whose stresses and slips are governed by frictional constitutive relationships, i.e., friction laws. In addition, faults in nature generally show fault geometrical complexities such as fault bends, step-overs and branches at all length scales. Analyses of past earthquake ruptures show that the complexities conditionally allow ruptures to pass through, leading to disastrous large earthquakes. Earthquake scientists use physics-based numerical models that incorporate friction laws to understand the key factors that control the details and extents of earthquake ruptures. With single-event dynamic rupture models, we understand the dynamic stress is critical to earthquake ruptures, such as in what conditions a rupture may continue through a fault bend or jump over a step-over. In the other scope of long-term earthquake cycle models, we acknowledge that stress heterogeneities induced by fault geometrical complexities and stress histories inherited from previous earthquakes may determine rupture patterns of a fault system. The rate- and state- friction law (RSF) is derived from rock experiments. It successfully unifies many earthquake phenomena, such as earthquake nucleation and post-seismic deformation, in its framework. Numerical models incorporating the RSF can model all phases of an earthquake cycle, especially the physically and mathematically sensible phase of earthquake nucleation. However, in the earthquake science community, there is still no such a software that can simulate earthquake

cycles of geometrically complex faults based on the RSF. In the Chapter II of the dissertation, we will present a Finite Element Method (FEM) and its software we have developed that tackles the challenge. We'll apply the FEM to a three-dimensional strike-slip fault with a bend.

After an earthquake occurs on a fault, seismic waves are radiated from the fault and poise seismic hazard to the cities and infrastructures they pass by. Ground motion simulations of scenario earthquakes (i.e., potential, disastrous earthquakes) on seismically active faults have become an important tool to assess seismic hazard mitigation in the recent decade. For example, the Shakeout-K and -D simulations are multidisciplinary collaborations led by USGS (U.S. Geological Survey) and SCEC (Southern California Earthquake Center) to predict strong ground motion in southern California from potential earthquakes on the southern San Andreas Fault. North China Basin (NCB) area stands in the same position as the Southern California with urgent attentions to seismic hazard on several active earthquake faults that are due to large earthquakes. In addition, deep sedimentary basins that can enhance and prolongate seismic shakings widely exist in NCB. In Chapter III of the dissertation, we'll present ground simulations of scenario earthquakes on a portion of Tangshan-Hejian-Cixian fault that passes through an economically and politically critical city, Tianjin. We build up the detailed 3D velocity structures that show several bowl shape basins. Peak ground velocities from several scenario realizations are presented and analyzed.

In Chapter IV, we will steer our attention back to single dynamic rupture of geometrically complex fault with the focus on off-fault damage and their links to geological observations of mesoscale subsidiary faults and microcracks in the damage zone of a mature fault. The idea comes from my involvement in the structural geology, petrology, and rock experiments that I have learned and benefited a lot during my four years stay in our Tectonophysics Center. Typical

fault zones of mature and large-displacement faults have a structure of fine granulated fault core that hosts the majority of earthquake slip and a damage zone of fractures ranging many scales. The debate of damage zone formation is between the arguments that it is formed by stress concentration induced at the rupture front and that the linkage of remaining joints and microcracks over the long-term maturing of the fault. Regardless of how the damage zone forms, under the framework of continuum mechanics, the fractures in the damage zone can be modeled as inelastic/plastic deformation, i.e., off-fault plasticity often used in numerical modeling literature. Because stress heterogeneities are associated with fault geometrical complexities in dynamic ruptures, it is necessary to examine the features of off-fault plastic deformation induced by such stress heterogeneities and their links to geologic field observations, both of which are lacking in the earthquake science community. Geological field observations of mesoscale subsidiary faults and microcracks associated with earthquake ruptures and numerical dynamic rupture models of elastoplastic mechanics demonstrate that the dynamic stress change during an earthquake usually surpasses the yield strength of rocks surrounding the fault. It leads to irrecoverably plastic deformation. The magnitude of such plastic deformation becomes larger when a fault geometrically complexity is present. Orientations of such plastic deformation could have implications to the rupture histories on faults. We use dynamic rupture models with off-fault plasticity to study the parameters that control the magnitude and orientations of such plastic strains of a 3D strike-slip fault with a bend. The fault structure is conceptualized from the Northern Branch of San Gabriel Fault (NBSGF), where thorough structural-geological and petrological analyses on mesoscale subsidiary faults and microstructures in the damage zone have been carried out. The key parameters identified to have critical impacts on the pattern of off-fault plastic strain is the angle between the maximum principle compressive stress relative to

the fault strike and the direction of rupture propagation. The study serves as a bridge between numerical models and geological field observations. It also provides a means to uncover the histories of past earthquakes near a fault bend.

CHAPTER II

A FEM-BASED DYNAMIC EARTHQUAKE SIMULATOR FOR GEOMETRICALLY COMPLEX FAULTS WITH RSF

2.1 Introduction

The magnitude of an earthquake and its seismic hazard are generally proportional to the total length of the earthquake rupture (Romanowicz, 1992, Hanks and Bakun, 2008, Hanks and Bakun, 2002, Somerville, 2006). Geological mapping of continental earthquakes has shown faults are generally segmented by geometrical complexities such as step-overs, bends or gaps, which play controlling roles in terminating ruptures or conditionally allowing ruptures to pass through (Wesnousky, 2006, Biasi and Wesnousky, 2016, Wesnousky, 2008). It is desired in seismic hazard analysis to incorporate physics-based models to understand the factors and their conditions that determine when a geometrical complexity, conceptualized as earthquake gates (Oskin et al., 2015), to impede a rupture propagation or to allow one to pass through. Geologic observations of fault maps of past earthquakes reveal that the statistical distribution of passing ratio of ruptures as functions of the extents of geometrical complexities, such as angles of fault bends (Biasi and Wesnousky, 2017). Single-event dynamic rupture models demonstrate the necessity to apply fully dynamic physics-based models to assessing whether a dynamic rupture can jump a step-over or a bend (Harris and Day, 1993, Lozos et al., 2011, Oglesby, 2008). Earthquake cycle simulations of geometrically complex fault show that strong stress heterogeneities can be induced by the fault geometric complexity of a fault bend, a step-over, and a fault branch (e.g., Duan and Oglesby, 2005, Duan and Oglesby, 2006, Duan and Oglesby, 2007). The stress heterogeneity affects dynamics of the following earthquakes. A big uncertainty in applying single-event dynamic rupture models is the setting of initial stresses on earthquake

faults. Under the framework of multicycle earthquake simulation, however, the long-term stress histories and earthquake event patterns associated with fault geometrical complexities can be evaluated. A fully dynamic earthquake cycle model helps to understand the physics governing the statistical distribution of passing ratio of ruptures as functions of bend angles as observed in fault maps of past earthquakes. In addition, the incorporation of physics-based models in probabilistic seismic hazard models will enhance its predictive potential.

Different approaches to model dynamics of earthquake cycles have been proposed (Tse and Rice, 1986, Duan and Oglesby, 2005, Lapusta et al., 2000, Lapusta and Liu, 2009). Lapusta et al. (2000), based on previous efforts (Tse and Rice, 1986), develop a boundary integration methodology to capture transient co-seismic dynamics, slow tectonic inter-seismic loading and extremely sensitive earthquake nucleation, implementing experimentally-derived RSF law (Dieterich, 1979, Ruina, 1983). Lapusta et al. (2000) propose a variable time stepping scheme to evolve fault slips and discuss numerical resolutions to properly resolve the underlying physical processes in detail. However, their applications are limited to planar vertical strike-slip faults. To take fault geometrical complexities into account, Duan and Oglesby (2005) develop a Finite Element Method (FEM) to model earthquake cycles on 2D strike-slip fault with a bend (Duan and Oglesby, 2005), with a step-over (Duan and Oglesby, 2006), and with a branch (Duan and Oglesby, 2007). The FEM has an advantage to model irregular fault geometries. They combine a dynamic rupture model for co-seismic ruptures with an analytical viscoelastic solution to mimic the tectonic inter-seismic and post-seismic deformations. The nucleation of an earthquake is determined by the Coulomb Failure Criteria in a fault patch whose size is pre-determined. Later on, Lapusta and Liu (2009) extend their methodology to three-dimensional planar vertical faults.

They discuss in detail the crucial numerical resolutions to properly model the physical processes of an earthquake cycle.

The privileges of using the RSF to model earthquake cycles are that 1) the friction law is derived from rock experiments and 2) its ability to model all phases of deformation in an earthquake cycle including co-seismic dynamic rupture, post-seismic deformation, inter-seismic tectonic loading and the sensitive nucleation. However, to use the RSF to simulate earthquake cycles of 3D geometrically complex fault systems is very challenging in terms of numerical implementation of the RSF in the FEM framework and enormous computational costs. An earthquake cycle typically involves co-seismic dynamic rupture and complex quasi-static deformation of post-seismic, inter-seismic and nucleation phases (Scholz, 2002, Lapusta and Liu, 2009). Quasi-static deformation phases may alter stresses and other initial conditions and determine the locations of earthquake nucleation (Lapusta and Liu, 2009). The numerical model has to handle many orders of magnitudes of temporal and spatial scales involved in the physical processes. For instance, the inter-seismic deformation may last hundreds of years, while the dynamic co-seismic rupture is counted in seconds. In terms of spatial scales, the spatial discretization should be fine enough to resolve the cohesive zone at the front of rupture (Day et al., 2005), say, hundreds of meters, while the model needs to host an earthquake fault measured in tens to hundreds of kilometers.

2.2 Methodology: The FEM earthquake cycle simulator

We develop a finite element method (FEM) earthquake cycle simulator to model multicycle dynamics of three-dimensional geometrically complex fault systems in the framework of the rate- and state- friction law. The simulator combines EQdyna (Duan, 2010, Duan and Oglesby, 2005, Duan et al., 2017) to simulate co-seismic dynamic ruptures and a newly

developed EQquasi to simulate quasi-static deformations of nucleation, post-seismic and inter-seismic processes of an earthquake cycle. EQdyna and EQquasi are switched through on-fault physical quantities of shear and normal stresses, slip-rates and state variables defined in the RSF. EQquasi is called for when a criterion is met that inertia forces of fault rocks can be reasonably negligible to quasi-statically model the nucleation, post- and inter-seismic phases. Otherwise, EQdyna will be applied to simulate co-seismic dynamic ruptures. The two-code scheme shows advantages to reconcile the computational challenges from different deformation phases of an earthquake cycle. The challenges are mainly related to handling time steps ranging from hundredths of a second to a few years based on the variable time stepping scheme (Lapusta et al., 2000, Lapusta and Liu, 2009) and to using element size small enough to resolve the cohesive zone at the rupture front of dynamic ruptures (Day et al., 2005). In addition, we need carefully choose the model size to ensure no undesired interactions between model boundaries and the earthquake fault. It usually results in at least a few million hexahedral elements for a moderate size of an earthquake fault, say, 30 km in length and 15 km in dip.

2.2.1 EQdyna: FEM to simulate co-seismic rupture dynamics

We use an explicit FEM EQdyna (Duan and Day, 2008, Duan, 2010, Duan, 2012, Duan and Oglesby, 2006, Duan et al., 2017, Liu and Duan, 2018) to simulate dynamic rupture and seismic wave propagation in this study. Three-dimensional versions of EQdyna, including the hybrid MPI/OpenMP parallel version (Duan, 2010, Liu and Duan, 2018), have been validated against benchmark problems of the SCEC/USGS Spontaneous Rupture Code Verification Project (Harris et al., 2009, Harris et al., 2011, Harris et al., 2018a). EQdyna features an under-integrated hexahedral element stabilized by hourglass control (Kosloff and Frazier, 1978). With the explicit central difference time integration, the method has been proved to be efficient and accurate in

simulating spontaneous rupture and seismic wave propagation. The traction-at-split-node (TSN) scheme of Day et al. (2005) is adopted to treat the faulting boundary in EQdyna (Duan, 2010). The Perfectly Matched Layer (PML) (e.g., Collino and Tsogka, 2001, Ma and Liu, 2006) has been implemented in EQdyna to make model sizes more economic by effectively absorbing reflections from model boundaries (Liu and Duan, 2018). The RSF has been implemented in the EQdyna (Luo and Duan, 2018) and is validated against benchmarks TPV 103 and TPV 104 in the SCEC/USGS Code Verification Project.

2.2.2 EQquasi: FEM to simulate the quasi-static processes of an earthquake cycle

For other phases of an earthquake cycle, the time step will be far larger than hundredths of a second required to stabilize an explicit FEM. Therefore, we develop a FEM EQquasi to simulate quasi-static deformations of nucleation, post- and inter-seismic phases. EQquasi features fully integrated hexahedral elements, which do not require hourglass control. It adopts highly efficient parallel sparse linear solvers PARDISO (Petra et al., 2014b, Petra et al., 2014a) and MUMPS (Amestoy et al., 2001, Amestoy et al., 2006) to solve equations for the finite element system. Faults are treated as an essential boundary condition using the TSN technique (Day et al., 2005).

The switch between EQquasi and EQdyna is determined by $dt_{evol} = ndt$, where dt_{evol} is the variable time step calculated by the formula proposed by Lapusta et al. (2000), dt is the time step for dynamic ruptures and is a fraction of element size divided by maximum P-wave velocity in the model, and n is a whole number (the default is 5). In EQquasi, when dt_{evol} falls below ndt , EQquasi is terminated and EQdyna starts. EQdyna runs with time step as dt. After EQdyna, EQquasi starts with dt_{evol} calculated from the maximum sliprate in the model. On-fault physical quantities including normal and shear stresses, slip-rates, and state variables are

transferred to continue the simulation. The switching process has been automated through the batch system on Texas A&M University High Performance Computing clusters to model any number of earthquake cycles.

2.2.3 Numerical implementation of the RSF in EQquasi

After spatial discretization of the finite element model, the system is expressed as

$$\mathbf{M}\mathbf{A}^{t+1} + \mathbf{K}\mathbf{U}^{t+1} = \mathbf{F}^{t+1} \quad (1)$$

Based on the switch criterion, during quasi-static deformation, slip velocities of fault nodes are generally very slow, indicating negligible inertia forces of fault masses comparing to elastic force from deformation induced by fault slip. As a result, the inertia term $\mathbf{M}\mathbf{A}^{t+1}$ in equation (1) can be omitted and equation (1) becomes

$$\mathbf{K}\mathbf{U}^{t+1} = \mathbf{F}^{t+1} \quad (2)$$

Since the fault split nodes are controlled by the RSF, the tractions that work on two fault walls will be a function of slip velocity $\mathbf{V}^{t+1}$ and state variable $\boldsymbol{\varphi}^{t+1}$, as expressed in the following equation (3),

$$\mathbf{F}^{t+1} = A * (\mathbf{T}_c^{t+1}(\mathbf{V}^{t+1}, \boldsymbol{\varphi}^{t+1}) - \mathbf{T}_0^{t+1}) \quad (3)$$

where A is the fault area represented by each pair of fault nodes, $\mathbf{T}_c^{t+1}$ and $\mathbf{T}_0^{t+1}$ are frictional resistance calculated by the RSF and shear traction on the fault at the beginning of time step t+1, respectively. By solving equations (2) and (3), the on-fault velocities $\mathbf{V}^{t+1}$, state variables $\boldsymbol{\varphi}^{t+1}$ and displacements $\mathbf{U}^{t+1}$ will be obtained. These on-fault $\mathbf{U}^{t+1}$ will serve as Dirichlet boundary to update the $\mathbf{U}^{t+1}$ and $\mathbf{V}^{t+1}$ for the whole model. If we adopt $\mathbf{U}^{t+1} = \mathbf{U}^t + \mathbf{V}^{t+1}dt$, both sides of equation (2) will involve $\mathbf{V}^{t+1}$, it becomes computationally expensive to solve the non-linear problem involving the stiffness matrix of the whole model. In addition, combining the elastic system of the finite element model and the RSF system will yield inaccurate results due to the

significant difference between their 'stiffness' (Rojas et al., 2009). Therefore, in each time step of computing the elastic Finite Element system, we solve equation (3) for individual pair of fault split nodes. In practice, we use $\widetilde{\mathbf{U}}^{t+1} = \mathbf{U}^t + \mathbf{V}^t dt$ to estimate $\mathbf{U}^{t+1}$ and equate trial elastic forces $\mathbf{K}\widetilde{\mathbf{U}}^{t+1}$ to $\mathbf{F}^{t+1}$ to get estimations of $\mathbf{V}^{t+1}$.

We have largely followed the scheme of Lapusta et al. (2000) to advance the on-fault quantities in each time step that proceeds as follows:

(a), when the switch criterion is reached, terminate EQquasi and transfer necessary on-fault quantities to EQdyna and start the dynamic rupture using EQdyna; otherwise continue the simulation using EQquasi;

(b), determine the time step to advance based on $dt_{evol} = \varepsilon\, {}^{L}/_{\max(sliprate)}$, in which ε is a fraction of 1, L is the critical slip distance in the RSF; we use $\varepsilon = 0.2$ in our simulations, even though $\varepsilon < 1/3$ is claimed to yield consistent results (Lapusta and Liu, 2009);

(c), make first predictions of displacements for time step t+1 based on known values from the last time step, using $\widetilde{\mathbf{U}}^{t+1} = \mathbf{U}^t + \mathbf{V}^t dt_{evol}$ and $\widetilde{\boldsymbol{\varphi}}^{t+1} = \boldsymbol{\varphi}^t + \dot{\boldsymbol{\varphi}}^t dt_{evol}$;

(d), make first predications of elastic force $\tilde{\mathbf{F}}^{t+1} = \mathbf{K}\widetilde{\mathbf{U}}^{t+1}$ and $\tilde{f}_i$ represents $\tilde{\mathbf{F}}^{t+1}$'s i^{th} individual element; by doing so, we separate the elastic Finite Element system and the RSF system. It allows us to solve sliprate $\tilde{V}_i^{t+1}$ for each pair of split nodes i, according to equation (3) or equivalently

$$\tilde{f}_i = A * \left(T_c^{t+1}\left(\tilde{V}_i^{\,t+1}, \tilde{\varphi}^{t+1} \right) - T_0^{t+1} \right) \qquad (4)$$

once $\tilde{V}_i^{t+1}$ is obtained, $\tilde{\dot{\varphi}}^{t+1}$ can be handily computed by

$$\tilde{\dot{\varphi}}^{t+1} = Aging\ law\left(\tilde{V}_i^{\,t+1}, \tilde{\varphi}^{t+1} \right) \qquad (5)$$

(e), compute the final predictions of slip and state variables using $\tilde{\tilde{U}}^{t+1} = U^t + \left(V^t + \tilde{V}_i^{t+1}\right)dt_{evol}/2$ and $\tilde{\tilde{\varphi}}^{t+1} = \varphi^t + \left(\dot{\varphi}^t + \tilde{\dot{\varphi}}^{t+1}\right)dt_{evol}/2$;

(f), make new predications of elastic forces $\tilde{\tilde{\mathbf{F}}}^{t+1} = \mathbf{K}\tilde{\tilde{\mathbf{U}}}^{t+1}$ and $\tilde{\tilde{f}}_i$ represents $\tilde{\tilde{\mathbf{F}}}^{t+1}$'s i^{th} individual element; using the predictions $\tilde{\tilde{f}}_i$ and $\tilde{\tilde{\varphi}}^{t+1}$ to get $\tilde{\tilde{V}}^{t+1}$ and $\underset{\sim}{\tilde{\varphi}}^{t+1}$ following equations (6) and (7):

$$\tilde{\tilde{f}}_i = Area * \left(T_c^{t+1}\left(\tilde{\tilde{V}}_i^{\,t+1}, \tilde{\tilde{\varphi}}^{t+1}\right) - T_0^{t+1}\right) \tag{6}$$

$$\tilde{\dot{\varphi}}^{t+1} = Aging\ law\left(\tilde{\tilde{V}}_i^{\,t+1}, \tilde{\tilde{\varphi}}^{t+1}\right) \tag{7}$$

(g), claim the final displacements, state variables and slip-rates at time step t+1 as $U^{t+1} = U^t + \left(V^t + \tilde{\tilde{V}}_i^{t+1}\right)dt_{evol}/2$, $\varphi^{t+1} = \varphi^t + \left(\dot{\varphi}^t + \underset{\sim}{\tilde{\varphi}}^{t+1}\right)dt_{evol}/2$ and $V_i^{\,t+1} = \tilde{\tilde{V}}_i^{\,t+1}$, respectively;

(h), go back to step (a).

2.3 Models, Parameters, and Numerical resolutions

2.3.1 Model and fault geometry

Before we march on to simulate earthquake cycles on geometrically complex faults with the simulator, we first model fault dynamics on a 3D vertical planar strike-slip fault that contains a potentially seismogenic region with a steady state velocity-weakening feature surrounded by a steady state velocity-strengthening region, as shown in Figure 2.1a. We'll show our simulation of a similar model to Lapusta and Liu (2009)'s three-dimensional planar strike-slip fault to qualitatively validate the correctness of the earthquake simulator. Then, we simulate earthquake cycles on a 3D strike-slip fault with a bend as sketched in Figure 2.1b. The bend in the context refer to the portion of fault where a change in strike takes place. The left segment and the right segment are as indicated in Figure 2.1b and 2.1c. The left segment is parallel to the far-field tectonic loading, while the right segment, whose strike deviates $10\,°$ from the left segment, is compressed slightly by the tectonic loading. The dimensions of both the vertical planar fault and

the fault with a bend are 60 km along the strike (x axis) and 30 km in the dip (z axis). The coordinate system of the Finite Element models is given in Figure 2.1b. We design three models with the bend: M11, M07 and M11v. In M11 and M07, the critical slip distances L in the RSF are 11 mm and 7 mm, respectively. The reference friction f_0 in the RSF is 0.6 on the whole fault. In M11v, parameters are the same as those in M11 except that the reference friction is calculated as the ratio of initial shear stress divided by initial normal stress.

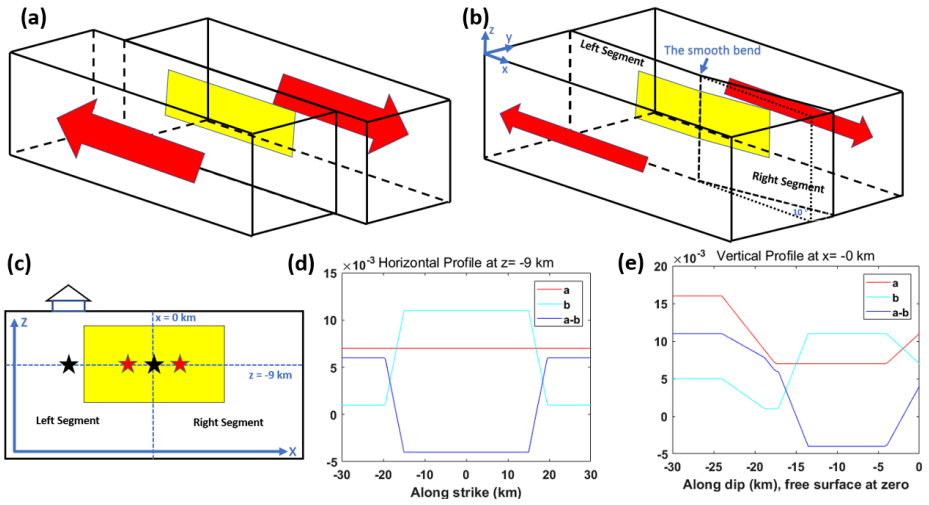

Figure 2.1 (a) The schematic diagram of the vertical planar strike-slip fault model. The tectonic loading is applied on boundaries with red arrows indicating directions of movements, which gives rise to a right-lateral sense of slip. The interface between two blocks is the fault. The shaded area is velocity weakening region. The rest of the fault region is velocity strengthening. (b) The schematic diagram of the strike-slip fault with a 10° smooth bend. The location of the smooth bend and the coordinate system of the Finite Element model are shown. Other setups are the same as in (a). (c) The fault plane in (a) or the projection of the fault plane onto the surface parallel to the left segment in (b). The shaded area is velocity weakening region with the rest of the fault velocity strengthening. For the strike-slip fault with a bend, the left segment and the right segment are shown in the panel (c). Two dashed lines are profiles to show frictional parameter distributions at x=0 km (panel d) and z=-9 km (panel e), respectively. Stars stand for on-fault stations, on which time series results will be presented. (d) Distributions of frictional parameter *a*, *b*, and *a-b*, defined in the RSF, along the horizontal profile along z = -9 km in (c). (e) Distributions of frictional parameter *a*, *b*, and *a-b* along the vertical profile along x = 0 km in (c).

We adopt different model sizes for co-seismic dynamic rupture using EQdyna and quasi-static deformations using EQquasi. Because the element size is restricted to be less than a few hundred meters given frictional parameters from rock experiments, the main goal is to use as small model size as possible to reconcile the computational challenges arising from various phases of deformation in an earthquake cycle. We'll discuss in detail the necessary element size to resolve physical processes in Section 2.2.3 Crucial Numerical Resolutions. In this section, we'll focus on limitations on choosing the model size.

In co-seismic dynamic ruptures, there are two limitations on the model size. First, fault slip generally reaches the magnitude of meters, which requires the model boundaries being far enough away from the earthquake fault. For example, to simulate dynamic ruptures on a fault of 60 km in length by 30 km in dip, the model boundaries should be extended at least 30 km from the fault in all directions based on trial simulations. Otherwise, the boundary conditions where far-field tectonic loading is applied may contaminate the solutions on the fault. Second, we want to avoid undesired wave reflections from model boundaries in the time window we simulate. With the Perfectly Matched Layer absorbing boundary (Liu and Duan, 2018), we can simulate 100 seconds of co-seismic dynamic ruptures without making the model too big. A model of 120 km by 120 km by 60 km in the x, y, z directions, respectively, is appropriate. Given the element size of 300 m, there are 32 million hexahedrons in the model. If the element size is reduced to 200 m, the number of total elements jumps to 108 million.

Ideally, we want to use the exact model to simulate quasi-static deformations with EQquasi. However, it proves extremely challenging given the current computational capacity of EQquasi even after parallelization. As discussed in the Section 2.1.3, in quasi-static deformation

phases, the inertia term is neglected due to low slip-rates on the fault. Therefore, we need to solve the equations of the linear system of the Finite Element model expressed in Equation (2). EQquasi currently adopt parallel sparse linear solver PARDISO (using OpenMP on shared memory infrastructure) or MUMPS (using MPI on distributed computing clusters) to complete the computation. We can process 2 million hexahedrons with 100 MPI (Message Passing Interface) processes with ease. But, to handle 32 million hexahedrons is still out of our capacity. However, there are two factors that make an adoption of a smaller model with EQquasi possible. First, we apply tectonic loading on boundaries of two blocks as shown in Figure 2.1a and 2.1b. The interface between the blocks – the fault – slips at low slip-rates governed by the RSF. According to this setup, the slips on the fault and stresses in the volume are solutions from boundary tectonic loading. We can apply a smaller model if we adjust strain rate in the volume to fit geodetic observations. The second factor is that there is negligible wave propagation. Therefore, the model in EQquasi is from -30 to 30 km in the strike direction (x), -30.19 to 30.19 km in strike-perpendicular direction (y), and from -30 to 0 km in the vertical direction (z). The fault is the interface between two moving blocks (y = 0) that penetrates the model, as shown in Figure 2.1a and 2.1b.

In terms of the boundary conditions of quasi-static models, because the dominant displacement in the model is along the strike, we apply $\pm 9.513 \times 10^{-10}\, m/s$ on the maximum and minimum y boundaries along the strike but free all other surfaces, as shown by the red arrows in Figure 2.1b. The applied velocities yield an along-strike shear strain loading rate at 1 μ/yr in the model. Results show the normal displacements on the maximum y, the minimum y and the bottom surfaces are negligible. Therefore, we do not constrain the normal displacements on those surfaces. The boundary conditions are essentially the same as the one applied in

Aagaard et al. (2013). Given such a model size and 300 m on-fault element size, the model contains 0.64 million hexahedrons. With 200 m on-fault element size, the number increases to 1.8 million. Both cases involve a 1.3 enlarging ratio along the fault-perpendicular direction to gradually increase the element size starting from 1.2 km away the fault surface.

2.3.2 Parameters in RSF

Depth-dependent frictional parameters a and b are set up in a similar multi-linear manner as in Lapusta and Liu (2009). We use slightly smaller a and b in the velocity weakening region to make a 300 m element size properly resolve the cohesive zone at the front of dynamic ruptures. In addition, we linearly reduce b along the strike when abs(x) > 15 km to arrest the dynamic rupture spontaneously. A velocity strengthening region at shallow depth is present. a and b are uniform in the majority portion of the velocity weakening region on the fault and their values are given in Table 2.1. Distributions of a, b, and a-b along a horizontal profile at z = -9 km and along a vertical profile at x = 0 km are provided in Figure 2.1d and 2.1e, respectively.

We choose the critical slip distance L in the RSF to be 11 mm over most of the fault. L (also denoted as d_c or D_c in the literature) can be interpreted as the slip distance for the fault to evolve to the steady state. It is linearly increased from the 4 km depth to the free surface at shallow depth to represent unconsolidated rocks or soft sediments showing velocity strengthening behavior. Initial normal stress and shear stress are -50 MPa (tensile positive) and 30 MPa, respectively, for the planar fault model. The stresses are resolved from a uniform regional stress field with $\sigma_1 = 80$ MPa, $\sigma_3 = 20$ MPa and σ_1 at a $45°$ to the planar fault or the left segment of the fault with a bend. Rock density, P-wave velocity, and S-wave velocity are 2670 kg/m^3, 6000 m/s, and 3464 m/s, respectively. Other important parameters are summarized in Table 2.1.

Table 2.1 Fault geometry, material properties and friction parameters in M11.

Fault length along strike	FS	60 km
Fault depth	FD	30 km
Velocity-weakening (VW) region, length	L_{seis}	30 km
Velocity-weakening (VW) region, width	W_{seis}	15 km
Minimum slip-rate	V_{min}	10^{-12} m/s
S wave velocity	V_s	3464 m/s
P wave velocity	V_p	6000 m/s
Density	ρ	2670 kg/m^3
Reference slip velocity	V_0	10^{-6} m/s
Reference friction coefficient	f_0	0.6
Rate- and state- parameters in the VW region	b	0.011
	a	0.007
Normal stress on the planar segment	σ_n	-50 MPa
Shear stress on the planar segment	τ	30 MPa
Critical slip distance in the RSF	L	11 mm/ 7mm
On-fault element size of FE models	dx	300 m / 200m
Minimum time step	dt	0.02 s / 0.015 s

2.3.3 Crucial Numerical Resolutions

There are two important spatial resolutions to resolve in earthquake cycle simulations, h^*/W_{seis} and Λ_0/dx, as defined in Lapusta and Liu (2009). h^* is the size of nucleation patch. W_{seis} is the width of seismogenic zone. Λ_0 is the width of cohesive zone at the rupture front with

a zero propagating speed. dx is the element size. h^* and Λ_0 are functions of normal stress σ_n, rock shear modulus μ^* (we use μ^* for Mode III shear cracks), and frictional parameters a, b, L in the RSF, as shown in equations (8) and (9). Equations (8) and (9) are equations (16) and (20), respectively, in Lapusta and Liu (2009). C_1 is a constant that equals to $9\pi/32$ if the stress is linearly distributed within the cohesive zone.

$$h^* = \left(\frac{\pi}{2}\right) * {\mu^* bL}\Big/{(b-a)^2\sigma_n} \tag{8}$$

$$\Lambda_0 = C_1 * {\mu^* L}\Big/{b\sigma_n} \tag{9}$$

First, the size of the nucleation patch should be less than the shorter dimension of fault, W_{seis}, to induce unstable slips, which means that $h^*/W_{seis} < 1$. Second, the element size should be small enough to resolve rapid changes of stresses and slip-rates in the cohesive zone at the rupture front (Lapusta and Liu, 2009, Day et al., 2005). Lapusta and Liu (2009) simulate earthquake cycles of a model (L = 8 mm case) using dx of 50, 100, 200, and 400 m, respectively. They conclude that dx = 100 m yields indistinguishable results from dx = 50 m, while results computed using dx = 200 m deviate from those of dx = 100 m. Based on their parameters and conclusion, we reckon a criterion that $\Lambda_0/dx > 2.3$ for proper numerical resolution. In Table 2.2, we provide key parameters and ratios of our models and the model with 100 m element size and L = 8 mm in Lapusta and Liu (2009). We carefully choose our parameters and element size to meet the criterion.

Table 2.2 Parameters and critical ratios of the model of dx = 100 m and L = 8 mm in *Lapusta and Liu (2009)* and our models.

	a	b	L mm	Dx m	Vp m/s	Vs m/s	ρ Kg/m^3	Λ_0/dx	h^* $/W_{seis}$
L&L09	0.015	0.019	8	100	5196.2	3000	2670	2.384	0.8173
M11[1]/M11v[2]	0.007	0.011	11	300	6000	3464	2670	2.5163	0.8674
M07[3]	0.007	0.011	7	200	6000	3464	2670	2.4019	0.5520

[1] M11 stands for the model with L = 11 mm.

[2] M11v has the same parameters as the M11 does except that the reference friction coefficient is computed by dividing the initial shear stress by the normal stress rather than a constant 0.6.

[3] M07 stands for the model with L = 7 mm.

2.3.4 A smooth bend

In previous studies of a 2D fault with a bend (Duan and Oglesby, 2005, Lozos et al., 2011), the bend is modeled by a sharp change of strike over one or two elements. As shown in Duan and Oglesby (2005), slips around a bend will reduce normal and shear stresses on the left segment of bend and increase those on the right segment of the bend. (The model geometry and terminologies are the same in their models and ours.) The more abrupt the change in strike, the higher magnitude of stress heterogeneity. Over earthquake cycles, the pure elastic model will produce pathological stress levels around the bend, which may be relieved by including viscoelasticity in the inter-seismic deformations. The abrupt change of strike at a fault bend over a few hundred meters may not be necessarily true in nature because the severely high stress heterogeneity may not promote the development or retaining of such a structure. Therefore, we propose a smooth bend structure in which the strike of the fault gradually changes over one to

two kilometers. It is mathematically described using the spline function. Figure 2.2 shows a close view of the smooth bend structure where the change of strikes takes place. Arrows are normal vectors calculated with spline function as well. We will see later the introduction of the smooth bend structure allows us to capture the stress heterogeneity around the bend without pathological stress level buildup over many earthquake cycles.

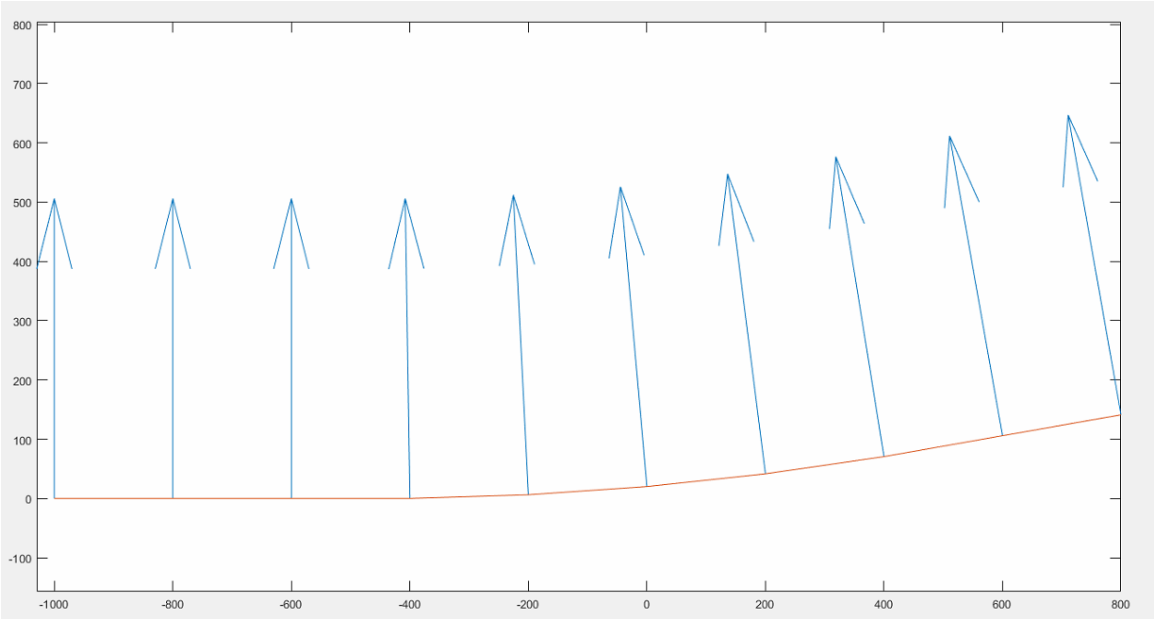

Figure 2.2 A smooth bend where the change of fault strikes takes place. The element size dx is 200 m in this case. The coordinates of the points at x=-1000, x=-800, x=-600 are predetermined following a straight line that strikes at 0°. The points at x=400, x=600 are predetermined to follow the other straight line that strikes at 10°. The two lines will intersect at x=0 and y=0 if extended. Coordinates at x=-400, x=-200, x= 0, x=200 are interpolated based on the cubic spline function. Arrows are normal vectors to the local strike at the fault nodes. They are calculated based on the spline function as well. The change of strike takes place smoothly over 5 elements of 1 km length. In the case of dx = 300 m, the change of strikes will take place over 1.5 km.

2.4 Results

2.4.1 Earthquake cycles on the planar fault

We first simulate earthquake cycles on a planar vertical strike-slip fault, whose geometry is shown in Figure 2.1a. The fault plane is sketched in Figure 2.1c, in which the shaded region is governed by velocity-weakening feature and the surrounding region velocity-strengthening. The initial slip-rate is uniform on the whole fault as 10^{-9} m/s. The simulation starts by applying tectonic loading on boundaries as indicated by red arrows in Figure 2.1a. A difference between our model and Lapusta and Liu (2009)'s models is that we do not prescribe a bottom loading of fixed slip-rates. Because we apply tectonic loading along far-field boundaries, the slip-rates on the whole fault including the velocity weakening and velocity strengthening regions are solutions from the coupled Finite Element and the RSF systems.

Physical quantities including slip-rate, shear stress and accumulated slips at two on-fault stations (black stars in Figure 2.1c) are presented in Figure 2.3 for the first 10 events. Stations are located at the center of velocity weakening region (solid lines) and the edge of velocity strengthening region (dashed lines), respectively. Earthquakes occur about every 30 years in the fault system as simulated. The station at the center of velocity weakening region slips at about 1 m/s in dynamic ruptures and quickly changes to the 'locked' status at 10^{-12} m/s for the majority time of an earthquake cycle. Approaching the nucleation phase, the slip-rate may build up in a time window of a few weeks. The station at the edge of velocity strengthening region show a totally different behavior. The fault creeps at 10^{-9} m/s for most of an earthquake cycle, unless a dynamic rupture penetrates the velocity strengthening region, which lifts the slip-rate at the station to ~1 m/s that quickly returns to the creeping sliprate. The difference can be readily seen in the third panel of accumulated slip. The station in the velocity weakening region accumulates

slips in a staircase manner, while the station in the velocity strengthening zone keeps creeping. The features qualitatively match the results shown in the Figure 3 of Lapusta and Liu (2009).

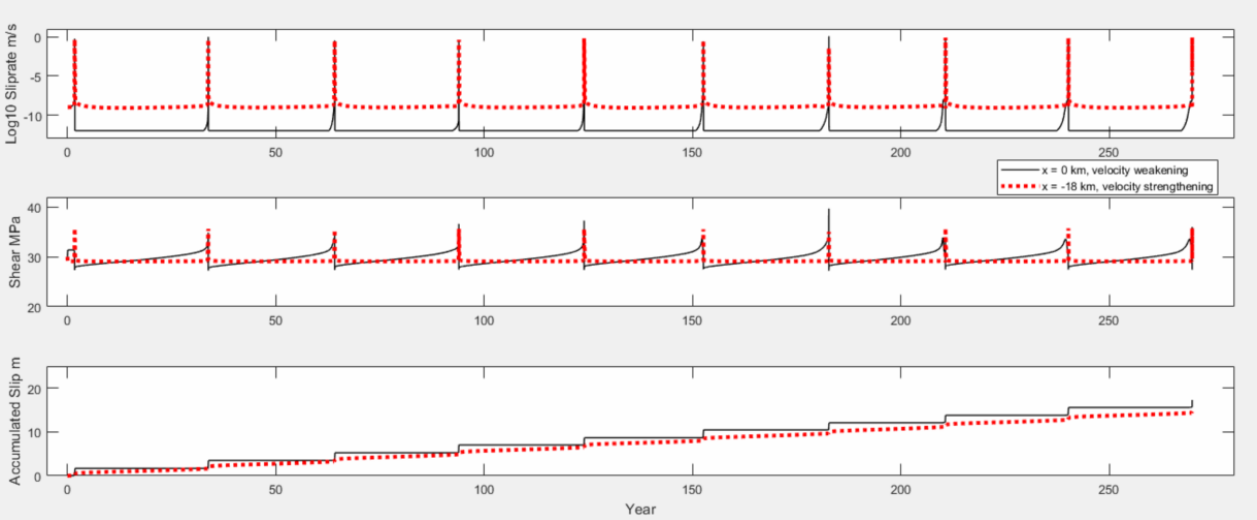

Figure 2.3 Slip-rate, shear stress, and accumulated slip histories of two on-fault stations at the velocity weakening (solid lines) and the velocity strengthening (dashed lines) regions, respectively. The locations of stations are x = 0 km and z = -9 km and x = -18 km and z = - 9 km, respectively. Their locations are also shown as black stars in Figure 2.1c.

Figure 2.4 presents accumulated slips from the 7th to the 21st events along the horizontal profile at the z = -9 km depth. Besides slightly different frictional parameters, we initiate the simulation from an uniform stress condition rather than introducing a patch of higher initial shear stress as in the models in Lapusta and Liu (2009). Because of the symmetry of fault geometry, initial stresses and frictional parameters, the first few earthquakes' nucleation patches are symmetric about the x = 0 km axis. The symmetric pattern of the nucleation patches is broken after a few events and the nucleation patches start to migrate over the fault. Among the 14 events shown, we see a 7-event pattern, that contributes ~10 m accumulates slips. The pattern starts with the first event nucleating close to the left edge of the fault. It is followed by three events

nucleating on the right portion of the fault. Then, the 5^{th} event nucleates at the center of the fault, which is followed by an event nucleating relatively to the right side. The last event nucleates, again, at the center of the fault. The pattern repeats once.

Erickson and Day (2016) find a similar breakup of symmetry in their two-dimensional models with uniform and symmetric initial stress conditions. They attribute the phenomenon to numerical errors and sensitive reaction of the RSF to such errors. They introduce a slight perturbation (10^{-6}) in the initial state variable and find the mono-material case with symmetric uniform initial condition is very sensitive to such perturbation. However, after including bi-material, a kind of heterogeneity, their simulation results stabilize. Because the focuses of this work are the implementation of Finite Element simulator for earthquake cycle dynamics and its application on geometrically complex fault, the stress heterogeneity induced by the smooth bend will predominantly control the dynamics of the system. The earthquake cycle simulation of the planar fault system only serves to qualitatively validate correct implementation of the simulator to capture all deformation phases in an earthquake cycle by comparisons with a similar model in Lapusta and Liu (2009).

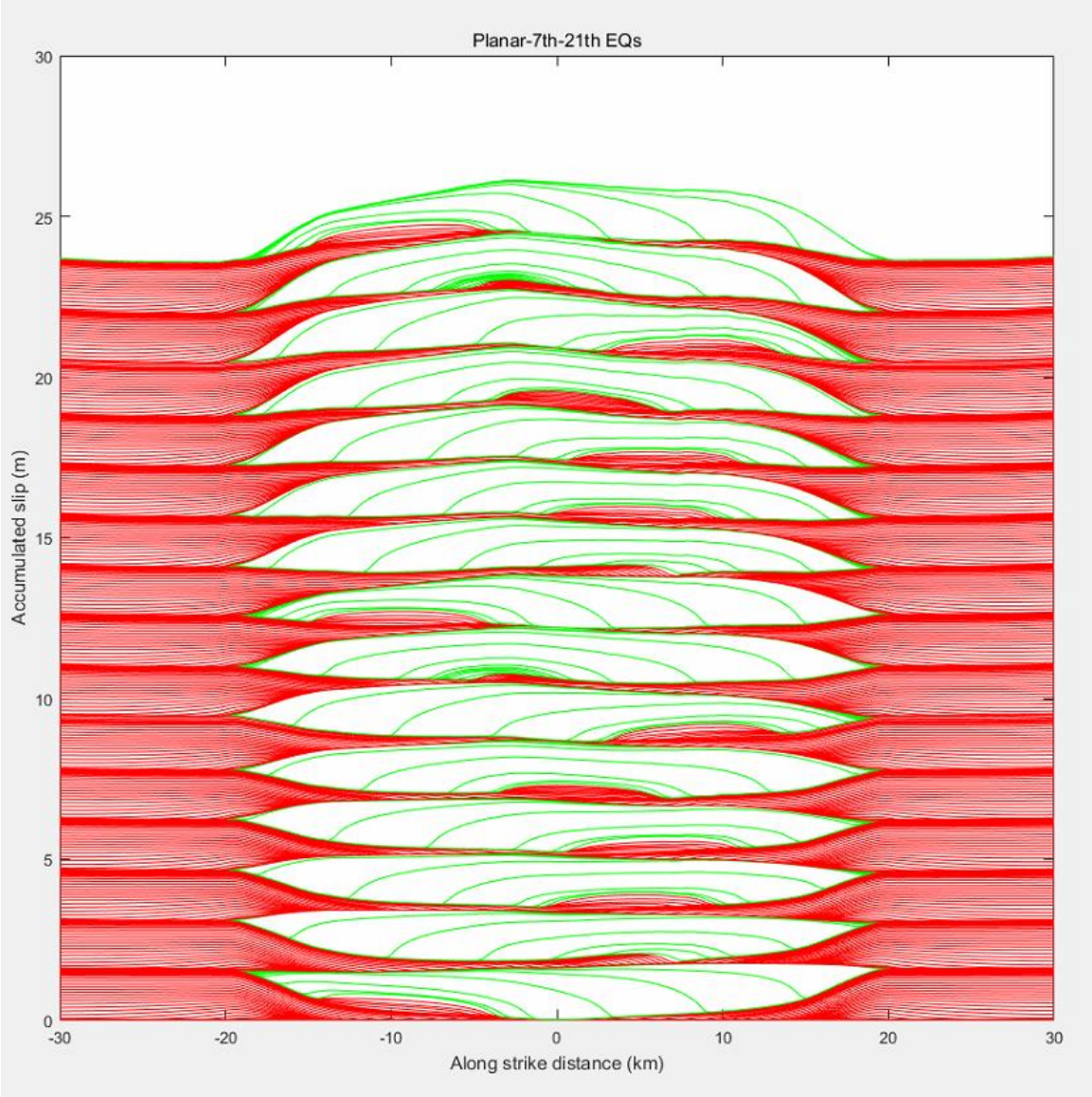

Figure 2.4 Accumulated slips at the z = -9 km horizontal profile of the planar fault model from the 7th to the 21st events. The green curves, representing dynamic ruptures, are separated every 10 s, which are 500 time-steps of dt = 0.02 s. The red curves, indicating quasi-static deformation, are separated every 100 time-steps. Because of the variable time stepping, the 100 time-steps may range from seconds to years.

2.4.2 Earthquake cycles on the fault with a bend

We simulate earthquake cycles on the strike-slip fault with the bend as presented in Figure 2.1b. The left segment and the right segment are termed as in Figure 2.1c. Trending from

the left segment to the right segment, the strike of the left segment is 0°, and it transits to 10° at the right segment. The transition takes place through the smooth bend as introduced in Section 2.2.4 and Figure 2.2. We keep the regional stress field uniform. With σ_1 at a 45° to the left segment, the normal and shear stresses on the left segment are -50MPa and 30 MPa, respectively. Because of the 10° change of strike, the normal and shear stresses on the right segment are -60.26 MPa and 28.19 MPa, respectively. The sense of slip is right lateral.

In the following subsections, we'll first present several features of the dynamics controlled by the smooth bend and the RSF. Second, we'll discuss how the reduction in the critical slip distance in the RSF affects the details of rupture dynamics.

2.4.2.1 Locations of earthquake nucleation

The privilege of implementing the RSF is to capture the nucleation phase of an earthquake cycle, when dramatic changes of shear stress, slip-rate, and state variable take place. In a previous earthquake cycle modeling, Duan and Oglesby (2005) combines a dynamic rupture model governed by the slip-weakening law (e.g., Day, 1982) for co-seismic deformation with an analytical solution of linear viscoelastic model to load the fault system between co-seismic events. They determine whether an earthquake nucleates if the Coulomb Failure Criteria in a patch of a certain size is met. In their 2D bent fault system, they find that most earthquakes nucleate around the bend and some of them terminate around the bend. Notably, in their 28th, 29th and 30th events, the nucleation occurs just left to the bend because of the low normal and yield stress induced by previous slips. With the implementation of the RSF, earthquakes still tend to terminate at the bend, but may not nucleate just next to the bend.

Figure 2.5 shows the last time steps in the nucleation phases, when dt_{evol} is reduced to ndt, of the first nine events in M11. For events with nucleation on the left segment, the locations

of nucleation patches stay a few kilometers left to the bend. For events with nucleation on the right segment, earthquakes may nucleate closer to the bend (5^{th} and 7^{th} event) comparing to those occur on the left segment. Occasionally, in the 5^{th} event, earthquake nucleates just right to the bend with a much smaller patch. The results are mainly caused by 1) the elevated stress heterogeneity induced by the bend and past slips and 2) nucleation patch size determined by the fricitonal parameters in the RSF and the normal stress heterogeneity, as esitmated by equation (8).

Figure 2.6a and 2.6b show the shear stress and the normal stress that is multiplied by 0.6 at the z = -9 km depth profile after the 4^{th} and 5^{th} dynamic events, respectively. The normal stress changes from -50 MPa on the left segment to the -60.26 MPa on the right segment. As indicated by the arrows, the normal stress dips left of the bend while is lifted right of the bend due to previous dynamic ruptures. According to equation (8), the estimations of nucleation patch size h^* for the left and the right segments are 10.15 km and 8.42 km, respectively, given the L = 11 mm in M11. The fault tends to nucleate in a larger patch if the normal stress decreases, while nucleates in a smaller patch with the normal stress lifted. In Figure 2.5, nucleation patches on the left segment are larger than those on the right segment. The patches on the left segment tend to stay a few kilometers left of the bend. The patches on the right segment are much closer to the bend. Especially in the 5^{th} event, the nucleation patch is very small and is just right to the bend. The elevated normal stress and shear stress right to the bend in Figure 2.6a makes the 5^{th} event breaking the right segment indicated by the reduced shear stress in Figure 2.6b. The 5^{th} event is about 13 days (0.0359 years) after the 4^{th} one, which is much shorter than the other intervals ranging from 8 years to about 70 years. The 8^{th} event breaking the left segment follows the 7^{th} rupture on the right segment in 6.2 days (0.017 years). However, the short interval is not caused

by stress heterogeneities at the bend but the stress level on the left segment ready for a rupture after 42.7 years loading after the 6th event on the left segment. The nucleation patch of the 8th event is close to the velocity strengthening zone on the left.

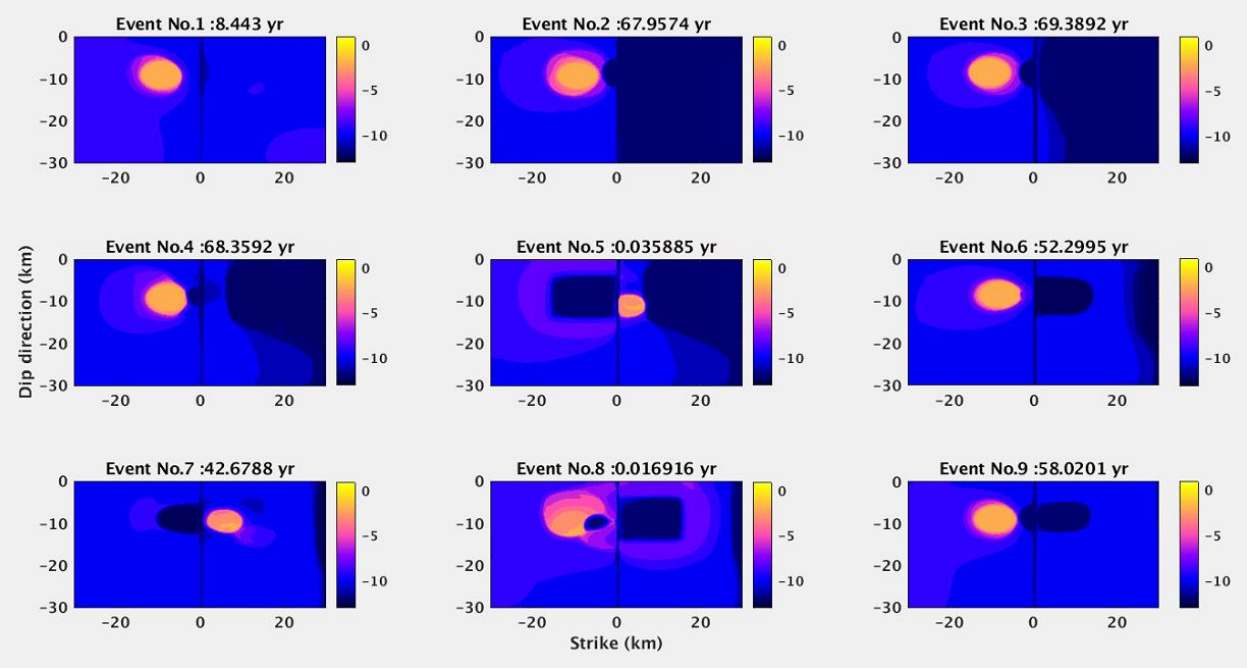

Figure 2.5 Logarithmic of sliprates at the last time steps of nucleation phases for the first nine events in M11. The event number and the years used from the current nucleation to the last one are labeled on each panel. Nucleation patches on the left segment are larger than those on the right segment because of the higher normal stress on the right segment contributed from both regionally resolved stress and previous dynamic ruptures. The patches on the left segment generally stay a few kilometers left to the normal stress dip of the bend caused by previous slips. The 5th and 7th events nucleate right to the bend. The fault area around the bend generally slip at the minimum slip rates.

(a)

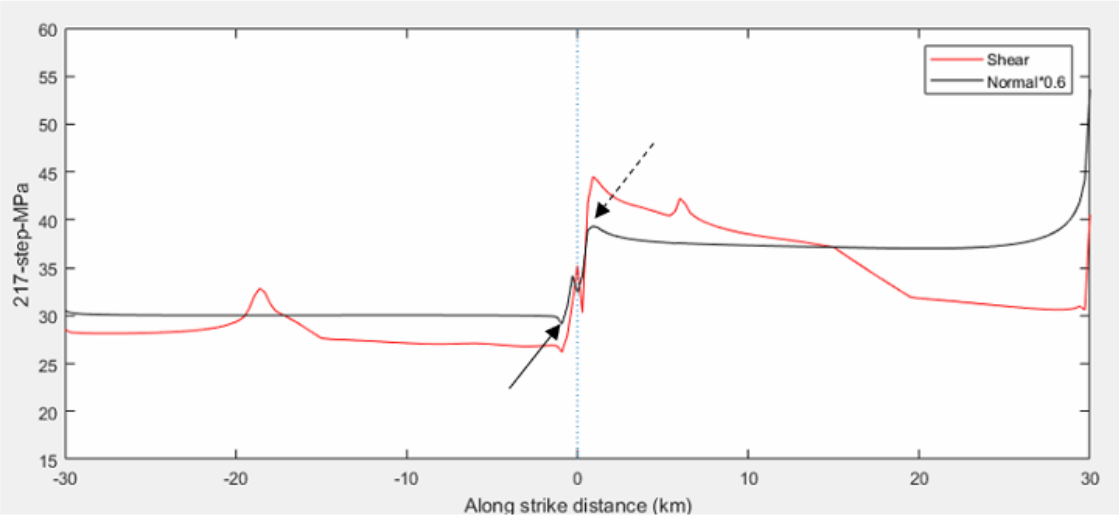

(b)

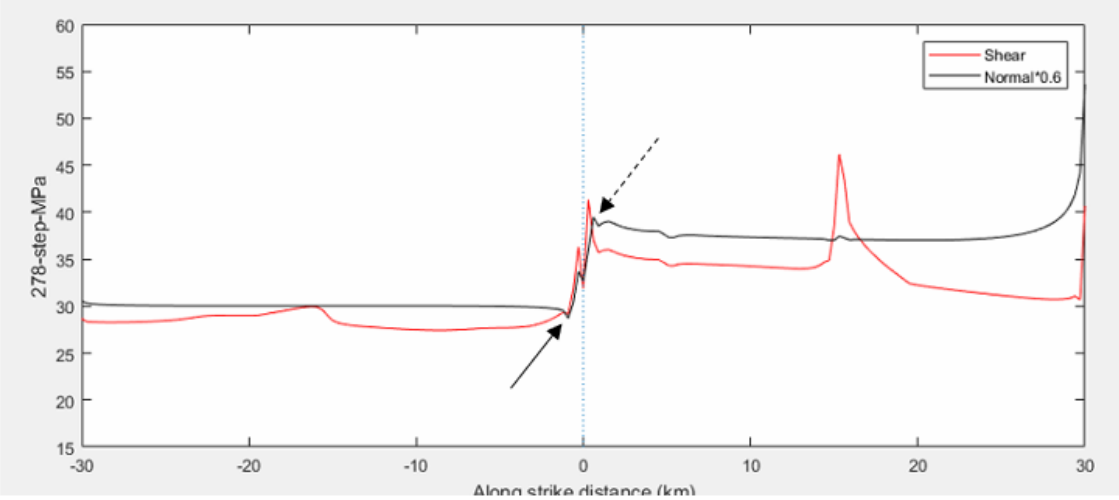

Figure 2.6 (a) and (b) show shear stress and scaled normal stresses at the 9 km depth profile after the 4th and 5th events in M11, respectively. The 4th event ruptures the left segment while the 5th ruptures the right segment. The normal stress is scaled by a factor of 0.6, which is the reference friction coefficient, to be at similar level as the shear stress. The dashed line labels the center of the fault at x = 0 km. Solid and dashed arrows show normal stress dips and elevated normal stresses because of previous dynamic ruptures, respectively.

2.4.2.2 The bend as a barrier to dynamic ruptures and the effect of the reference friction

Figure 2.7 shows accumulated slip histories along the horizontal profile at the z= -9 km depth for the first 10 events. There are two prominent features. First, the bend serves as a barrier to dynamic ruptures showing very limited amount of accumulated slips. Second, the left segment hosts seven out of ten events and the right segment accumulates far less slips compared to the left segment. They result from both stress heterogeneity around the bend and the relation between reference friction and the ratio of the shear stress to the normal stress.

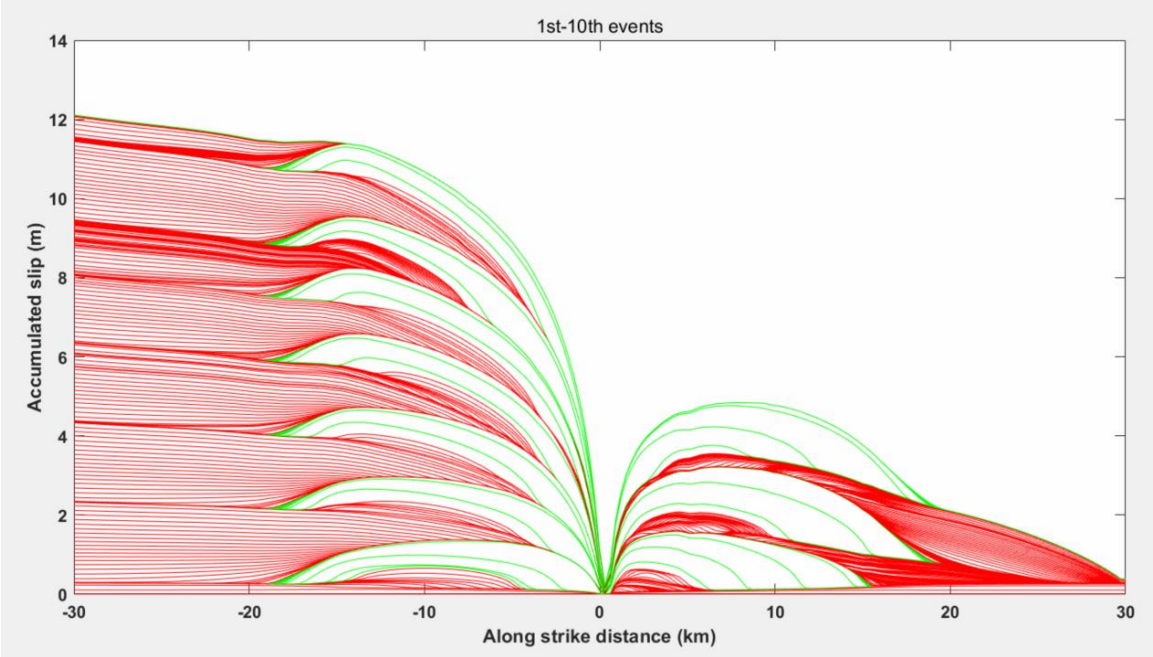

Figure 2.7 Accumulated slips at the z = -9 km horizontal profile on the fault with a bend from the 1st to the 10th event in M11. The green curves, representing dynamic ruptures, are separated every 10 s, which are 500 time-steps of dt = 0.02 s. The red curves, indicating quasi-static deformation, are separated every 100 time-steps. Because of the variable time stepping, the 100 time-steps may range from seconds to years. Two results are shown that the smooth bend is a barrier to slips and the right segment accumulated much less slips than the left segment over earthquake cycles.

The right segment accumulates much less slip compared to the left segment. It is caused by the ratio of initial shear stress to normal stress (0.468, computed using 28.19 MPa divided by 60.26 MPa) falling well below the reference friction (0.6), which leads the velocity strengthening region on the right segment slips at a lower sliprate of 10^{-12} m/s rather than 10^{-9} m/s as the velocity strengthening region on the left segment does. What if we modify the reference friction to match the initial ratio of shear stress to normal stress resolved from regional stress field? Will the bend still serve as a barrier to dynamic ruptures in this case? Figure 2.8 shows the accumulated slips along the z = -9 km horizontal profile in the first ten events in the model M11v (M11v has the same parameters as the M11 does except that the reference friction coefficient is computed by dividing the initial shear stress by the normal stress rather than a constant 0.6; it is also denoted in the foot note in Table 2.2) with varying reference friction that is calculated as initial shear stress divided by initial normal stress. Both ends of velocity strengthening regions slip at 10^{-9} m/s and accumulate equivalent amount of slips over earthquake cycles. The right segment hosts more events because of more loading from the velocity strengthening region. However, the bend still stops dynamic ruptures and accumulated very limited slips over earthquake cycles.

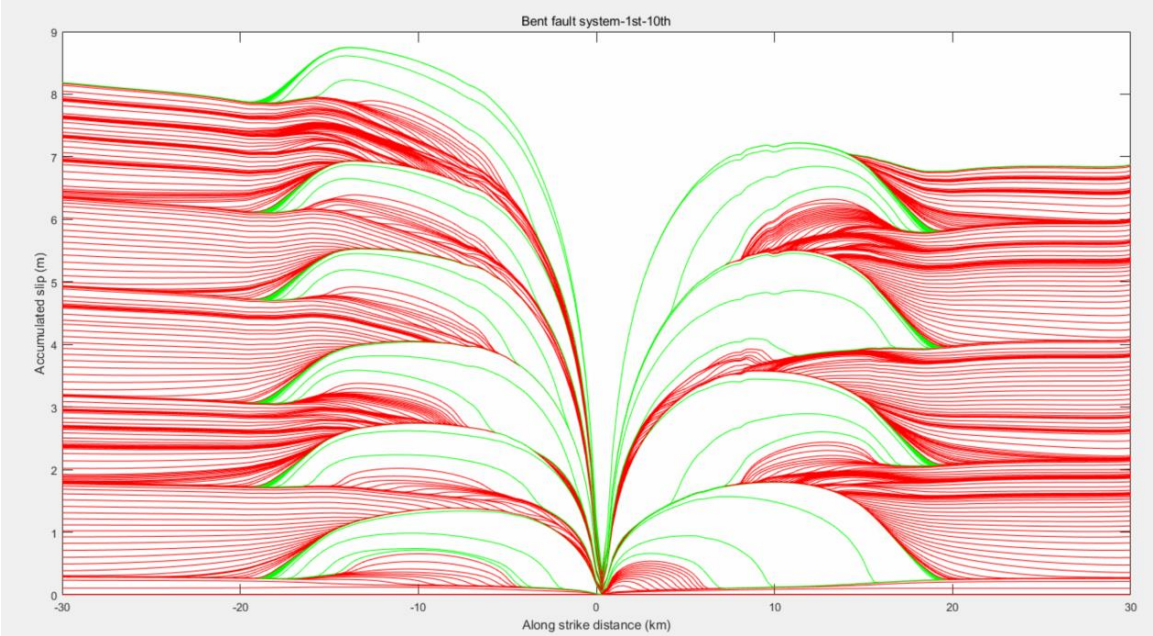

Figure 2.8 Accumulated slips at the 9 km horizontal profile on the bent fault from 1st to 10th event in M11v. The green curves, representing dynamic ruptures, are separated every 10 s, which are 500 time-steps of dt = 0.02 s. The red curves, indicating quasi-static deformation, are separated every 100 time-steps. Because of the variable time stepping, the 100 time-steps may range from seconds to years. First, the smooth kink severs as a strong barrier to slips; second, the right segment accumulates more slips and hosts more events than M11 does.

2.4.2.3 Earthquake event patterns

Figure 2.9 presents slip-rate, shear stress, accumulated slip, and normal stress histories at two on-fault stations from M11. One station is on the left segment at x = -6km and z = -9km and the other one is on the right segment at x = 6 km and z = -9 km, as shown by the red stars in Figure 2.1c. There is a total of 26 events simulated over the 810 years. The event number is labeled next of slip-rate history on the top panel. The solid lines represent results on the left segment and the dashed lines show those on the right segment.

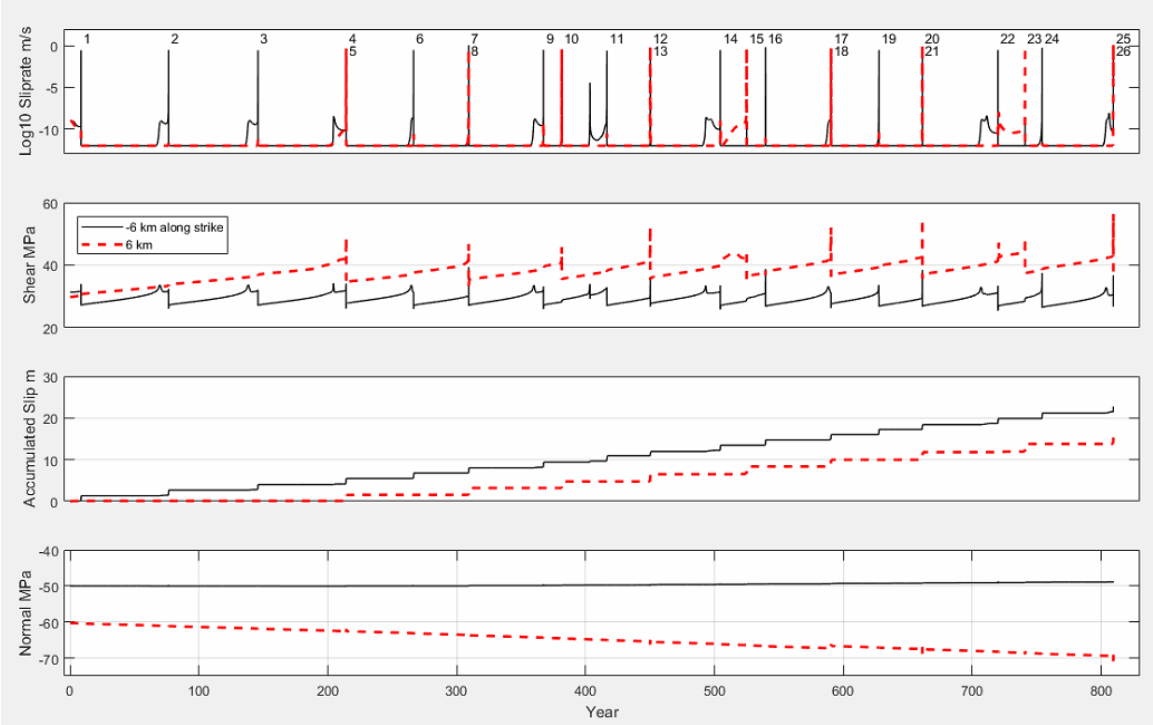

Figure 2.9 Slip-rate, shear stress, accumulated slip, and normal stress histories at two on-fault stations in M11 over 810 years simulated. A station lies on the left segment (solid lines) and the other station is located at the right segment (dashed lines). The two stations are both at z=-9 km depth.

There are four event patterns that are notable in the sequence. The first two patterns involve interactions of earthquakes from both fault segments. The third and fourth patterns are associated with each individual segment exclusively.

In the first pattern, some ruptures break the left and right segments consecutively with two events separated by several days up to tens of days and occasionally by several minutes. The lengths of 25 intervals between dynamic ruptures in the sequence are provided in Table 2.3. The intervals are calculated from the starting time point of previous dynamic event to that of the next event. The intervals are measured in years. Events 4 and 5, 7 and 8, 12 and 13, 17 and 18, 20 and

21 are separated by about 6 days (0.017 years) up to about 34 days (0.089 years). Events 25 and 26 are separated by about 190 seconds (6×10^{-6} years).

The second pattern involves three events, such as events 9-10-11, 14-15-16, and 22-23-24. It starts with a dynamic rupture on the left segment. Then, an earthquake tends to nucleate on the right segment but fails, indicated by a moderate rise of sliprate as shown after the 9th, 14th, and 22nd event. After about 10 – 20 years, a dynamic rupture occurs on the right segment. Events 14-15-16 and 22-23-24 follow the pattern exactly, while Events 9-10-11 has an extra failed nucleation on the left segment preceding the 11th event.

The previous two patterns involve interactions between the left and the right segments. The third and fourth patterns are associated with earthquakes exclusively on each individual segment. Table 2.4 and Table 2.5 list intervals between earthquakes on the left segment and intervals between events on the right segment, respectively. In the first 4 events, earthquakes only occur on the left segment. Earthquakes repeat about every 68 years. From the 4th event, the two segments actively interact with each other and collectively show patterns discussed above.

The third pattern is only associated with earthquakes on the left segment. As calculated in Table 2.4, from the 1st to the 4th event, earthquakes return about every 68 years. After the interaction between the two segments starts, from the 4th to the 12th, earthquakes on the left segment return from about 42 to 58 years. Finally, from the 12th to the 26th event, earthquakes on the left segment return about 30-some years or 50-some years after the previous one.

The fourth pattern only involves earthquakes on the right segment. As the numbers in Table 2.5 indicates, from the 8th event, the right segment will host an earthquake about every 71.5 years (the average of intervals from the 8th event with a deviation of 4.7 years).

Figure 2.5 show that the nucleation patch of the 5th rupture is rather small comparing to other rupture nucleation because of the elevated normal stress. The 5th event benefits from the first four dynamic ruptures on the left segment that well increase the stresses right of the bend. As shown in Figure 2.6a, the lifted shear stress heterogeneity occurs narrowly right to the bend, while the smaller nucleation patch favored by the elevated normal stress allows the rupture to nucleate.

Table 2.3 Lengths of intervals between earthquakes measured in years for all the 25 intervals. The interval is computed from the starting time point of previous dynamic rupture to the starting time of the next one.

Interval No.	1	2	3	4	5	6	7	8	9
Length of the interval in years	67.96	68.39	68.36	0.036	52.30	42.68	0.017	58.02	14.23
Interval No.	10	11	12	13	14	15	16	17	18
Length of the interval in years	34.99	33.62	0.089	54.28	20.47	14.61	50.81	0.06	37.18
Interval No.	19	20	21	22	23	24	25		
Length of the interval in years	33.63	0.038	58.67	21.06	13.21	55.27	6.0e-6		

Table 2.4 Lengths of intervals measured in years between events on the planar segment.

Event No.	1-2	2-3	3-4	4-6	6-7	7-9	9-12	12-14
Length of the interval in years	67.96	68.39	68.36	52.36	42.68	58.04	49.22	54.37
Event No.	14-16	16-17	17-19	19-20	20-22	22-24	24-26	
Length of the interval in years	35.08	50.81	37.24	33.63	58.71	34.27	55.27	

Table 2.5 Lengths of intervals measured in years between events on the bent segment.

Event No.	5-8	8-10	10-13	13-15	15-18	18-21	21-23	23-26
Length of the interval in years	95.02	72.25	68.70	74.75	65.48	70.85	79.73	68.48

2.4.2.4 The effect of the critical slip distance in the RSF

We decrease the critical slip distance L to 7 mm in M07. A shorter L reduces fracture energy and the size of nucleation patch. Reduced fracture energy leads to faster rupture speed and stronger stress heterogeneity around the bend. Figure 2.10 shows slip-rate, shear stress, accumulated slip, and normal stress histories at two on-fault stations in M07 over the 210 years simulated. Combining the smaller size of the patch to nucleate an earthquake and stronger stress heterogeneity around the bend, the first rupture on the right segment in M07 occurs about 3.8 days (0.0104 years) after the first event on the left segment as shown in Figure 2.10. In M11, the first event of the right segment comes after four ruptures on the left segment and after 210 years of slip evolution. In M07, we still can see failed nucleation after the 5^{th} event or after the 7^{th} event. But over the 210 years simulated in M07, the system hosts 9 events, much more than the 5 events in the first 210 years in M11. The left segment and the right segment evenly host 4 and 5 events, respectively.

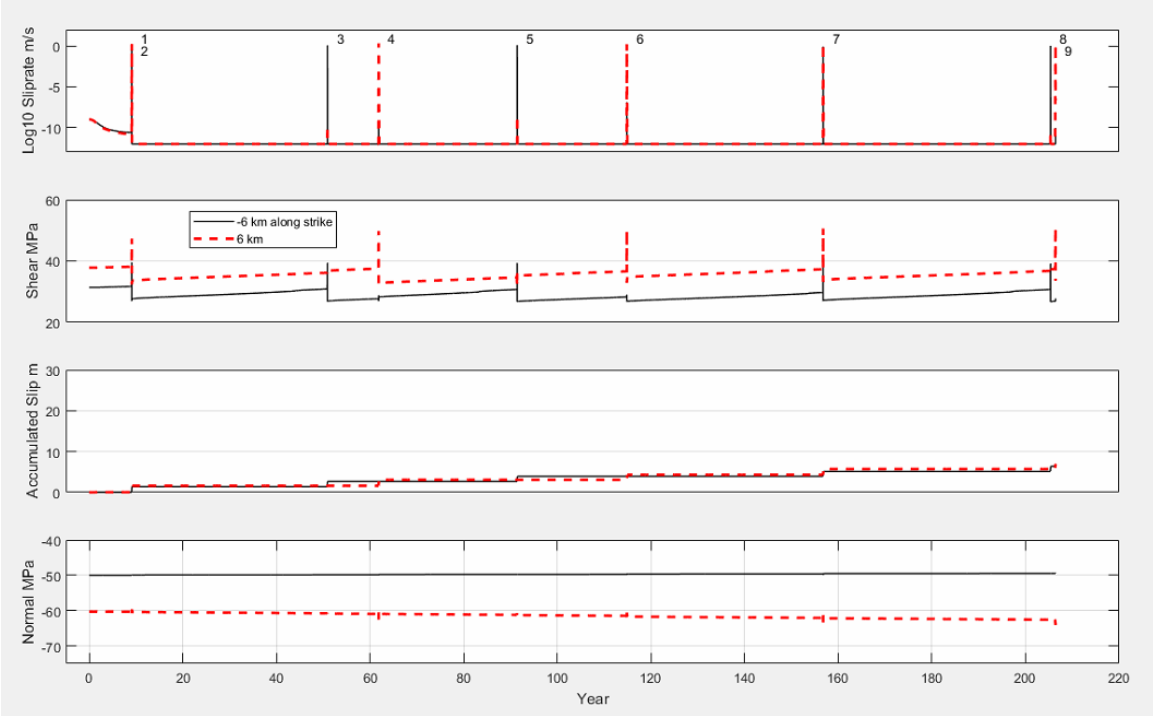

Figure 2.10 Slip-rate, shear stress, accumulated slip, and normal stress histories at two on-fault stations in M07 over the 210 years simulated. The two stations are at z = - 9 km depth and are shown by the red starts in Figure 2.1c. One station lies on the left segment (solid lines) and the other station is located on the right segment (dashed lines).

2.5 Discussion

2.5.1 The relation between stresses and the reference friction coefficient

Our results indicate that the initial stresses resolved from a uniform regional stress field based on local strike of the fault segment, the stress heterogeneity around the bend induced by dynamic ruptures, and the reference friction coefficient in the RSF influence the multicycle dynamics of the fault with a bend. In both dynamic rupture simulations and earthquake cycle simulations using the RSF, the reference friction coefficient is generally assumed to be a constant. If the reference friction coefficient is constant over both the left and the right segment as simulated in M11, the velocity strengthening region on the left segment will slip at $10^{-9}\ m/s$, three orders of magnitude larger than the $10^{-12}\ m/s$ of the velocity strengthening region on the

right segment. It results in much less accumulated slips on the right segment and few earthquake events. In dynamic events, the bend serves as a barrier to slips and accumulates very limited slips over the 810 years simulated. The cause is a low shear stress trap at the bend developed during the quasi-static deformations. Therefore, the fault will slip at the minimum required slip-rate 10^{-12} m/s.

In M11v, reference friction coefficient is calculated as the initial shear stress divided by the initial normal stress. It allows the velocity strengthening region on the right segment to accumulate equivalent slips and to host more earthquakes comparing to M11. However, as shown in Figure 2.8, the bend still tends to stop dynamic ruptures.

We may expect the reference friction coefficient to be a constant over the whole fault if the rock does not change properties significantly on the two fault segments. The results spark an idea to use long-term slip rates of various fault segments to estimate the ratio of shear stress to normal stress if the reference friction coefficient of the rock can be readily measured in the laboratory.

2.5.2 The bend as a barrier to slip and consecutive earthquakes

There are two predominant features associated with the bend. One feature is that it serves as a barrier to dynamic ruptures. The other one is that the bend accumulates very limited slips over the long term. The stress evolution in the velocity weakening zone is driven by the creeping (slips happening at very low sliprate such as 1e-12 ~ 1e-9 m/s) of velocity strengthening zone over the long-term between dynamic ruptures. A low shear stress trap at the bend develops during the quasi-static deformation phases between dynamic ruptures. It is the low shear stress trap that lowers shear stresses at the bend in the velocity weakening zone. The low shear stress trap impedes dynamic ruptures to get over the fault bend. The sliprates of the velocity

strengthening zone in the model evolves according to the stress evolution and the RSF, which differs from the fixed sliprate in Lapusta *et al.* (2000) and Lapusta and Liu (2009). We will examine which scheme has a better representation in the real faults in future works.

With the current setup of the models, we see new event patterns such as that earthquake occurs consecutively on the left and the right segments separated by days or tens of days or even minutes. When the stress heterogeneity builds up over many earthquake events, consecutive earthquakes on the two segments can be separated by 3 minutes, as shown by the 25^{th} and 26^{th} events in M11. The results imply that fault geometrical complexity could be the explanation for earthquakes on a fault but separated by minutes or days.

In terms of the limited amount of slip accumulated at the bend, Andrews (1989) argues that nonzero slip at the bend will cause unphysical stress singularity assuming no opening displacements on the fault. The remedy is that the fault bend belongs to a triple junction and the slips on the three segments have a vector sum of zero. In our study, the fault bend without a third spur segment governed by the RSF inherently show very limited slips. However, it is still necessary to carefully explore the parameter space including stresses and frictional parameters to validate the argument. Because the emphasize of the article is methodology and the Finite Element simulator, we'll systematically explore other factors that affect multicycle dynamics of geometrically complex fault systems in a future study. The factors may involve the bend angle, nucleation patch size, the angle between the principle stresses and the left segment, pore pressure change, etc. It is worth to point out the stresses around the bend build up over earthquake cycles. Therefore, the elastic model may not sustain itself without incurring inelastic deformation when stresses are very high over many earthquake cycles.

2.6 Conclusion

We propose a Finite Element simulator to model dynamics of earthquake cycles on 3D geometrically complex fault controlled by the RSF. The simulator includes an explicit EQdyna for co-seismic dynamic ruptures and EQquasi to model aseismic deformations of nucleation, post-seismic and inter-seismic deformations quasi-statically. In EQquasi, the variable time stepping scheme determined by the maximum sliprate on the fault allows simulation of long-term earthquake cycles over hundreds of years. We switch from EQquasi to EQdyna when the inertia forces of the fault mass cannot be neglected. The simulator is parallelized through MPI to boost computational efficiency.

We qualitatively validate the simulator by modeling earthquake cycles on a similar planar vertical strike-slip fault as that in Lapusta and Liu (2009). The on-fault station in the velocity weakening region accumulates slips in a staircase manner and the station in the velocity strengthening region creeps to increase slips.

Earthquake cycles on a strike-slip fault with a bend are simulated. The fault bends 10° through a smooth bend structure that changes strikes over one to two kilometers depending on the element size. The size of nucleation patch on the left segment is larger than that on the right segment due to the lower normal stress on the left segment resolved from the regional stress field. Dynamic ruptures reduce stresses left of the bend but lift those right of the bend. When the shear stress builds up high enough on the right segment, an earthquake may nucleate if the nucleation patch becomes small enough due to the elevated normal stress heterogeneity. The nucleation patches on the left segment stay a few kilometers away from the bend, while they may stay close to the bend due to their various sizes.

The bend is a barrier to dynamic ruptures and accumulates very limited slips over the long-term, because a low shear stress develops at the bend during quasi-static deformation phases. Therefore, the bend will slip at the minimum required slip-rate 10^{-12} m/s.

The relation between the ratio of the shear stress to the normal stress and the reference friction coefficient in the RSF affects the slip-rate of velocity strengthening regions of the left and the right segments. Given a constant reference friction, 0.6, on the whole fault, the velocity strengthening region of the right segment may creep at 10^{-12} m/s, compared to the 10^{-9} m/s creeping rate of the velocity strengthening region on the left segment. It is caused by the ratio of the shear stress to the normal stress falls well below 0.6 on the right segment. If the reference friction coefficient is adjusted based on the ratio of initial shear stress to the normal stress, the right segment will creep at a similar rate of 10^{-9} m/s. The results spark an idea to use long-term slip rates of various fault segments to estimate the ratio of shear stress to normal stress if the reference friction coefficient of the rock can be readily measured in the laboratory.

Complex earthquake event patterns are identified in the fault system. Earthquakes interact between the two segments. Sometimes, events breaking consecutively the left and the right segments can be separated by tens of days, a few days, or even several minutes. Earthquakes also show returning patterns for each individual segment exclusively, such as that earthquakes on the right segment returns about 71.5 years on average.

A reduced critical slip distance L in the RSF results in faster rupture speed and stronger stress heterogeneity around the bend, promoting a much earlier earthquake on the right segment.

CHAPTER III

GROUND MOTION SIMULATION OF SCENARIO EARTHQUAKE IN NORTH CHINA BASIN

3.1 Introduction

To predict when an earthquake hits a region is still not feasible in the near future. However, we can estimate the potential damage by simulating earthquake ruptures and the corresponding ground motion[1].

Yin et al. (2014) identify a 160km-long seismic gap along the Tianjin-Hejian-Cixian (THC) fault in the NCB, where a series of large earthquakes that caused severe damage stroke in the 1960s and 1970s, including the devastating 1976 M_w 7.6 Tangshan earthquake (Liu et al., 2002). Yin et al. (2014) conclude that the seismic gap can generate a M_w 7.5 earthquake. The seismic gap passes through Tianjin, an economically and politically important city in northern China with a population of 13 million. We denote this seismic gap as the Tianjin seismic gap in this work.

Ground motion simulations of scenario earthquakes (i.e., potential, disastrous earthquakes) on seismically active faults have become an important means for seismic hazard assessment and mitigation in the recent decade. For example, the Shakeout-K and -D simulations are multidisciplinary collaborations led by USGS (U.S. Geological Survey) and SCEC (Southern California Earthquake Center) to predict strong ground motion in southern California from potential earthquakes on the southern San Andreas Fault (Bielak et al., 2010, Olsen et al., 2008,

[1] The Chapter III on ground motion is modified from "Scenario Earthquake and Ground-Motion Simulations in North China: Effects of Heterogeneous Fault Stress and 3D Basin Structure" by Dunyu Liu and Benchun Duan, 2018, *Bulletin of Seismological Society of America*, 108(4): 2148-2169. https://doi.org/10.1785/0120170374.

Olsen et al., 2009). Fruitful results have been obtained. For example, these studies found that an energy channel through the San Bernardino-Chino-San Gabriel-Los Angeles basins may lead to strong localized amplification around Whittier Narrows and the Los Angeles basin. By comparing kinematic and dynamic sources, Olsen et al. (2008) concluded that spontaneous dynamic source generates more reasonable ground motion both at rock sites and in low velocity sedimentary basins, due to its less coherent wavefield induced by the complicated rupture propagation. Day et al. (2008b) found that the amplification inside sedimentary basins strongly relates to basin depths and frequency of the shaking, i.e., the amplification increases with basin depths and periods.

Previous studies have also shown that sedimentary basins significantly amplify and prolongate ground motion by basin-edge induced diffracted waves and surface waves (e.g., Kawase, 1996, Sato et al., 1999, Narayan, 2012, Pitarka et al., 1998). Kawase and Aki (1989) found that edges of 2D deep basin structure help trap seismic waves to generate large amplitude surface waves and to elongate the duration of seismic vibrations. A soft layer embedded on top of the deep basin would induce even longer duration up to 80 s in their study, which can explain the observation in the 1985 Michoacan Mexico Earthquake. Graves (1995) found similar long duration in the Los Angeles basin from the 1994 Northridge earthquake. In his simulation, he also successfully captured the recorded large amplitude and long duration waves using a deep sediment basin with several shallow closed-shape small basins. Besides trapping seismic waves, basin edges also induce basin-edge transduced waves (e.g., Narayan, 2012) and cause localized amplifications, termed as the basin-edge effect, which has been used by Kawase (1996) to explain the damage belt observed in the 1995 Kobe earthquake.

Low-velocity sedimentary basins with different sizes, depths, and shapes exist in NCB, and the Tianjin seismic gap passes through two of these sedimentary basins at its two ends (Figure 3.1). How may the two sedimentary basins affect rupture propagation and slip distribution if a M_w 7.5 earthquake happens on the seismic gap? How may these basins affect ground motions in this important region? What level of ground shaking can happen? To address these questions, we simulate spontaneous rupture propagation on the seismic gap and seismic wave propagation in high-resolution 3D velocity structures of the region.

One of important parameters in spontaneous rupture models is the initial stress on the fault. Studies on past large earthquakes (e.g., Mai and Beroza, 2002) suggest the fractal nature of earthquakes, which means that the stress drop or slip distribution on a fault exhibits a power-law spectrum in the wave number domain. Based on this feature of natural earthquakes, Andrews and Barall (2011) proposed a method to set up self-similar initial stresses for spontaneous rupture models. As they focused on ground motion simulations, they did not explore in details complex rupture processes. In this work, we will also examine how self-similar heterogeneous initial stresses affect dynamic rupture propagation.

3.2 Method: EQdyna with Perfectly Matched Layer Absorbing Boundary and Coarse-Grained Q Attenuation Model

We use an explicit, dynamic finite element method (FEM) code EQdyna (Duan and Day, 2008, Duan, 2010, Duan, 2012, Duan and Oglesby, 2006) to simulate dynamic rupture and seismic wave propagation in this study. 3D Versions of EQdyna, including the hybrid MPI/OpenMP parallel version (Duan, 2012), have been validated against recent benchmark problems of the SCEC/USGS Spontaneous Rupture Code Verification Project (Harris et al., 2009, Harris et al., 2011, Harris et al., 2018b). EQdyna features an under-integrated hexahedron

element stabilized by hourglass control (Kosloff and Frazier, 1978). With the explicit central difference time integration, the method has been proved to be efficient and accurate in simulating spontaneous rupture and seismic wave propagation. The traction-at-split-node (TSN) scheme of Day et al. (2005) is adopted to treat the faulting boundary in EQdyna (Duan, 2010). In this work, further efforts have been made on implementing into EQdyna the Perfectly Matched Layer (PML) absorbing boundary (e.g., Collino and Tsogka, 2001, Ma and Liu, 2006) to reduce model sizes for computational efficiency, and the coarse-grained Q model (e.g., Day, 1998, Ma and Liu, 2006) to model the anelastic attenuation of seismic waves.

3.2.1 Perfectly Matched Layer absorbing boundary

After Berenger (1994) 's introduction of PML absorbing boundary to electromagnetic wave propagation, the remarkable analytical zero-reflection property at the PML interface has drawn a great attention. The algorithm has been shown to be very effective and efficient even after numerical discretization. Collino and Tsogka (2001) extended the formula to elastic wave propagation. Their velocity-stress presentation becomes a basis for both 3D staggered-grid velocity-stress finite-difference methods (Festa and Nielsen, 2003) and explicit finite element methods (Ma and Liu, 2006). We adopt the formulation of Ma and Liu (2006) to implement PML into EQdyna. Two differences are the treatment of velocity continuity along the PML interior interface and the choice of hourglass control scheme. In Ma and Liu (2006), they use velocities calculated from the interior region for the nodes along the interface and ignore the contribution to velocities from the elements in the PML region. Theoretically, this treatment may result in non-zero-reflection at the PML interior boundary. In our work, we compute the contribution to velocities from the elements both in the interior region adjacent to PML and in the PML region. In addition, we find out that the hourglass control scheme proposed by Kosloff

and Frazier (1978), which has been used in EQdyna, works stably and accurately for under-integrated hexahedral PML elements in EQdyna (see Appendix A).

3.2.2 Coarse-grained Q modeling

An important property of Earth's material is its anelastic response to loading forces. It is easy to account for this effect in the frequency domain, while the convolution expression of stress-strain relation makes it ineffective to be implemented into time-marching numerical methods, such as finite difference and finite element methods (Day and Minster, 1984). Based on the Padé approximant, Day and Minster (1984) first transform the convolution expression of general anelastic laws into a differential form. Later, Day (1998) uses coarse-grained memory variables to formulate the attenuation term, which significantly reduces the memory cost. Ma and Liu (2006) incorporate the scheme into their finite element code with under-integrated hexahedral elements.

We largely follow Ma and Liu (2006)'s formulation to implement the coarse-grain Q modeling into EQdyna. We make several remarks on the implementation. The first note is that the Lamé constants in the equations should be the unrelaxed modulus. We adopt Graves and Day (2003)'s element specific modulus formulation to set up the unrelaxed modulus. The second one is that the relaxation coefficients used in Ma and Liu (2006)'s formula are derived from Liu and Archuleta (2006)'s scheme, which is proposed for 1D constitutive relationship. As noted by Day (1998), in 3D cases using the average of attenuations from 8 adjacent elements to represent the attenuation in the volume, a factor of 8 should be multiplied to the relaxation coefficients derived from 1D constitutive relation. The third note is that the PML schemes used in Collino and Tsogka (2001) and Ma and Liu (2006) are proposed for perfect elastic material without any attenuation. Directly combining the elastic PML with the coarse-grained Q model inside the

research region may cause some unexpected reflections from the PML/interior boundary. However, because the attenuation term is generally small in terms of the elastic stress change, in numerical experiments this effect might be negligible. Theoretically, we could follow Liu and Tao (1997)'s method to derive additional terms to account for the anelastic attenuation for the PML elements.

We validate our numerical implementation of the coarse-grained Q modeling in EQdyna by simulating the same benchmark problem of Ma and Liu (2006). We compare our results with the analytical synthetic seismograms computed using the computer program for seismology (CPS) (Herrmann, 2013). The description of the benchmark problem and the comparison of results are presented in Appendix A.

3.3 Models

3.3.1 Fault geometry and finite element models

Figure 3.1 shows the study area in NCB area. Surrounding mountains (Taihang Shan and Yan Shan), Bohai Bay, provincial boundaries (light dashed lines) and important cities such as Beijing and Tianjin are illustrated. The 160 km seismic gap is indicated by the solid thick line. It starts from the southwest end at 116.23º E, 38.57º N to the northeast end at 117.72º E, 39.38º N. The thick dashed line shows the extension of the seismic gap along the THC fault, and its northeast portion was responsible for the disastrous 1976 M_w 7.8 Tangshan earthquake (indicated by the star). The seismic gap passes through the city of Tianjin and lies between the historical 1144 Hejian earthquake and the 1977 Tanggu Earthquake (Earthquake No. 3 and No. 24 in Figure 1 of Yin et al. (2014), respectively). The fault is a vertical strike-slip fault with a width of 20 km, which is supported by earthquake locations (e.g., Liu et al., 2016).

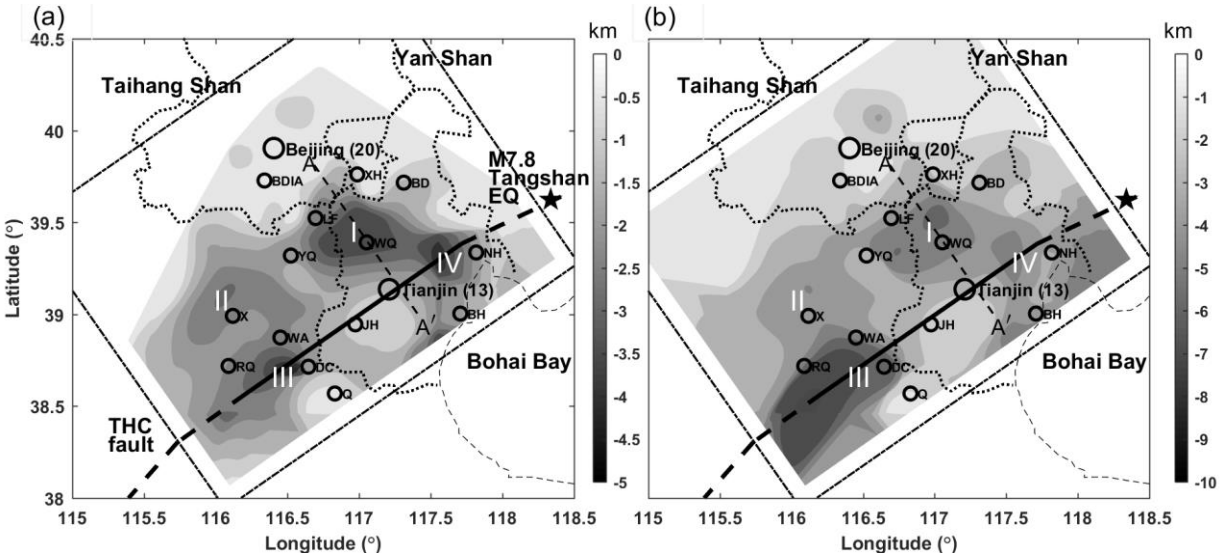

Figure 3.1 Research region, surrounded by Taihang Shan, Yan Shan and Bohai Bay, and isosurfaces of basin depth determined by shear wave velocity Vs=1.5 km/s (a) and Vs=2.5 km/s (b). The thick line denotes the THC fault, with the solid part for the 160 seismic gap modeled in this study. The devastating 1976 M_w 7.6 earthquake (star) occurred to northeast of the seismic gap on the THC fault. Light dashed lines outline the political boundaries of Beijing and Tianjin, with populations of 20 and 13 million, respectively. Notations: BDIA-Beijing Daxing Internatinal Airport, NH-Ninghe, BH-Binhai, JH-Jinghai, DC-Dacheng, Q-Qingxian, WA-Wen'an, RQ-Renqiu, X-Xiongxian, YQ-Yongqing, LF-Langfang, BD-Bindi, XH-Xianghe. Four basins exist in the study area. Basin I is around Wuqing and has a similar size and shape to the Los Angeles Basin. Basin II is around Xiongxian. Basin III is a tilted basin passed by the southwest end of the gap. Basin IV is at the northeast end of the gap. Dash-dotted rectangular shows the model boundaries. Fourier amplitude spectra of synthetic velocities along the profile AA' are shown in Figure 3.10.

The boundaries of the finite element (FE) models are shown by the dash-dotted rectangular. The boundaries of the FE models are 50 km away from the fault ends along the strike, 50 km away towards southeast normal to the fault trace and 50 km downwards from the bottom of the fault, respectively. The northwest boundary normal to the fault is 150 km away to include low velocity sedimentary basins and cities of interest. These FE model boundaries are far enough away from the fault so that slip on the fault will not be affected by these fixed boundaries. As the PML absorbing boundaries are implemented in this study, we do not need a

large buffer region in the FE models. With an element size of 200 m, each FE model consists of ~478 million hexahedral elements. The minimum shear wave velocity is truncated at 500 m/s. If the wavelength of a frequency component needs to be resolved by at least 5 elements, the maximum reliable frequency is 0.5 Hz. High frequency noises should be suppressed by the hourglass control and a small stiffness-proportional Rayleigh damping in EQdyna.

3.3.2 Seismic velocity structure and anelastic attenuation model

After a series of disastrous earthquakes in NCB in the 1960-70s, China Earthquake Administration had organized to conduct more than 30 deep seismic sounding (DSS) profiles in this area. Wei et al. (2007) select 14 profiles and construct a P-wave velocity model in the region from 110° E to 120° E in longitude and from 35° N to 41° N in latitude. Yang and Huang (2013) combine 40 survey points of seismic stack velocity data from petroleum industry with 9 DSS profiles to construct a high-resolution upper-crust P-wave velocity structure around Beijing (from 115.5° E to 117.6° E in longitude and from 38.4° N to 40.75° N in latitude). We collect the P-wave velocity data from 9 horizontal cross-sections every 1 km from the free surface to 8 km depth in Yang and Huang (2013) and from 2 cross-sections at the free surface and 10 km depth in Wei et al. (2007). We interpolate the P wave velocity onto the nodes in our finite element model. In the upper 10 km, the maximum and minimum P wave velocities are 6.42 km/s and 1.7 km/s, respectively. Below 10 km and outside the region of P-wave velocity models of Wei et al. (2007) and Yang and Huang (2013), a constant 6.42 km/s is applied. Because in this study, we focus on basin effect and near source ground motion, Moho is not considered in the models. Figure 3.2 shows the P wave velocity on the free surface and 3 km depth extracted from Yang and Huang (2013), which are identical to the original Figure 4 of Yang and Huang (2013).

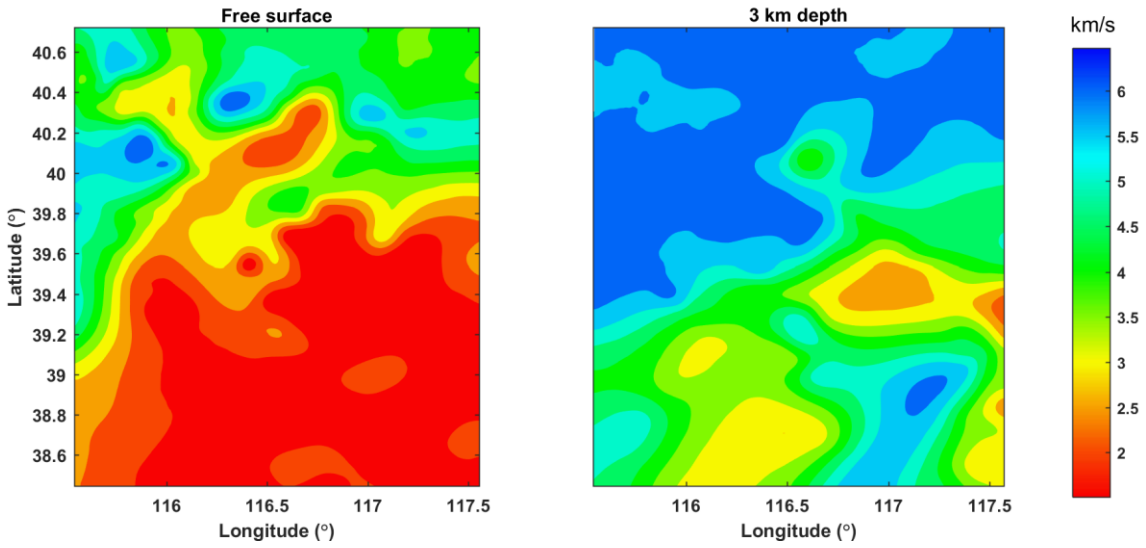

Figure 3.2 Reconstructed high-resolution P wave velocity structures (Yang and Huang, 2013) on horizontal cross-sections at the free surface (left) and 3 km depth (right) used in the velocity structure model for the simulations. The region extends from 115.5° E to 117.6° E in longitude and from 38.4° N to 40.75° N in latitude. It covers the major portion of velocity structure in our finite element model except in the Northeast. The velocity structure in the east corner of the finite element models is constructed with Wei *et al.* (2007)'s P-wave velocity structure of a lower resolution.

The shear wave velocity and density are derived from empirical relationships proposed by Brocher (2005), which is valid for Vp from 1.5 km/s to 7 km/s. Figure 3.3 shows the empirical relations between shear wave velocity and density against P wave velocity from Brocher (2005). The minimum shear wave velocity in our models could be as low as 330 m/s, which poses a big challenge to computational resources. Therefore, shear wave velocities are truncated at 500 m/s, similar to a previous study by Olsen et al. (2003). They point out that by doing so, it would underestimate 10 to 20% of the amplitude in the frequency 0-0.5 Hz in the SCEC model, which is acceptable in our study.

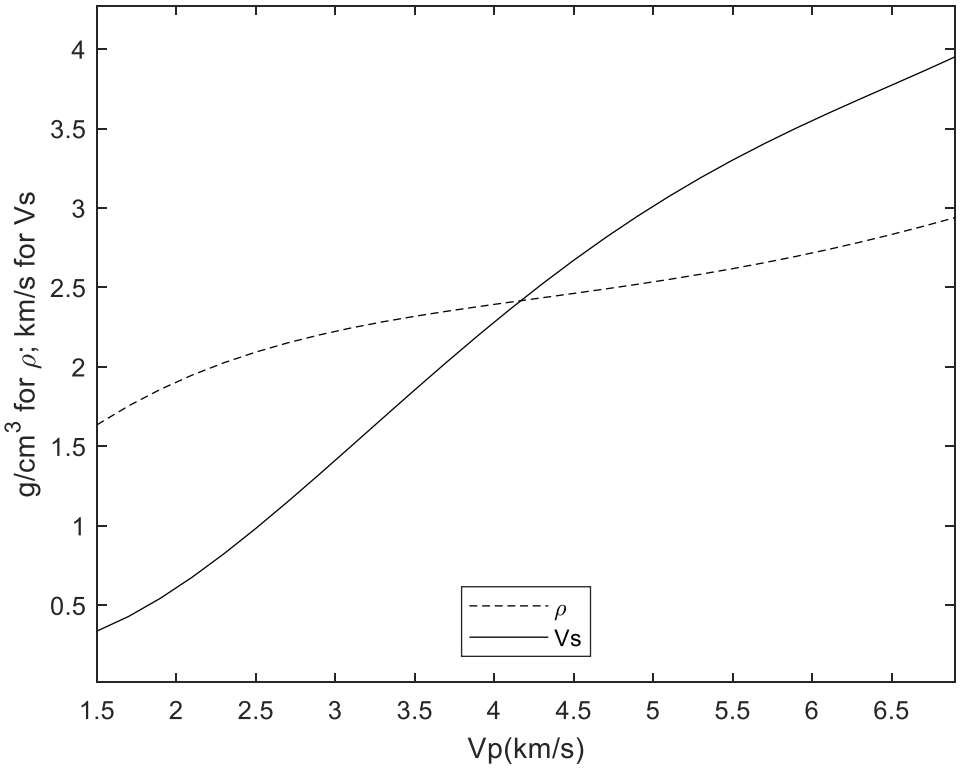

Figure 3.3 Density (dashed line) and shear wave velocity (solid line) as a function of P wave velocity from the regression relations in Brocher (2005).

Day et al. (2008b) propose Vs=1.5 km/s as the best predictor for basin structure, while the difference between using Vs=1.0, 1.5 or 2.5 km/s as the indicator are not very significant, due to the strong correlation of 3D basin structures defined by these Vs'. Hence, in Figure 3.1 we present basin structures by isosurfaces of basin depth determined by Vs=1.5 km/s and Vs=2.5 km/s, respectively. Low velocity sediments (Vs<1.5 km/s) exist in NCB. Four bowl-shape basins are identified and numbered by roman numerals. A basin with about 40 km horizontal dimensions (hereafter Basin I) is located around Wuqing (WQ), between Beijing and Tianjin. It is of a similar shape and size to the Los Angeles basin in southern California. Around Xiong Xian (X), a small basin (Basin II) can be identified in Figure 3.1 (a), while the edges of the basin

become blurry in Figure 3.1 (b). At the southwest end of the seismic gap, a very deep and tilted basin (Basin III) exists, with the deepest depth reaching 8 km in Figure 3.1 (b). At the northeast end of the fault, a fourth basin (Basin IV) can be identified. It is worth to point out that this basin is located at the junction of two velocity structure datasets, thus the northeast portion of the basin is not well resolved.

The attenuation model is another key factor to simulate realistic ground motion, especially for locations where basin effects are expected (Olsen et al., 2003, Day et al., 2008b). Attenuation models describe the spatial distributions of quality factor Qp and Qs. Olsen (2003) has compared several attenuation models for the Los Angeles basin by validating simulated seismograms against recordings from the well-recorded 1994 Northridge earthquake. In the upper crust of North China basins, the distribution of quality factor Qp and Qs is still poorly understood. In this study, we adopt the best attenuation model of Olsen et al. (2003) as below,

$$\mathrm{Q_s} = 0.02 v_s \quad if\ v_s \leq 1500\ \mathrm{m/s}\ ,$$

$$\mathrm{Q_s} = 0.1 v_s \quad if\ v_s > 1500\ \mathrm{m/s}\ ,$$

$$\mathrm{Q_p} = 1.5\mathrm{Q_s}\ .$$

3.3.3 Self-similarly heterogeneous stresses setup and reference models

In spontaneously dynamic rupture models, initial stresses are important but are not well constrained by observations. Efforts have been made by using heterogeneous stress drop (Oglesby and Day, 2002) or slip (Lavallee et al., 2006) in physical-based spontaneous rupture models to explore effects of stress heterogeneity on rupture process and corresponding ground motion. The fractal nature of earthquakes, exhibited as a power-law spectra distribution of slip or stress drop on fault, has been recognized by the seismological community (e.g., Andrews, 1980, Mai and Beroza, 2002, Andrews and Barall, 2011, Andrews, 1981). Andrews and Barall (2011)

propose a method to build heterogeneous initial stresses for spontaneously dynamic rupture models in a self-similar manner. In their method, the ratio of initial shear stress to depth-dependent normal stress, *w*, is set to be self-similar. They map a 2D self-similar random function *w* in the Fourier domain and invert it back to the space domain to generate initial stress distributions. Rupture length is controlled by half length of the longest wavelength component in the along-strike dimension of *w*. To limit the rupture within seismogenic depths, a conditioning function along dip direction is applied to taper shear stress below a certain depth. In this study, we use the FORTRAN code provided by Andrews and Barall (2011) to generate initial stresses for our heterogeneous ruptures. Formula and parameter selections are described below.

The depth-dependent effective vertical principle stress σ_z is,

$$\sigma_z = \int (\rho - \rho_w) g dz$$

Where ρ and ρ_w are the densities of rock and fluid, respectively, and g is the gravity acceleration. The on-fault normal stress, then, follows

$$\sigma_n = F\sigma_z$$

where F is related to tectonic setting and dipping angle of the fault. For the vertical strike-slip fault here, we assume $F = 1$, which yields

$$\sigma_n = \int (\rho - \rho_w) g dz$$

Given the self-similar random function $w = w(\mathrm{x}, \mathrm{y})$ that fluctuates around 1 and depth conditioning function $D(z)$, initial shear stress τ has a relationship with the normal stress σ_n as

$$\frac{\tau}{\sigma_n} = (\mu_d + \alpha w) D(z)$$

where μ_d is dynamic friction coefficient and α is an adjustable parameter to control the stress drop (or equivalently earthquake magnitude). $D(z)$ has the form of $D(z) = 1/(1 + ({}^{z}/_{z_0})^4)$,

where z_0 is a constant. Static friction is chosen as a typical value for the upper crust rock of $\mu_s = 0.7$. However, in some places the initial shear stress may be larger than the shear strength because of the heterogeneous fluctuation of *w*. To maintain the stability of the fault system before a rupture starts, static friction should take the maximum of μ_s and $(1+\epsilon)\frac{\tau}{\sigma_n}$. ϵ is a small fraction and its default value is 0.01. As a result, static frictions range between 0.7 and 0.79 in our simulations.

The rupture length is roughly controlled by the half wavelength of the longest mode of the along-strike dimension of *w*. This half wavelength is represented by an unitless 1024 points in Andrews and Barall (2011)'s code. To simulate a 160 km rupture, we choose a spatial grid interval of 160 m. Using the same high-cut filter at a factor of 8 below Nyquist as that used in Andrews and Barall (2011), it is safe to interpolate the initial physical quantities onto a finite element size up to 8 times of 160 m. It means the 200 m element size in our finite element models is acceptable. Typical focal depths of earthquakes in the NCB region range from 9 to 15 km (Liu et al., 2016, and references therein). Given $z_0 = 30\ km, \mu_d = 0.6\ and\ \alpha = 0.05$, initial shear stress is equal to sliding frictional stress at the depth of 16.1 km, above which major ruptures may occur. In addition, these chosen parameters can generate earthquakes of magnitudes around M_w 7.5 as proposed by Yin et al. (2014). The scenarios are determined by the random function *w*, which is generated with a set of random seeds (Andrews and Barall, 2011). We generate four sets of self-similar heterogeneous stresses with four sets of random seeds (Table 3.1). With other variations, we have a total of 8 models (Table 3.1). In the model names, H stands for heterogeneous stress setup and R represents the reference models (further discussion below). In the heterogeneous models, the first index indicates different stress randomizations, and the second index indicates different D_0 values used in the simulations, where 1 stands for

D_0=0.4 m and 2 stands for D_0=1.0 m. In the slip-weakening law (e.g., Ida, 1972; Day, 1982), D_0 is the critical slip distance over which shear stress drops from shear strength to frictional sliding shear stress. B in H21B indicates a buried rupture.

Table 3.1 Parameters of eight models simulated in this study, including six self-similar scenarios and two reference scenarios.

Model Name	D_0 (m)	Seed 1	Seed 2	Seed 3	Seed 4
H11	0.4	1325	5321	3852	9093
H21	0.4	1234	2345	3456	4567
H31	0.4	9053	2873	5830	8767
H41	0.4	3728	3392	3859	2534
H21B	0.4	Same as H21			
H22	1.0	Same as H21			
R1	0.4	From NE to SW.			
R2	0.4	From SW to NE.			

*Four sets of random seeds are used to generate random function w(x,y) for four heterogeneous models H11, H21, H31, and H41. The other two heterogeneous models are two variations from H21, with H21B as a buried rupture and H22 using a larger critical slip-weakening distance D_0. The two reference models have a constant w(x,y)=1 with the hypocenter location at the northeast and southwest ends of the fault in R1 and R2, respectively.

It is worth to point out that as required by Andrews and Barall (2011)'s method, to simulate a 160 km dynamic rupture with self-similar heterogeneous stresses, the fault should be set as 320 km in length, twice of the targeting 160 km, and the actual rupture length can only be known after simulation. We first make trial simulations on models with an element size of 500 m and find that, in practice, the ruptures are effectively restricted within the 160 km by stress conditions. Therefore, we set the fault length as 180 km, in case that a rupture longer than 160 km may exist, but do not set the fault 320 km long to reduce computational costs.

Besides the heterogeneous stress models, two reference models are built with the ratio of initial shear stress to normal stress being a constant. The only difference in the two reference models is the hypocenter location, which is at the northeast end and the southwest end of the fault in R1 and R2, respectively (Table 3.1 and Figure 3.4). To make the heterogeneous and reference models comparable, we simply let $w = 1$ in the reference models. At the same time, a conditioning function along strike direction *D*(x) is used to spontaneously cease the rupture when it approaches the lateral fault edges in the two reference models. In the coordinate system of our finite element mesh, the fault strike ranges from -90 km to 90 km along x direction, thus

$$D(x) = \frac{1}{1 + \left({(abs(x) - 60)}/{x_0}\right)^4} \text{ when } abs(x) > 60 \text{ km and } x_0 = 30 \text{ km}$$

$$D(x) = 1 \; when \; abs(x) < 60 \text{ km}$$

Then the initial shear stress is related to the initial normal stress in the reference models as,

$$\frac{\tau}{\sigma_n} = (\mu_d + \alpha) D(x) D(z)$$

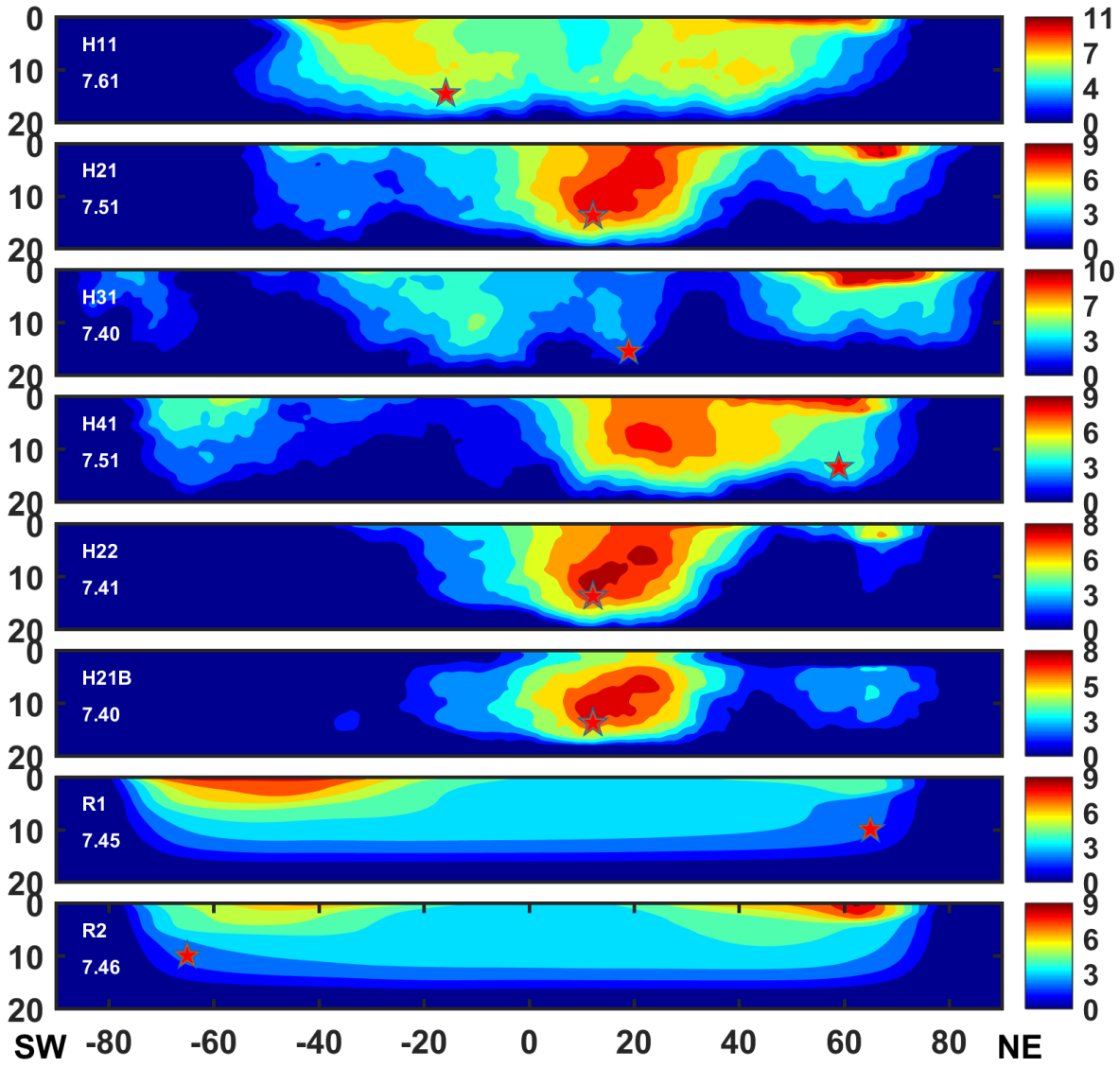

Figure 3.4 Distributions of computed final slips (m) of all scenarios. The model names and magnitudes are labeled at the left side of each panel. Stars represent hypocenters.

3.3.4 Initiation of spontaneous rupture, slip-weakening friction law and the choice of D_0

Dynamic rupture is initiated within a circular area with a radius of 4 km to the hypocenter using a time weakening law (e.g., Andrews, 2004). The critical time of 0.4 s is applied to make the nucleation phase smooth. Outside the nucleation patch, rupture propagates spontaneously in

the control of a slip-weakening law (Ida, 1972, Day, 1982). In the slip-weakening law, after reaching the shear strength, shear stress drops in a linear manner over the critical slip distance D_0 and finally stays at the sliding friction level. One issue is how to choose D_0, which is not well constrained by observations. In ground motion simulations, D_0 is generally taken as a constant over the whole fault plane and it ranges from 0.2 m to 1 m (Olsen, 1997, Olsen et al., 2008, Olsen et al., 2009, Oglesby and Day, 2002).

Guatteri and Spudich (2000)'s work shows that under the context of the slip-weakening law, if given a stress drop distribution, it is the apparent fracture energy distribution that controls the rupture velocity and the low frequency ground motions. There is a strong trade-off between the D_0 and the stress excess in determining rupture velocity. They simulate two dynamic ruptures of similar apparent fracture energy but different D_0 and strength excess. The two models generate similar rupture time contours and synthetic seismograms in the low frequency range up to 1.6 Hz. In our work, the minimum shear velocity is cut off at 500 m/s and the spatial discretion of the finite element models is 200 m. It could produce meaningful ground motion up to 0.5 Hz, far less than the 1.6 Hz limit reported by Guatteri and Spudich (2000). In the slip-weakening law, fracture energy G is represented by $G = D_0(\tau_{strengh} - \tau_{sliding})/2$ (e.g., Andrews, 2005), where $\tau_{strengh}$ is the shear strength and $\tau_{sliding}$ is the sliding friction. Since initial stresses have already been constructed by Andrews and Barall (2011)'s scheme, a smaller D_0 means less apparent fracture energy. Therefore, given the shear stresses, a smaller D_0 will allow the models to generate larger rupture velocities and larger ground motions. In this study, we try to put an upper bound to the ground shaking in the region. Therefore, a small value of D_0 is preferred.

Another limitation to choosing D_0 is that the spatial resolution of the finite element model should be able to resolve the cohesive zone at the rupture front. Andrews (2005) and Day et al. (2005) develop similar scaling relations between D_0 and the cohesive zone width Λ_0. Here, we refer to the conclusions from 3D dynamic rupture simulations in Day et al. (2005), that the element size should resolve the cohesive zone width $\Lambda_0 = 0.883\mu^* D_0/\Delta\tau$. Given the shear modulus μ and Poisson ratio ν, $\mu^* = \mu$ for Mode III shear crack and $\mu^* = \mu/(1-\nu)$ for Mode II shear crack. $\Delta\tau$ is the stress drop. Taking the rupture propagation into account, the cohesive zone width $\Lambda = \Lambda_0({}^{2L_0}/_{L})/(1 + ({}^{L_0}/_{L})^2)$, where L_0 is the critical length of the initiation patch and L is the distance a rupture has propagated. It indicates that the cohesive zone will shrink with rupture propagation. In 3D strike-slip ruptures on a vertical planar fault, both Mode II and Mode III cracks are involved. Since the μ^* of Mode III crack is smaller than that of Mode II crack, we here discuss the spatial resolution of the cohesive zone based on Mode III crack and derive a lower bound of D_0 for our models.

We select an on-fault station at x=0 km along the strike and z=10 km in depth, which is a typical hypocenter depth of earthquakes in NCB. In the reference models, the stress drop and the shear modulus at this station are 6.70 MPa and 3.664×10^4 MPa, respectively. In a heterogeneous model H21, the stress drop is 10.53 MPa. As shown in Figure 3.4, in heterogeneous models (model names starting with H), asperities (large slip patches) may extend 20 to 50 km horizontally. Given $\mathrm{L_0} = 4$ km and $\Delta\tau = 10.53\ MPa$, if we assume that the rupture propagates $\mathrm{L} = 50$ km (i.e., the maximum size of asperities) and that the cohesive zone still could be resolved by at least one element, say $\Lambda = 200$ m, the minimum D_0 required would be around 0.40 m. With the stress drop of 6.70 MPa in the reference models, this value of $D_0 = 0.4\ m$ will resolve the cohesive zone for a longer rupture (i.e., longer than 50 km) up to about 80

km propagation distance. Therefore, the value of $D_0 = 0.4\,m$ is enough to resolve the cohesive zone for heterogeneous cases, but it may sacrifice some accuracy in the later part of ruptures (i.e., after 80 km propagation distance) in the reference models. It's worth to point out that at shallower depth, although the shear modulus decreases toward the free surface, the stress drop decreases at a faster rate and the cohesive zone width increases at shallow depth. Therefore, to make results of heterogeneous cases and reference models comparable, we chose $D_0 = 0.4\,m$ in most of our models. To test sensitivity of rupture dynamics and ground motions to D_0, we also run some models with a larger D_0, such as Model H22 with $D_0 = 1$ m.

In each scenario, D_0 is kept constant over the fault plane, thus the fracture energy generally follows the depth dependency of normal stress and lies between 10^2 to 10^6 J/m^2, consistent with previous studies (Guatteri and Spudich, 2000). Although Andrews and Barall (2011) suggest that fracture energy or friction coefficients may fluctuate self-similarly, in the current stage we do not make extra efforts to consider this complexity.

3.4 Results

3.4.1 Complex rupture behaviors generated by self-similar stresses

Figures 3.4, 3.5, 3.6 and 3.7 show accumulated slip, stress changes calculated at the end of simulations, rupture time contours and peak slip rates, respectively, for 8 scenarios listed in Table 3.1. We remark that peak slip rates are reliable within 0 ~ 0.5 Hz in these models.

In the heterogeneous cases, the hypocenters are located where the maximum stress drops are, as suggested by Andrews and Barall (2011). We also try to set the hypocenters arbitrarily, but we find that most of these ruptures cannot propagate outside the initiation patch due to the heterogeneity of initial stresses. The phenomenon appears to be common when applying heterogeneous stresses in spontaneous dynamic rupture models (Oglesby and Day, 2002).

Therefore, the maximum stress drop location may be the best location to initiate ruptures for heterogeneous stress scenarios. A total of 8 heterogeneous stress states are generated, but only 4 of them can break most of the fault area. We report those ruptures that can break most of the fault area in this study, as we are interested in ground motions expected from large earthquakes on the Tianjin seismic gap. As shown in slip distributions in Figure 3.4, rupture lengths of all the heterogeneous models stay within 160 km, indicating the practically chosen 180 km long fault model works well. Slip distributions show irregularities as observed in kinematic source inversions of recent large earthquakes such as the 1992 Landers earthquake (e.g., Mai and Beroza, 2002). Without special efforts to make asperities, as the 'asperity case' in Andrews and Barall (2011), we still observe many asperities (large slip patches) at various depths in these models. The asperities at deep portion of the fault (approximately below 3 km) are caused by large stress drops there. While at shallow depth, the asperities mainly occur in the Basins III and/or IV due to low rigidities, though the stress drops there are very small.

Shear stress increases significantly where the ruptures arrest naturally, as shown by the stress changes in Figure 3.5 as negative extremes. In these plots, stress drops are positive and stress increases are negative. For better visualization, the stress increase is truncated at -30 MPa for the heterogeneous models and at -7 MPa for the reference models, respectively.

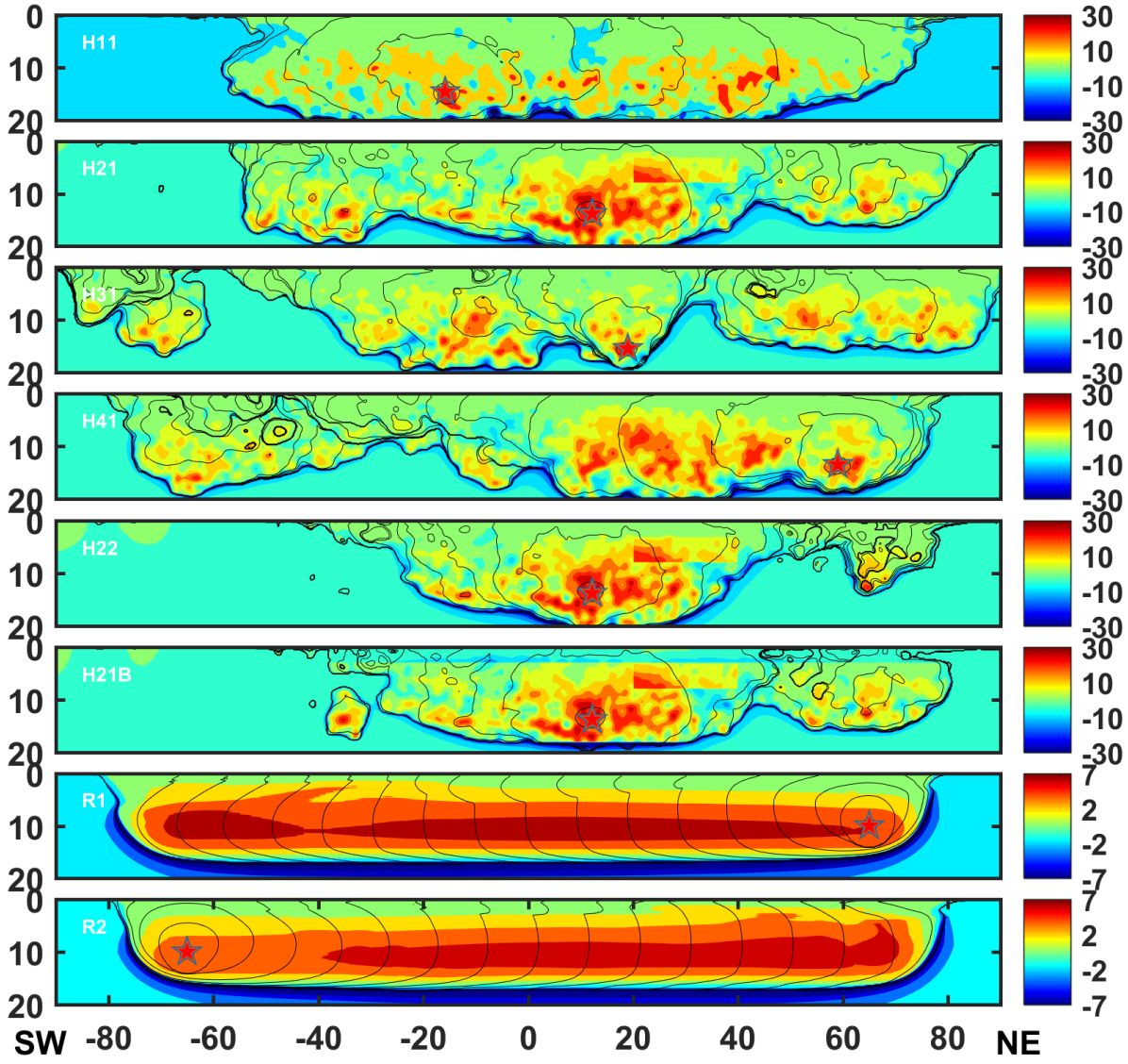

Figure 3.5 Stress changes (MPa) computed at the end of simulations of all scenarios. The stress changes are overlaid by rupture time contours. Positive value represents stress drop. Stress increase is truncated at -30 MPa in the heterogeneous models and -7 MPa in then reference models for better visualization. Stars stand for hypocenter locations. Jumped/triggered ruptures tend to occur at locations where stress drops are relatively high.

Rapid rupture within high stress-drop patches, jumped/triggered rupture at low/high stress-drop boundaries, delayed/paused rupture around low or negative stress-drop patches, and

spontaneous arrest of rupture by a wide area with low or negative stress-drop are complex rupture features in our self-similar heterogeneous stress models.

Delayed/paused ruptures and jumped ruptures in heterogeneous stress models are analyzed by Day (1982). In his problem III, a low stress-drop ($\Delta\tau = 2.5$ MPa) background is intervened by several high stress-drop rectangular patches ($\Delta\tau = 10$ MPa) of dimensions of 2.25 km. The high stress-drop patches are separated at an interval of 1.025 km. Under the context of the slip-weakening law, ruptures propagate quickly within the high stress drop patches and decelerate when they approach the high/low stress-drop boundaries, forming a pattern of condensed rupture time contours. These delayed/paused ruptures are widely observed in our simulations, as indicated by arrows with thick bars in Figure 3.6. The rupture recommences when it jumps to an adjacent high stress-drop patch, leaving unbroken fault behind and multiple fault areas rupturing at the same time. We name these phenomena as jumped ruptures, which are less than a few kilometers (typically hundreds of meters) ahead of the main rupture front and are represented by small circles in rupture time contours and indicated by arrows with dashed bars in Figure 3.6.

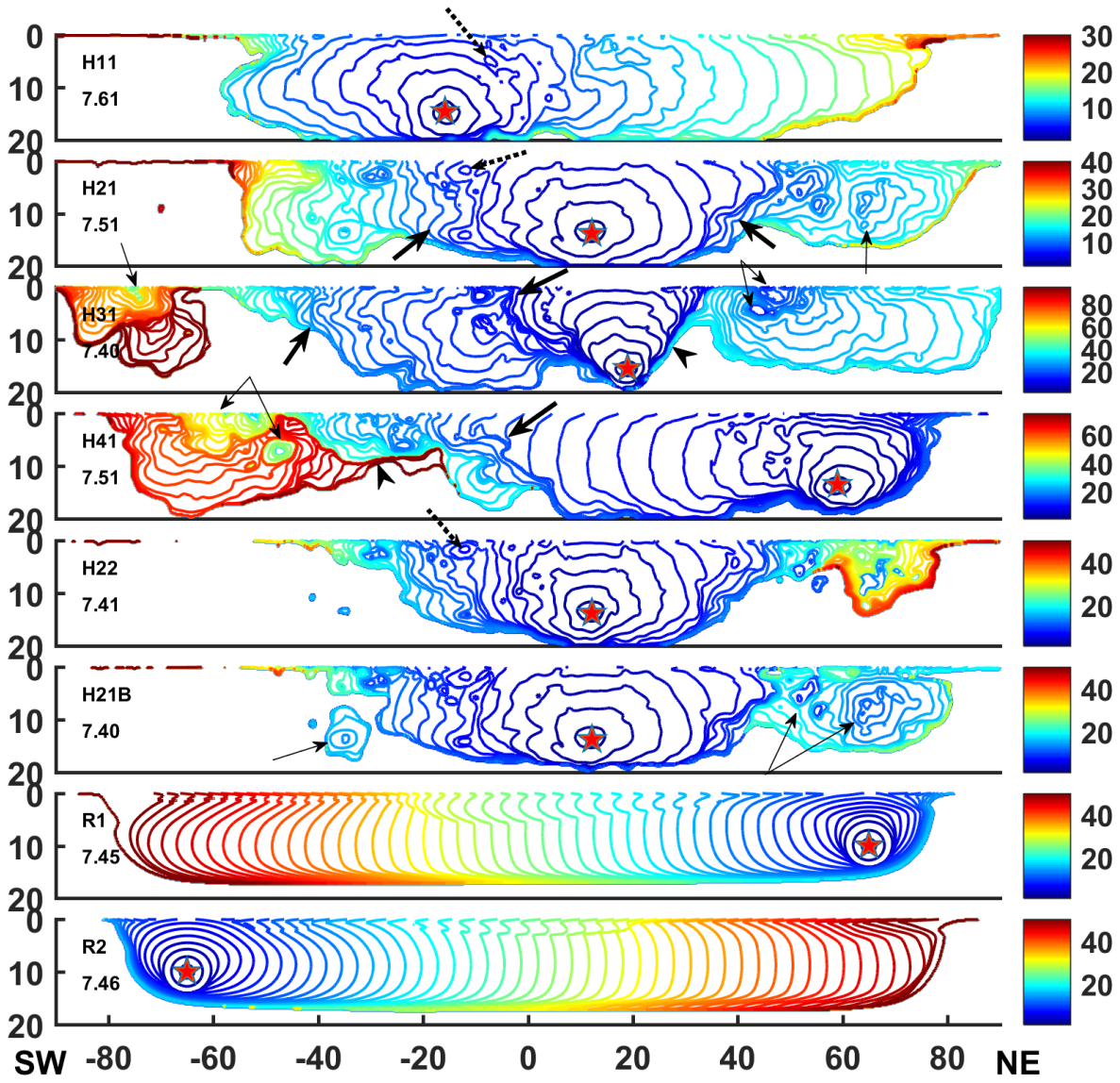

Figure 3.6 Rupture time contours of all scenarios. The model names and the magnitudes of events are given in each panel. The rupture durations vary from 23 s to 95 s for the heterogeneous models due to stress heterogeneity. Arrows with thick bars, arrows with dashed bars, arrow heads and arrows with thin bars represent delayed/paused ruptures, jumped ruptures, ceased ruptures and triggered ruptures, respectively.

Based on the results in Day (1982), the rupture from a high stress drop patch will penetrate low stress drop background. The intervals between high stress-drop patches should be slightly less than half length of dimensions of high stress-drop patches for the rupture to jump

across a low-stress patch. It explains why jumped ruptures are less than a few kilometers ahead of the rupture front in our simulations, since the dimensions of high stress drop patches in the heterogeneous models generally give a penetration distance less than a few kilometers. If the low/negative stress-drop area is too wide compared to the penetration distance, the rupture will arrest spontaneously, as indicated by arrow heads in Figure 3.6. In these self-similar heterogeneous stress models, we also observe that ruptures can be triggered ahead of a main rupture front up to tens of kilometers. We name these ruptures as triggered ruptures, as labeled by arrows with thin bars for models H21, H31, and H41 in Figure 3.6, which also show closed, circular rupture time contours ahead of the main rupture front as jumped ruptures do. These triggered ruptures are caused by seismic waves in these self-similar initial stress fields. The triggered ruptures usually lead to sub-events which extend the total rupture length of an earthquake, as shown to the SW end of the ruptures in the models H31 and H41.

Because of the complexities in rupture processes, rupture durations vary greatly among different scenarios. As shown by rupture time contours in Figure 3.6, rupture durations of the four heterogeneous scenarios are about 23, 34, 95 and 72 s, respectively. We describe some noticeable features in rupture propagation of the four self-similar scenarios below.

In H11, the rupture propagates rapidly to the SW in the first 11 s and to the NE in the first 20 s. The rupture slowly breaks the fault near the NE free surface until 23 s.

In H21, the rupture propagates rapidly to the SW in the first 24 s and to the NE in the first 20 s. The rupture slowly breaks the fault near the SW free surface between t=24 s and t=34 s. At t=10.64 s, the rupture jumps ahead of the major rupture front at the NE portion of the fault, as indicated by the arrow with a thin bar. It propagates southwestwards to meet the major rupture front at t=13.41 s and also propagates northeastwards up to t=15 s.

In H31, the rupture propagates continuously to the SW in the first 43 s, while temporarily ceases to the NE at about 13 s. Two ruptures are triggered at t=9.38 s and at t=17.58 s to the NE, as indicated by arrows with thin bars. The triggered ruptures propagate slowly toward the NE until t=38 s and also propagate back to the SW to meet the previously ceased rupture at t=33 s. On the SW end of the fault, a rupture is triggered near the free surface at 36.83 s as shown by the arrow with a thin bar and is paused immediately after the triggering. A second triggering episode happens just below the previously triggering location at 46.69 s. Finally, at t=63.23 s, a third triggering episode just below the second triggering location propagates to the SW end up to t=73 s. In addition, another triggering episode occurs at x=-72.6 km and z=6.6 km at t=86.77 s, breaking the deeper portion of the SW end and forming the last sub-event in this scenario. These complex triggering episodes typically start where the previous ruptures cease, which indicates the stress heterogeneity inherited from the earlier ruptures will affect the following rupture behavior, even during the short period of a dynamic event.

In H41, the rupture quickly propagates to the NE in the first 20 s and to the SW in the first 17 s. The rupture slows down significantly in the region -15 km <x<0 km and z>10 km. It recommences at x=-8.4 km and z=12.8 km at t=24.22 s and breaks the deeper portion during the period from t=24.22 s to about t=28 s. Finally, the rupture restarts at x=-62.2 km and z=7.2 km at t=57.28 s and breaks the deeper SW portion and propagates up to about t=72 s.

Day (1982) demonstrated the close relationship between the rupture velocity and peak slip rate. We overlay rupture time contours on top of peak slip rates in Figure 3.7. The coarser the contour lines are, the faster the rupture velocity is. The locations of large peak slip rates generally show fast rupture velocities. Peak slip rates over 8 m/s stays below the 5 km depth. At

depths above 5 km, the rupture velocity may be as fast as that at deeper part, but peak slip rates are relatively low due to small stress drops at shallow depths.

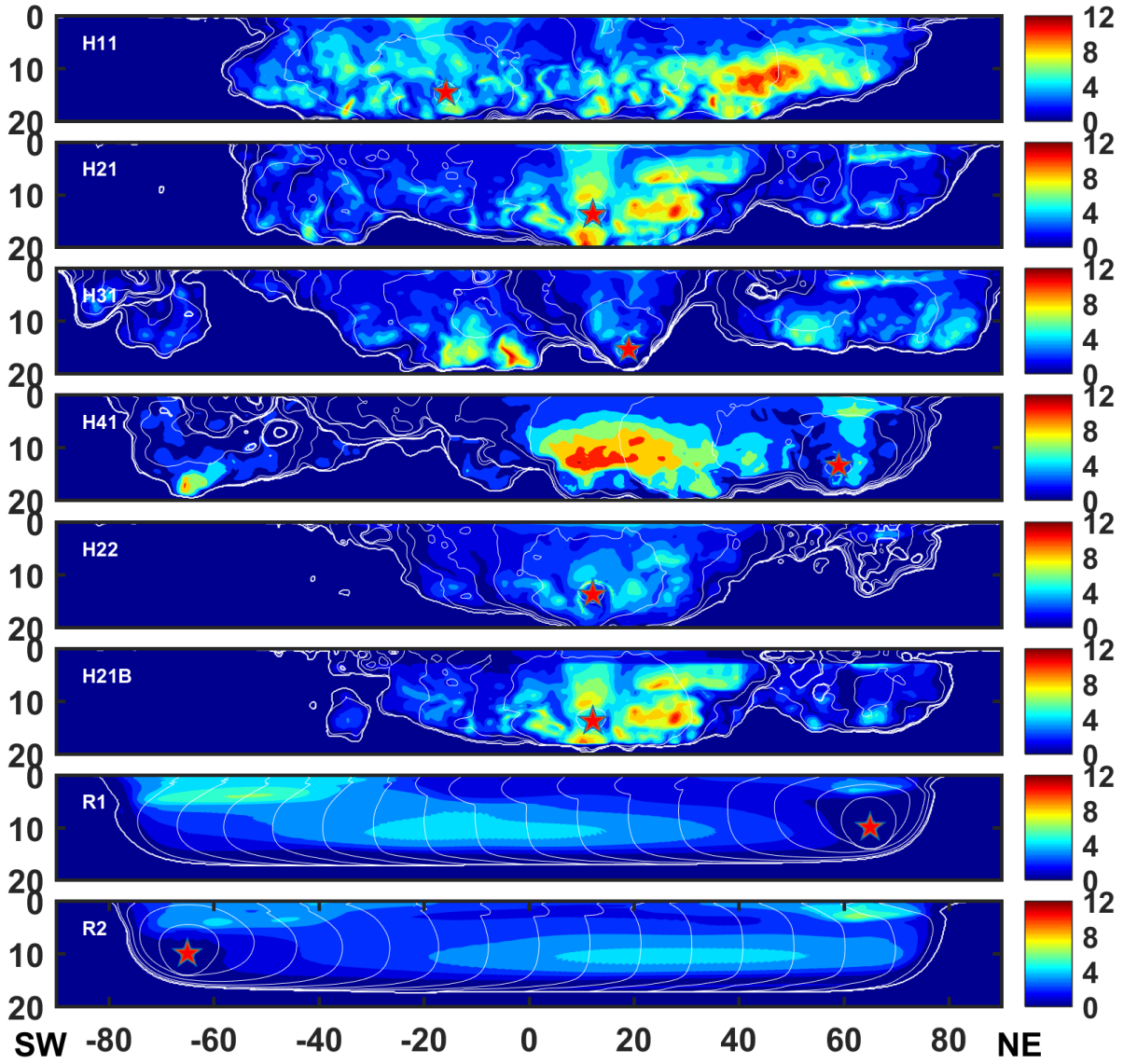

Figure 3.7 Distributions of peak slip rates on the fault of all scenarios. Rupture time contours are overlaid. Stars stand for hypocenter locations.

In H41, because its hypocenter location is close to the NE end of the fault, this event may produce the directivity effect in ground motions as the reference models do. However, the

heterogeneous initial stress makes it difficult for the rupture to maintain the smoothness over the whole fault. We believe that these complex rupture behaviors are common under self-similar heterogeneous initial stress conditions.

H21, H31 and H41 consist of several sub-events caused by triggered ruptures. Triggered ruptures occur frequently in the self-similar heterogeneous models. Most of them only break a small area, but some of them break a large area, leading to an increase of tens of kilometers in the final rupture length.

3.4.2 Dynamic ruptures of the reference models

The two reference models are different only by their hypocenter locations. The hypocenters are close to one end of the fault to account for as much directivity effect in ground motion as possible, as did in previous studies (Olsen et al., 2008, Olsen et al., 2009). As shown in Figure 3.6, their rupture propagations are much smoother than those of the heterogeneous models. The ruptures slow down relatively at the two low velocity sedimentary basins (Figure 3.6). The peak stress drop, about 7 MPa, is much smaller than the 30 MPa in the heterogeneous cases. It results in the maximum slip-rate (about 4.8m/s) in the reference models that is about 40% of those in the heterogeneous cases (about 11 m/s). Ruptured areas are much broader than those in the heterogeneous cases. Even though the peak slip-rates of the reference models are much smaller than those of the heterogeneous models, the smooth ruptures will generate strong ground shakings due to the directivity effect comparable in amplitude to ground motions in the heterogeneous models, in which strong ground motions are primarily induced by the large slip-rates of asperities. But the ground motions from the two types of events have some fundamental differences, which will be discussed in the next two sections.

For all the earthquake events simulated, the magnitudes vary narrowly from 7.40 to 7.61. Therefore, the moments are similar. The reference and heterogeneous models may represent two extremes of the potential earthquakes, given a targeted magnitude. Among the models, H21 has been considered as the worst scenario for Tianjin in terms of ground shaking hazard, because of the large asperity located directly beneath Tianjin. Similar to the "worst" case in Duan *et al.* (2017), the sliding frictional coefficient is reduced to 0.5 in a rectangular area right beneath Tianjin, as shown in Figure 3.5(b).

3.4.3 Peak ground velocity distributions and the directivity effect

Figures 3.8 and 3.9 show the fault-parallel and fault-normal peak ground velocity (PGV) distributions of scenarios H11 ~ H41, R1 and R2, respectively. Peak ground velocities, which are reliable within 0~0.5 Hz, are directly picked as the maximum absolute value of velocity synthetics at each station with no filter applied. The fault-parallel PGVs dominate in the heterogeneous models, as shown in Figure 3.8, while the fault-normal components dominate in the reference models in the direction of rupture propagation, as shown in Figure 3.9. In the reference models, the ruptures are smooth over the whole fault, which can effectively generate the directivity effect (Somerville et al., 1999), often observed in near-fault fault-normal ground motion recordings. However, the directivity effect cannot be efficiently induced in heterogeneous stress models, because ruptures accelerate and decelerate frequently due to the stress heterogeneity. Ruptures at different portions of the fault cannot communicate well and the rupture process is primarily controlled by local stress drops. Similar to that observed by Oglesby and Day (2002), the increase in initial stress heterogeneity is in favor of a decrease in the directivity effect.

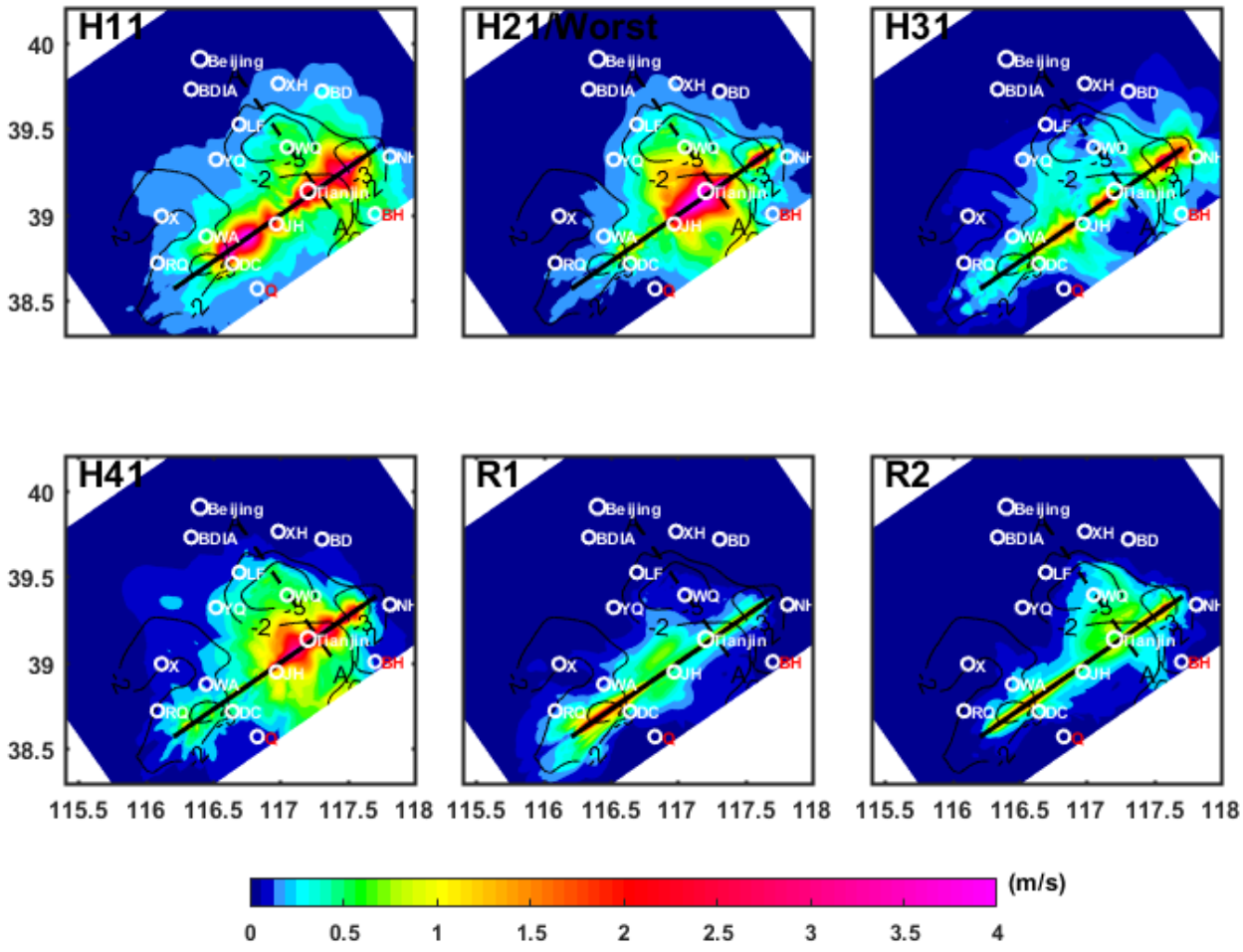

Figure 3.8 Peak fault-parallel ground velocity of H11, H21, H31, H41, R1 and R2. The thick solid line represents the seismic gap simulated in the study. Major cities or sites are depicted as white circles with the same notations as in Figure 3.1. Black contours are isosurfaces of Vs=1.5 m/s at 2 and 3 km depths to outline the basins.

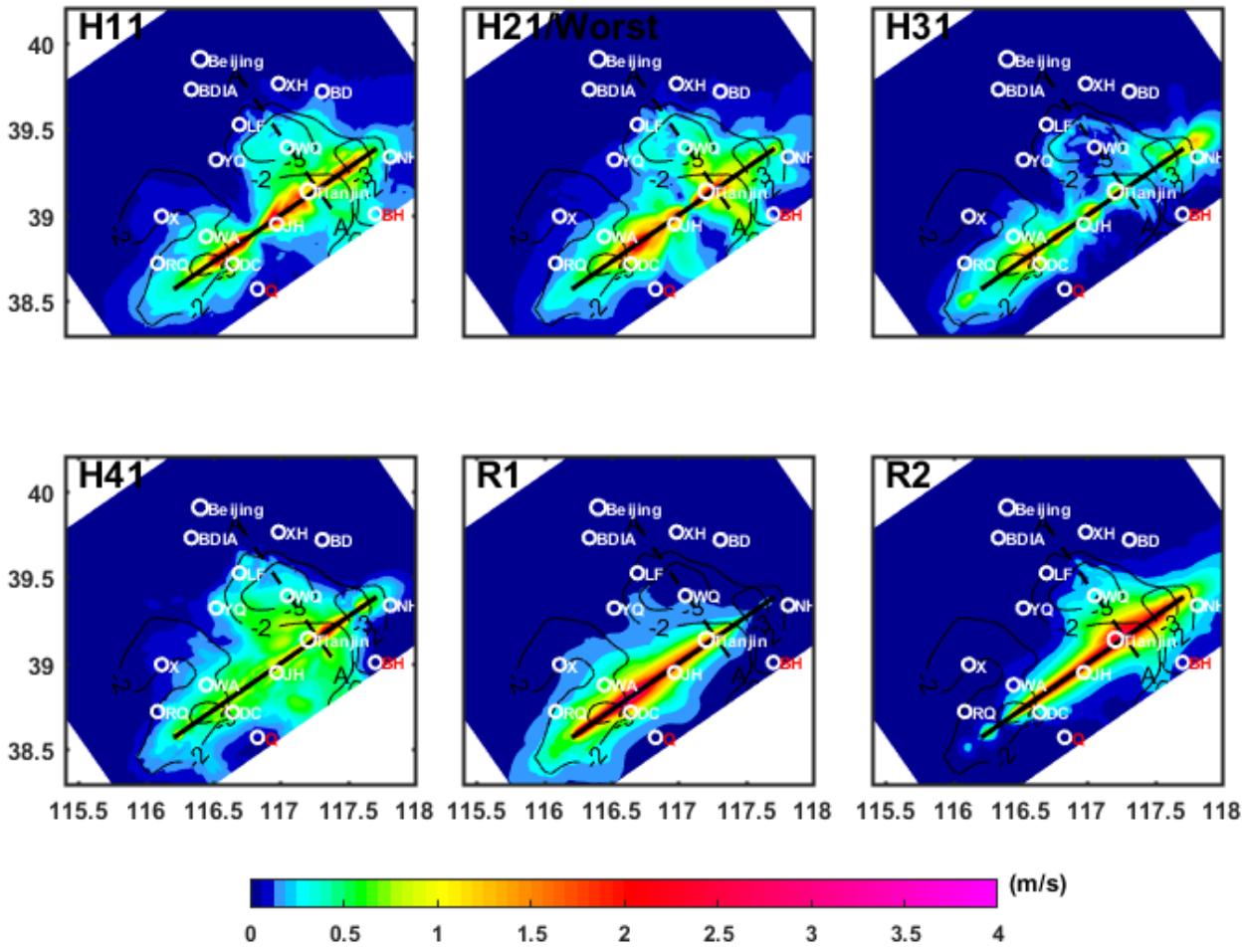

Figure 3.9 Peak fault-normal ground velocity of H11, H21, H31, H41, R1 and R2. The thick solid line represents the seismic gap simulated in the study. Major cities or sites are depicted as white circles with the same notations as in Figure 3.1. Black contours are isosurfaces of Vs=1.5 m/s at 2 and 3 km depths to outline the basins.

In terms of affecting areas of ground motion, heterogeneous ruptures generally have a broader impact than the reference models do. Even though the heterogeneous ruptures have smaller ruptured areas compared to the reference models, the high stress drop patches result in larger peak slip-rates, which allow heterogeneous ruptures to affect broad areas off the fault. An exception is Model H31, in which the large stress drop patches are scattered and not well connected in space, as shown in Figure 3.5 (c). As a result, the peak slip rates (Figure 3.7 (c)) are

considerably less than those of H11 (Figure 3.7 (a)), H21 (Figure 3.7 (b)) and H41 (Figure 3.7 (d)). Therefore, the PGV maps of H31 show reduced ground shaking compared with those of the other heterogeneous models, especially in the fault-normal component around Basin I, as shown in Figure 3.9 (c).

3.4.4 Basin effects

Basins amplify and prolongate ground motion, whose amplitude depends upon basin depth, basin shape and frequency contents of ground shaking (e.g., Day et al., 2008b). In the study region, four basins exist (Figure 3.1). We analyze the basin effect along the profile AA' that passes through the off-fault Basin I.

Day et al. (2008b) have found that the spectral acceleration amplification increases with increasing periods from 2 to 10 s and with increasing basin depth defined by the isosurface of Vs=1.5 km/s. Here we pick evenly distributed stations along Profile AA' and present their fault-parallel and fault-normal Fourier amplitude spectra of velocity synthetics for both heterogeneous and reference cases in Figure 3.10. The Fourier amplitude spectra are averaged separately for the heterogeneous and reference cases. Using Vs=1.5 km/s as the predictor for basin structure, the major portion of Basin I along the profile AA' approximately locates from 20 to 60 km off the fault (Figure 3.1 (a)).

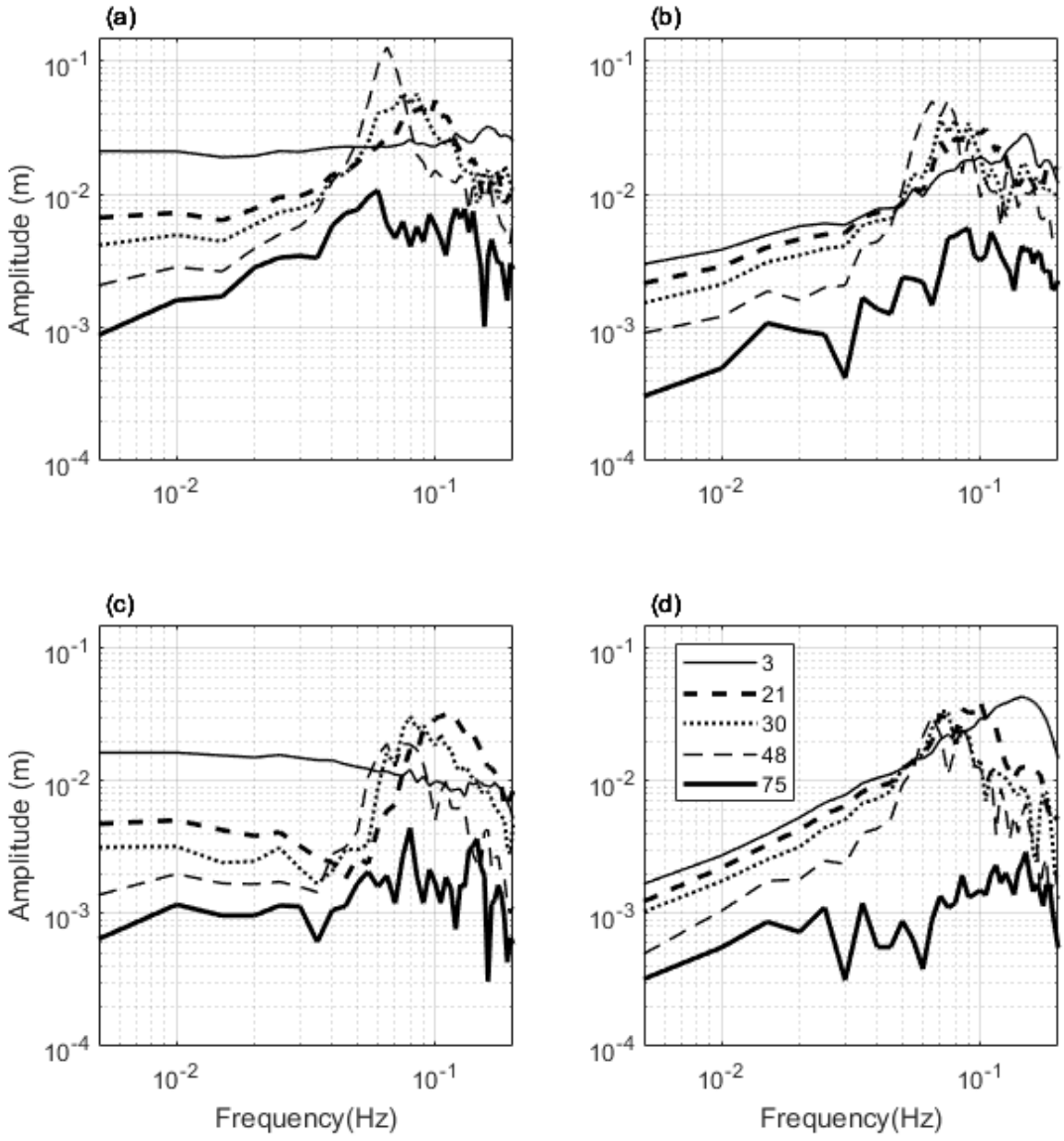

Figure 3.10 Amplitude spectra of synthetic velocities at stations along profile AA'. The numbers in the legend show how far stations are off the fault to the NW in the unit km. (a) Fourier amplitude spectra of the fault-parallel component averaged over H11, H21, H31 and H41. (b) Fourier amplitude spectra of the fault-normal component averaged over H11, H21, H31 and H41. (c) Fourier amplitude spectra of the fault-parallel component averaged over R1 and R2. (d) Fourier amplitude spectra of the fault-normal component averaged over R1 and R2.

Figure 3.10 (a) shows the Fourier amplitude spectra of the averaged fault-parallel component of the four heterogeneous models. Moving away from the fault, the peak amplitude starts to stand out at the station 21 km off the fault and the frequency of the peak is about 0.1 Hz. The peak amplitude increases and migrates towards lower frequencies further off the fault toward the center of Basin I. The extreme is reached at the center of the basin at the distance of 48 km off the fault and the frequency of the peak is at 0.065Hz. Moving outside of the basin, the peak amplitude starts to drop dramatically. The Fourier amplitude spectra of the fault-normal velocity synthetics show a similar trend with smaller amplitudes, as shown in Figure 3.10 (b). In the heterogeneous models, the peak amplitude in the amplitude spectra of the fault-parallel component is largest at the center of Basin I, where the basin is deepest. Away from that extreme, the peak amplitude decreases with decreasing basin depth, which is consistent with the results of Day et al. (2008b).

Figure 3.10 (c) and 10 (d) show the Fourier amplitude spectra of the fault-parallel and fault-normal velocities averaged over the two reference models at the various stations, respectively. The peak amplitudes of the fault-parallel components are less than those of the heterogeneous models, especially at the stations at the center of the basin. The peak amplitudes at the stations ranging from 12 ~ 48 km off the fault are at a similar level. For the fault-normal component, the extreme is reached just 3 km off the fault at the high frequency end of the spectra, which results from the directivity effect. The Fourier amplitude spectra of stations 21 km or further off the fault are similar to those in the heterogeneous models, indicating that the directivity effect mainly affects the spectra of stations close to the fault (less than 21 km off-fault). The off-fault basin structure will determine the Fourier amplitude spectra of stations inside the basin.

The amplification also depends on amplitudes of slip-rates, the direction of rupture propagation and relative locations between a basin and large slip-rate patches. In all heterogeneous models and R1, in which Basin I is located along the direction of rupture propagation, Basin I amplifies ground motion significantly. Compared to Basin I, Basin II is much smaller and shallower (Figure 3.1). Therefore, the basin effect is significantly reduced, and the amplifications are much less than Basin I.

The seismic gap passes through the Basin III and IV. The PGVs are strongly affected by the frictional behavior of low velocity sediments at shallow depth and by the free surface. We will discuss their amplification effects together with a buried rupture in the section “the effect of buried rupture”.

3.4.5 Velocity and displacement synthetics at selected stations

In this section, synthetic particle displacement and particle velocity at 3 stations TJRS, B3Center and WQ are shown with different characteristics in waveforms. Figure 3.11 shows synthetics at Tianjin railway station (TJRS), which is close to the fault trace and is outside the four basins. The waveforms show strong velocity pulses of large amplitudes and short durations. The permanent fault-parallel displacements vary from 1 to 4 m among different scenarios.

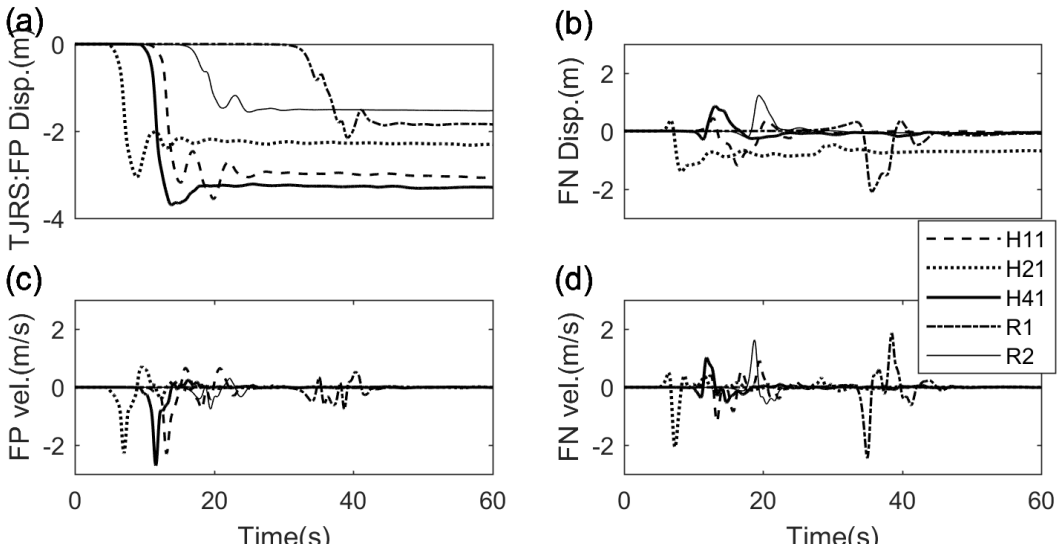

Figure 3.11 Synthetic particle displacements and particle velocities at the off-fault station TJRS. FP and FN stand for fault-parallel and fault-normal, respectively. (a) Fault-parallel displacements; (b) fault-normal displacements; (c) fault-parallel velocities and (d) fault-normal velocities. Since the station is close to the fault, the scenario earthquakes cause permanent slips varying from 1 to 4 m. The velocity synthetics show characteristics of pulses with large amplitudes and short durations.

Figure 3.12 shows synthetics at the station B3Center, which is also close to the fault trace and is located at the center of Basin III. The scenario earthquakes cause permanent fault-parallel displacement varying from 0 to 3 m. The fault-parallel velocity synthetics show short-duration strong pulses. The fault-normal velocity synthetics exhibit long-period waves of large amplitudes that last tens of second. In terms of the amplitudes of displacements and velocities, the reference models produce larger amplitudes of displacements and velocities than the heterogeneous models, due to the coupling of the directivity effect and the basin effect in the reference models.

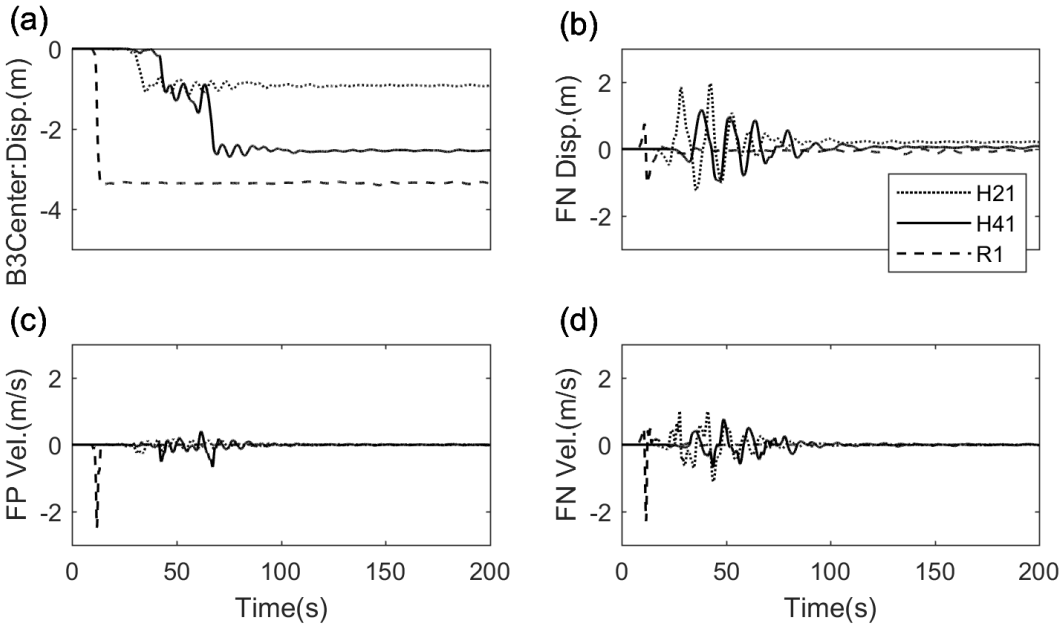

Figure 3.12 Synthetic particle displacements and particle velocities at the off-fault station B3Center. FP and FN stand for fault-parallel and fault-normal, respectively. (a) Fault-parallel displacements; (b) fault-normal displacements; (c) fault-parallel velocities and (d) fault-normal velocities. Since the station is close to the fault, the scenario earthquakes cause permanent fault-parallel displacement varying from 0 to 3 m. The fault-parallel velocity synthetics show short-duration strong pulses, while the fault-normal velocity synthetics is characterized by long-period waves of large amplitudes that last tens of seconds. The reference models produce larger displacements and velocities than the heterogeneous models.

Figure 3.13 shows synthetics at Station WQ, which is at the center of Basin I. The waveforms show seismic shaking with durations up to 150 s dominated by long period basin-induced surface waves. The shape and dimensions of Basin I are similar to the Los Angeles basin in southern California, where 150 s long shaking has been found in TeraShake2 (Olsen et al., 2008). It indicates the basin dimension and shape affect the duration of seismic shaking. When moving from the center of the basin to the basin edges, the prolongation of seismic shaking is alleviated. For example, at station LF, the durations are reduced to about 70 s (not shown).

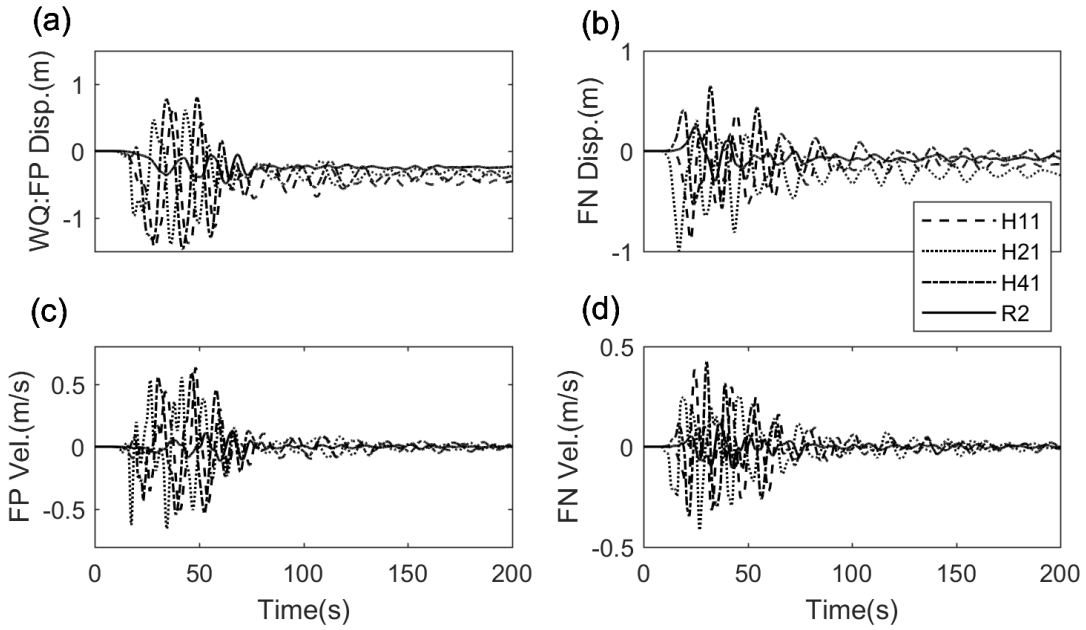

Figure 3.13 Synthetic particle displacements and particle velocities at the off-fault station WQ, which is located at the center of Basin I. FP and FN stand for fault-parallel and fault-normal, respectively. (a) Fault-parallel displacements; (b) fault-normal displacements; (c) fault-parallel velocities and (d) fault-normal velocities. The waveforms feature long period shaking of durations up to 150 s.

3.5 Discussion

3.5.1 The effect of buried rupture

Because in NCB low velocity sedimentary basins exist at shallow depth, which may be frictionally stable (velocity strengthening) due to the existence of unconsolidated granular material (Scholz, 1998, Oglesby and Day, 2002), a buried model, H21B, is developed to explore the effect of buried ruptures on ground motion. Also, observations in NCB may be in favor of buried ruptures. For example, aftershock distribution reveals that the sub-surface faulting of the 1976 Tangshan earthquake extended approximately 140 km, while evidences show the surface rupturing within Tangshan city was only about 10 km, exhibiting limited surface ruptures (Liu et al., 2002). Most historical earthquakes in NCB lack of surface ruptures (Xu et al., 2002).

Therefore, we design model H21B to explore the effect of buried rupture on ground shaking. Under the context of the slip-weakening law, slip-strengthening has been used to reproduce the frictionally stable behavior of weak layers (Day and Ely, 2002, Pitarka et al., 2009, Duan, 2012). Day and Ely (2002) reproduce results of foam rubber strike-slip models of Anooshehpoor and Brune (1994) with numerical simulations. They raise the dynamic friction for the weak layer (physically modeled by a plastic between the foam rubbers) to the static friction level, which means no stress drop and an infinite D_0. Duan (2012) uses a dynamic friction coefficient larger than static friction at shallow depth to limit surface rupturing in the 2011 Tohoku-Oki earthquake.

In H21B, above 3 km depth, we increase the dynamic friction coefficient to 0.9, larger than the static friction coefficient, which creates a negative stress drop zone at shallow depth. Different than the focus in Pitarka et al. (2009), in which they try to explain different frequency responses of ground motion from surface ruptures and buried ruptures, we want to figure out contributions to PGVs from shallow rupturing in heterogeneous models. Therefore, other parameters in H21B are kept the same as in H21.

Comparing H21B with H21 in Figures 4 and 6, we can see that the slip-strengthening at shallow depth in H21B significantly suppresses the accumulated slip and peak slip rates in the weak layer. In addition, slip-strengthening impedes the rupture to propagate to the southwestern portion of the fault.

Figure 3.14 (a) presents the subtraction of peak horizontal velocities (PHVs) of H21B from H21. The PHV at a station is computed as the maximum geometric mean of fault-parallel and fault-normal horizontal velocities. At the northern portion of the rupture, the slip-strengthening in shallow depth leads to less ruptured area in H21B and the effect of buried

rupture on PHVs is in the vicinity of the fault trace. The maximum PHV of H21 is 5.79 m/s, which should be considered as the upper bound neglecting off-fault plasticity, while it is reduced to 4.36 m/s in H21B, a 24.70% reduction. All these peaks lie on the fault trace. Therefore, the weak layer only reduces the peak horizontal velocities in the close vicinity of (several km off) the fault. Therefore, the majority results above without slip-strengthening at shallow depth still hold, except that the surface rupturing slip and PGV in the close vicinity of the fault might be reduced. At the southwestern portion of the fault, the weak layer impedes the rupture progressing southwestwards as discussed above, which causes reduction in peak ground velocity over a broad region, including cities DC and WA.

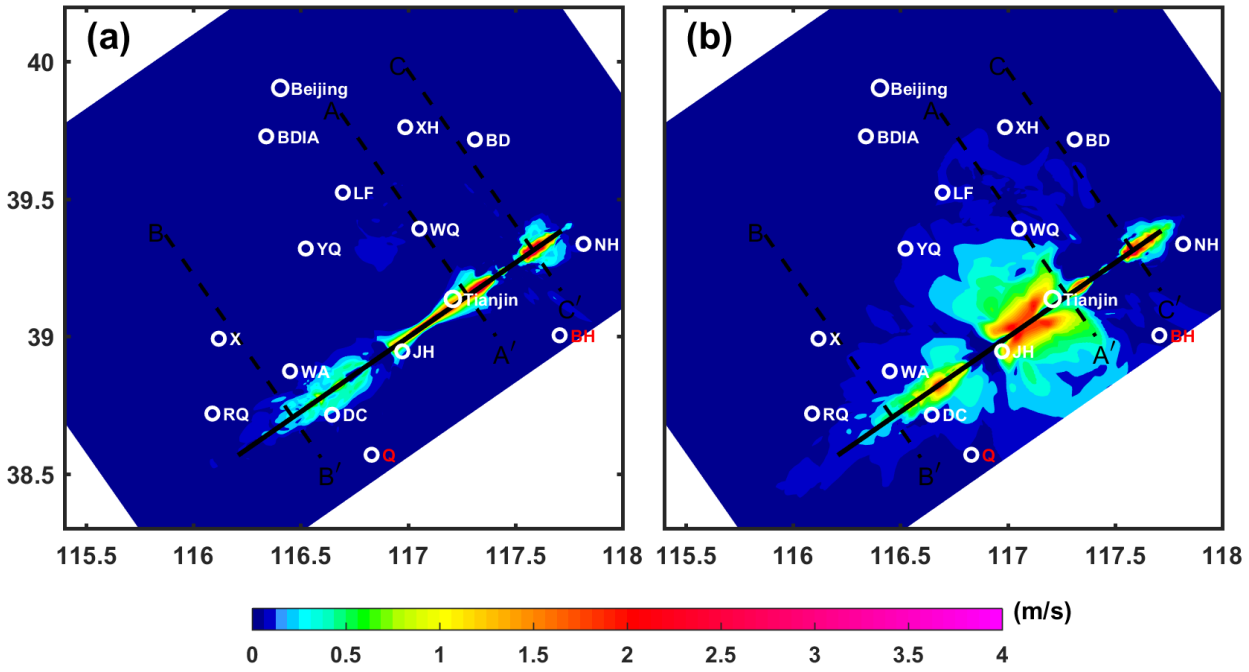

Figure 3.14 (a) Subtraction of peak horizontal velocities of H21B from H21. The H21B is a buried rupture with slip-strengthening above 3 km depth. Other parameters in H21B are the same as those in H21. (b) Subtraction of peak horizontal velocities of H22 from H21, where H22 has a larger slip-weakening distance D_0=1 m.

3.5.2 The effect of increased D_0 on rupture propagation and ground motion

We design model H22 with D_0 =1 m to explore the effect of increasing D_0 on rupture propagation and ground motion. Figure 3.14 (b) shows the subtraction of PHVs of H22 from H21. Comparing slip magnitude and rupture times contours between the two scenarios (Figures 4 and 5), the larger D_0 slows down the rupture propagation towards the free surface, resulting in smaller slip and a smaller rupture area in H22.

Peak slip-rates of H22 are significantly reduced comparing with those of H21 and are at a similar level to those of the reference models (Figure 3.7). As a result, the maximum PHV of H22 decreases from the 5.79 m/s of H21 to 4.82 m/s and the PHVs of H22 are reduced over a large area as far as WQ and YQ, because of the reduction of slip-rates on the asperity beneath Tianjin. It indicates that an increase in D_0 is in favor of a decrease in slip-rates and resultant PHVs.

3.5.3 Rupture roughness and directivity effect

Previous studies have shown that rupture roughness may reduce the near-fault directivity pulses (Oglesby and Day, 2002, Day et al., 2008a). Oglesby and Day (2002) find that their rough strength models show less-developed directivity pulses. Day et al. (2008a) indicate that rupture complexity may explain the diminution of the short-period directivity effect from ground motion observations (Somerville et al., 1997). Following Oglesby and Day (2002), we compute the mean percentages of the asperity area (with slip larger than 1.5 times the average slip over the fault) over the ruptured area (with slip larger than 0.01 m) of the heterogeneous (H11, H21, H31 and H41) and reference models (R1 and R2), respectively. The averages are 18.83±7.42% and 10.86±1.05%, respectively, and both are larger than 8.4±1.8% of ‘the rough case’ in Oglesby and Day (2002). Our results confirm that increasing roughness will decrease the directivity effect.

Moreover, the percentages of asperities over the ruptured area in our models are closer to the mean percentage of 22% from the observations in Somerville et al. (1999) (ranges from 5% to 40%). In terms of the percentage of asperity over the ruptured area, the heterogeneous models seem to better fit the data than the reference models. In these models, the peak fault-parallel velocities, which are mainly caused by adjacent large slip-rate patches (strongly related to large stress drop areas as shown in Figure 3.5), are larger than the peak fault-normal velocities, which are mainly generated by the directivity effect. Therefore, it appears that the effect of large slip-rate patches dominates over the directivity effect in these heterogeneous models.

3.5.4 Comparison of basin effects to the Southern California area

Basin I in our study area is similar to the Los Angeles basin in southern California in terms of their shape and size. It is a little farther away from the seismic gap, compared to the distance between the Los Angeles basin and the San Andreas fault segment simulated in the TeraShake2 exercises (Olsen et al., 2008). The maximum PGV inside Basin I of all the scenarios are about 0.6 m/s and is much less than the 1.5 m/s PGV inside the Los Angeles basin in TeraShake2. The difference likely results from differences in velocity structures between these two regions. In TeraShake2, the directivity effect and a wave guide passing through San Bernardino-Chino-San Gabriel-Los Angeles basins together lead to the strong localized amplification around Whittier Narrows (WN). In NCB, such kind of energy channel does not exist, because low velocity sediments widely exist over the region surrounding the seismic gap. Seismic wave energy is scattered and cannot be effectively concentrated and transmitted into Basin I.

A close examination shows that WN locates at the edge of the Los Angeles basin and localized amplification tends to occur at the basin edge due to ‘the basin-edge effect’ (Kawase,

1996). Kawase (2003) reviewed basin related waves, including basin-induced surface waves, the edge effect and basin-transduced surface waves. Large velocity contrasts at basin edges will cause diffraction waves, which would be transformed to surface waves in basins in the case of normal incident waves. If the slope of a basin edge is steep, diffracted waves and direct waves will arrive simultaneously and constructive interference will dramatically amplify the ground motion at stations adjacent to the edge in the basin, which is the edge effect discussed by Kawase (1996) to explain the severe damage belt in the 1995 Kobe earthquake. If the input wave is surface wave, basin-transduced surface waves take place. Graves et al. (1998) reported the edge effect in the Santa Monica area during the 1994 Northridge earthquake. In the Santa Monica case, the fault locates 20 km away from the basin edge instead of directly adjacent to the basin in the Kobe's case. The edge effect is also observed in our simulations in NCB. In our simulations, strong localized amplifications occur at the south edge of Basin I, which may be seen in Figure 3.8 (a) and Figure 3.9 (b) and (d).

Compared to the simplified 2D model in Kawase (1996) to explain the narrow severe damage belt, the areas of amplified PGV around Basin I in our study and around the Los Angeles basin in Terashake2 exercises are much broader. The reason is that velocities in high-resolution 3D velocity structures used in both studies vary gradually in space. Therefore, the interface of sharp velocity contrast in the 2D model, which favors narrow belt of localized ground shaking amplification, no longer exists.

Because there is not an energy channel helping concentrate and transmit seismic energy in NCB, Basin I does not show clearly basin effects in R1 (Figure 3.8 (e) and Figure 9 (e)) in which the rupture propagates away from Basin I. This is different from TeraShake2.3 in which the rupture propagates away from the Los Angeles basin but elevated PGVs are observed in the

basin. The difference indicates that the velocity structures play important roles in the resultant PGVs in NCB and in southern California.

3.5.5 The setup of ϵ

In the initial stress setup, the ϵ cannot be set to be arbitrarily large, otherwise the static friction would become unreasonable. In our models, the peak value of functions w is 3.644, which gives rise to a maximum static frictional coefficient of 0.79 with the default $\epsilon = 0.01$.

3.6 Conclusions

We simulate dynamic ruptures on the 160-km-long Tianjin seismic gap in North China Basin and deterministic ground motions up to 0.5 Hz with self-similar heterogeneous initial stresses and high-resolution 3D basin velocity structure. Complex rupture behaviors such as jumped/triggered ruptures and delayed/paused ruptures appear spontaneously in self-similar heterogeneous initial stress models. Triggered ruptures can happen tens of kilometers away from the main rupture front. Although many of triggered ruptures die out quickly, some of them can propagate tens of kilometers. Because of stress heterogeneity, durations of the simulated events on the same fault with the different realizations of self-similar initial stresses vary from 23 to 95 s. Comparing with the reference models with a uniform shear to normal stress ratio on the fault, self-similar stress models produce much larger peak stress drops and peak slip rates on the fault. The average ratio of the asperity area to the total rupture area from the self-similar stress models is about 18.83%, which is closer to the average value of 22% observed from recent large earthquakes, compared to the average value of 10.86% from the reference models.

In the self-similar stress models, the fault-parallel component of PGVs, which is dominated by the adjacent large slip-rate patches, is stronger than the fault-normal component. In the reference models, the fault-normal component is stronger due to the directivity effect. The

existence of the two basins at the two ends of the seismic gap enhances the directivity effect in the reference models. Near the fault and outside of the basins, synthetic waveforms exhibit short and strong velocity pulses, whereas at the center of the deep basin between Beijing and Tianjin (Basin I), long-duration and long-period waves from basin effects dominate synthetic waveforms. The largest peak ground velocity inside Basin I is about 0.6 m/s and the duration of ground motion can last 150 seconds.

The amplification of the Fourier amplitude spectra of the synthetic velocity correlates to the basin depth and the frequency content. In Basin I, the maximum peak amplitude occurs at the center of the basin at frequency 0.065 Hz, corresponding to the deepest basin depth of 3.49 km (by Vs = 1.5 km/s). The peak amplitude decreases with decreasing basin depth and occurs at higher frequencies toward the basin edge.

CHAPTER IV

OFF-FAULT INELASTIC DEFORMATION INDUCED BY DYNAMIC RUPTURES THROUGH A FAULT BEND AND THEIR LINKS TO FIELD OBSERVATIONS

4.1 Introduction

Geological observations demonstrate the structure of mature, large displacement faults including fine granulated fault cores that host the majority of fault slips and surrounding damage zone of fractured rocks extending hundreds of meters off the fault (Chester and Chester, 1998, Caine et al., 1996, Chester et al., 1993). Fault zone trapped waves (Ben-Zion, 1998) present a near-fault low-velocity zone, which is interpreted to have seismic wave velocities reduced to half than those of the surrounding rock. Pure elastic models of dynamic ruptures (Duan and Oglesby, 2005, Andrews, 2005) show that dynamic stresses generally exceed material yielding strength and the material would likely to incur inelastic deformations, which are linked to the fractures in the damage zone (Dunham et al., 2011b, Dunham et al., 2011a, Duan and Day, 2008, Andrews, 2005, Templeton and Rice, 2008). The structural layout of the faults play important roles in determining dynamic ruptures and seismic radiations. Andrews (2005) uses Mohr-Coulomb yielding criterion to model dynamic ruptures of 2D in-plane fault. The inelastic work significantly lifts the fracture energy, which limits the speed of rupture propagation. Given uniform stress drops on the fault, the width of off-fault inelastic deformation is proportional to rupture propagation distance with the inelastic deformation existing on the extensional side. Templeton and Rice (2008) demonstrate with the similar model setup that the angle of the maximum principle stress with respect to the fault strike, the seismic S ratio, and the closeness of the initial stress state to Mohr-Coulomb failure determine the extent and the distribution of off-

fault plasticity. Dunham et al. (2011a) study dynamic ruptures on a similar model but controlled by strongly rate-weakening fault friction and Drucker-Prager viscoelasticity.

There are two more structural features of faults that must be taken into account, the geometrical complexities of faults at all scales and the three dimensionalities of faults and depth-dependent stress conditions associated with the dipping dimension. Duan and Day (2008) model an elastoplastic 2D in-plane strike slip fault with a bend, a kind of first-order fault geometrical complexities. Dunham et al. (2011a) take accounts of fault roughness, fault geometrical complexities at finer scales, and the strong rate-weakening friction. All the 2D in-plane models assume the fault be buried at a specific depth. Ma and Andrews (2010) simulate dynamic ruptures on a 3D planar strike slip fault subjected to depth-dependent initial stresses and pressure-dependent Drucker-Prager yield criterion. They explore the effects of cohesion in the yielding criterion on the distribution of off-fault inelastic zone. Different cohesions, especially the low one (5 MPa), mainly affect inelastic zone distributions at shallow depth because the cohesion has more weight in determining the yielding strength of rocks due to low confining pressure. A "flower-like" distribution of inelastic strain is formed, which expands dramatically near the free-surface. Inelastic response is restricted near the fault at depths. They apply beach balls in seismology that show fault mechanics to present the off-fault shear inelastic strain, interpreted as damage associated with dynamic ruptures that may involve mesoscale subsidiary faults and microcracks. They only model a condition where the maximum compressional principle stress has a 45˚ with respect to the fault strike. They find the orientations of the induced shear microcracks vary near the surface. Given the non-negligible structural features of fault geometrical complexity and its three dimensionalities, it is necessary 1) to evaluate the dynamic ruptures and associated off-fault inelastic distributions on a 3D fault with geometrical

complexities, for instance, a fault bend in this study, 2) to compare the orientations of shear inelastic strain interpreted from the numerical models to field geological observations of mesoscale subsidiary faults and microcracks, and 3) to infer stress states or histories of past earthquake slips around a fault bend based on features of such mesoscale subsidiary faults and microcracks.

We simulate dynamic ruptures on a 3D strike-slip fault with a bend. The medium is loaded with depth-dependent initial stresses and is controlled by the pressure-dependent Drucker-Prager yielding criterion. We present beach balls of the off-fault shear inelastic deformation at various depths near the fault bend. The model is conceptualized from the North Branch San Gabriel Fault (NBSGF), California, where a 13° change in strike takes place over 435 m (Becker, 2012). The right-lateral sense of shear of slip makes the north side of the fault is compressive and the south dilatational. We choose the NBSGF because thorough structural geological and petrological observations and analyses have been conducted with the off-fault damage, i.e., macro-, meso-, and micro- fractures associated with the localized bend (Becker, 2012). We make efforts to link the simulated off-fault plastic deformation to features of fractures from field observations, which helps constrain the numerical models and improves their credibility and predictivity.

4.2 Fault Geometry, Depth-dependent Stresses, and Friction Law

We simulate dynamic ruptures on a right-lateral 3D strike-slip fault with a bend as shown in Figure 4.1. The fault is embedded in a homogeneous half-space. The bend is defined as the structure where the change of fault strike occurs. The bend connects two 30-by-15-km vertical planar fault segments, noted as the left and the right segments in Figure 4.1. The strike of the right segment deviates 10° from the left one over one element, which is conceptualized from the

NBSGF. The bend differs from the smooth bend in Chapter II because of the observation that the NBSGF changes 13˚ over 435 m. The bend structure consists of the element where the change of strike takes place and the two adjacent elements. The compressional side and the dilatational side of the fault are also noted in Figure 4.1. The coordinate system has x direction along the strike of the left segment, y direction normal to the left segment, and z direction upright. The P-wave velocity, S-wave velocity, rock density ρ, and fluid density ρ_f are 6000 m/s, 3464 m/s, 2670 kg/m^3, and 1000 kg/m^3, respectively, as given in Table 4.1.

The initial stresses are depth dependent. Normal stress on the left segment and σ_{zz} is assumed as the lithostatic stress minus the hydrostatic pore pressure with the water table at the free surface. In our reference model, which has the same stress setup as that in Ma and Andrews (2010), $\sigma_{xx} = \sigma_{yy} = \sigma_{zz} = -(\rho - \rho_f)gz = -(16.37\ \mathrm{MPa/km})z$, where g=9.8m/s^2 is the gravitational acceleration. We assume the maximum compressive stress σ_1 has a $\theta = 45°$ with respect to the left segment as indicated in Figure 4.1a and the model is named as M45. Therefore, $\sigma_{xy} = 0.4\sigma_{xx}$, and $\sigma_{xz} = \sigma_{yz} = 0$. Because we will explore the effect of θ on off-fault inelastic strain, two other models with $\theta = 35°$ and $60°$ noted as M35 and M60 respectively, are designed. The numbers in the model names are values of θs. We default the earthquake nucleation on the left segment. Two other models, named as M35Nuc2 and M60Nuc2, are designed and they differ from M35 and M60 with the location of earthquake nucleation on the right segment.

In dynamic ruptures, the fault surface is governed by the slip-weakening law (e.g., Ida, 1972, Day, 1982), where the shear stress τ (or frictional coefficient μ) drops linearly over fault slip D_0 from the peak shear strength τ_s (or static friction μ_s) to frictional sliding stress τ_d (or dynamic sliding friction μ_d). A schematic plot of the law is shown in Figure 4.1b. We assume

$\mu_s = 0.6$ and $\mu_d = 0.3$ and $D_0 = 0.8\,m$ for M35 and M45. In M60, because of the high angle of σ_1 with respect to the fault strike, μ_s and μ_d are assigned low values and differently for the left and the right segment to ensure realistic rupture propagations. They are 0.45 and 0.15 for the left segment and 0.4 and 0.1 for the right segment, respectively. The dynamic friction coefficient is tapered linearly from μ_d to μ_s from z=-12 km to z=-15 km and from z=-3km to z=0km to cease the dynamic rupture smoothly when it approaches the bottom of the fault and the free surface, respectively.

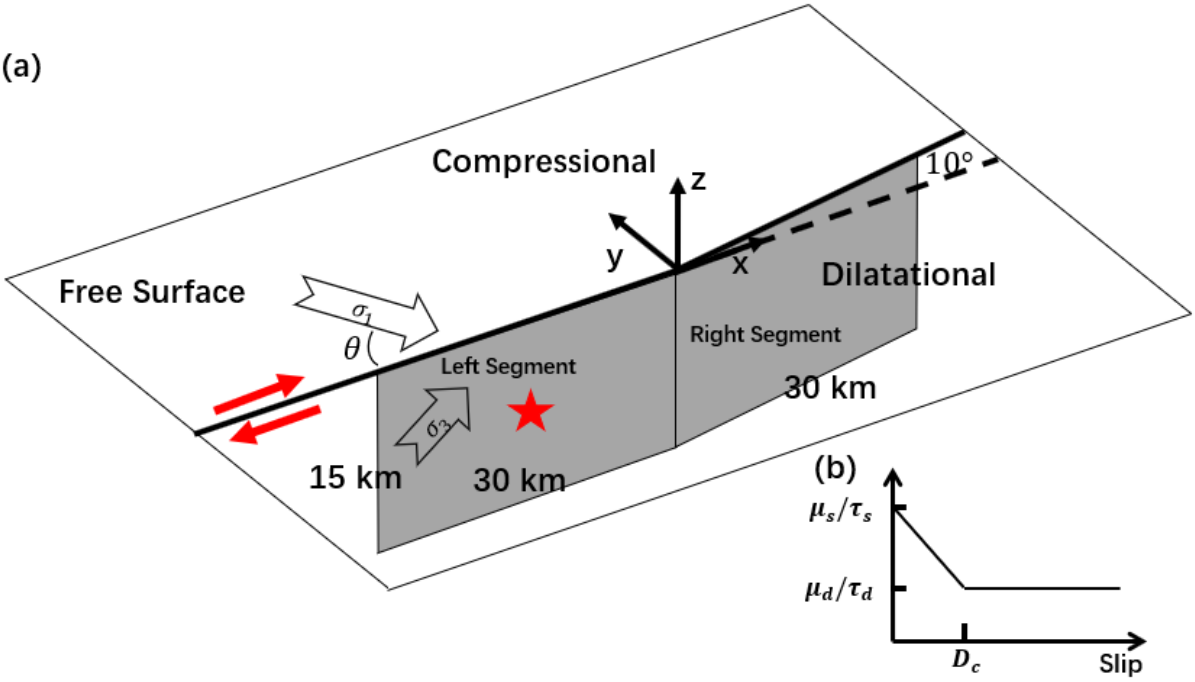

Figure 4.1 (a) Schematic of the fault geometry, dimensions, and the coordinate system. The left and the right segments are indicated in the figure. They strike at 0˚ and 10˚, respectively. The sense of shear is right-lateral. The maximum and minimum principle stresses are shown as σ_1 and σ_3, respectively. θ is the angle from the σ_1 to the strike of the left segment. (b) Demonstration of the slip-weakening law, where shear stress drops from the shear strength τ_s to the dynamic sliding stress τ_d linearly over the fault slip D_c. τ_s and τ_d can be replaced with μ_s and μ_d, respectively, if the shear stresses are denominated by the normal stress.

Table 4.1 Key parameters in models for the study of off-fault plasticity induced by a bend.

Physical quantities	Values
Fault length along the strike for the left segment	30 km
Fault length along the strike for the right segment	30/cos(10°) = 30.463 km
Fault depth	15 km
S wave velocity	3464 m/s
P wave velocity	6000 m/s
Density of rock	2670 kg/m^3
Density of fluid	1000 kg/m^3
Bulk modulus	0.75
Cohesion	2 MPa
Time elapse	0.06 s
Static friction μ_s [1]	0.6 (M35 and M45)/0.4 (M60's left segment)/0.45 (M60's right segment)
Dynamic sliding friction μ_d [1]	0.3 (M35 and M45)/0.1 (M60's left segment) / 0.15(M60's right segment)
Slid weakening distance	0.8 m
dt	0.008 s
Running time	30 s
dx	100 m

[1] For more details please see text section 4.1.

Table 4.2 Seismic ratio, S, on the left and right segments for various models.

Model Name	M35		M45		M60	
S	1.215	2	2	8.784	1.163	2.098

4.3 Drucker-Prager Plasticity and its Finite Element Implementation

We follow the schemes in Ma and Andrews (2010) to incorporate the Drucker-Prager Plasticity (Drucker and Prager, 1952) in the EQdyna (e.g., Duan and Oglesby, 2005, Duan, 2010, Kang and Duan, 2015, Liu and Duan, 2018, Harris et al., 2018a), a parallel Finite Element Software to efficiently simulate earthquake dynamic ruptures and wave propagation. The 3D version of EQdyna with Drucker-Prager plasticity has been used to study off-damage of low-velocity zone (Kang and Duan, 2015). We will lay out key equations and implementations of the Drucker-Prager Plasticity in the section.

$$\tau_v = \sqrt{0.5 s_{ij} s_{ij}} < -\left(\frac{\sigma_{kk}}{3}\right)\sin\phi + c\cos\phi = \tau_v^y,$$

Where s_{ij} is the deviatoric stress, τ_v is the square root of the second invariant of the deviatoric stress tensor and is considered as the measurement of the shear stress in 3D situation, c is the cohesion, ϕ is the internal frictional angle, τ_v^y is the yielding stress, and the repeated indices are summed up (Ma and Andrews, 2010). Following Ma and Andrews (2010), a scalar quantity η, which is the summation of absolute inelastic strain in each time step, is defined to evaluate the accumulated inelastic strain. It is calculated as,

$$\eta(t) = \int_0^t d\eta,$$

$$d\eta = \sqrt{0.5(d\varepsilon_{ij}^p - \delta_{ij} d\varepsilon_{kk}^p/3)(d\varepsilon_{ij}^p - \delta_{ij} d\varepsilon_{kk}^p/3)},$$

where $d\varepsilon_{ij}^{p}$ is the inelastic strain increment in each time step. As they point out, η is a better measurement of the inelastic deformation due to yielding because it does not decrease over time, while ε^{p} can decrease with time near the surface. No irrecoverable volumetric strain is assumed, therefore $\mathrm{d}\varepsilon_{kk}^{p} = 0$. $\tan\phi$ is chosen as 0.75, larger than the static friction of 0.6 to resemble the fault as a weak plane.

The whole Finite Element Model ranges from -40 to 40 km along x direction, from -40 to 41 km along the y direction, and from -35 to 0 km along the z direction. We pick out the normal stress σ_n and the static stress drop $\sigma_d = \mathrm{abs}\big((\mu_0 - \mu_d)\sigma_n\big)$ at x=-15 km and z=-7.5km, the center of the left segment to estimate the limit on element sizes that can resolve the cohesive zone in the rupture front. $\sigma_n = -124.4$ MPa and $\sigma_d = 12.4\,MPa$. According to equation (30a) in Day et al. (2005), $\Lambda_0 = C_1\mu^* D_0/(\tau_s - \tau_d)$, the cohesive zone width at zero rupture speed $\Lambda_0 = 304\,m$, given the constant $C_1 = 9\pi/32$, $D_0 = 0.8\,m$, and the shear modulus $\mu^* = 32GPa$. In addition, based on their equation (36), $\Lambda = 150$ m after a 15 km rupture propagating distance. Therefore, an element size dx that is less than 150 m is desired and we choose dx = 100 m in our simulations.

4.4 Results

4.4.1 Dynamic rupture propagation

Figure 4.2 show rupture time contours of the elastic model and the plastic model of the stress setup of M45, respectively. For every location on the fault, the rupture time is recorded as the time that the slip exceeds 0.001 m. Off-fault plasticity delays the rupture propagation where the inelastic strain occurs due to the dynamic rupture front. When the rupture enters the bend and the right segment, in the plastic model, the rupture only propagates at shallow depths (above 3 km depth) but stops at the bend at deep depths. The rupture of the elastic model has a further

reach into the right segment compared to that in the plastic model. The rupture speed in the plastic model is slower than that of the elastic model. The difference in the rupture patterns and the delay in rupture speed result from the severe inelastic deformation induced by the rupture entering the bend structure. The inelastic deformation takes some portion of energy off the rupture front. In both models, the right segment barely breaks because the stress excess, $\tau_s - \tau_0$, is much higher than the stress drop, $\tau_0 - \tau_d$, where τ_s, τ_0, τ_d are shear strength, initial shear stress and dynamic sliding shear stress, respectively. The seismic ratio, S, defined by $(\tau_s - \tau_0)/(\tau_0 - \tau_d)$ (Day, 1982) is used to measure whether a fault governed by the slip-weakening law is easy to break or not. Table 4.2 lists the S ratios for the left and right segments of M35, M45 and M60 calculated by stresses on the fault and frictional parameters. In M45, the S ratio on the left segment is 2, which facilitates rupture propagation, while it is 8.784 which impedes rupturing.

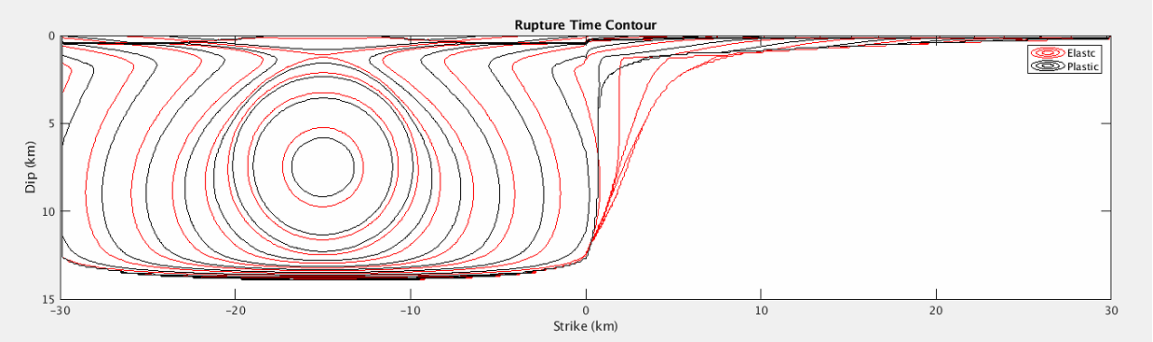

Figure 4.2 Rupture time contours of the elastic model and the plastic model of the stress setup of M45, respectively. Red and black contours are for the elastic and plastic model, respectively. The rupture of elastic model is faster than that of the plastic model. It also proceeds further than the plastic model into the bend and the right segment. Contour lines have an increment of 1 seconds.

4.4.2 Off-fault inelastic strains induced by the fault bend and their beach ball presentations

An important issue is how to present and interpret the off-fault inelastic strain. Templeton and Rice (2008) cite that materials such as rocks and soils exhibit pressure-dependent yielding in which the onset of plastic deformation depends on the mean normal stress at temperatures too low and/or timescales too short for creep. Inelastic deformation in brittle rocks under compressive stress occurs primarily as frictional sliding on fissure surfaces and microcracking. Duan and Day (2008) says that off-fault plastic yielding is used as an approximate continuum representation of the brittle damage mechanisms that dominate nonlinear deformation in the upper crust. Ma and Andrews (2010) cite that inelastic deformation under yielding implies frictional sliding on induced small shear microcracks.

Based on structure geological and petrological studies on fault damage zone, the inelastic deformation in numerical models should be associated with fractures at scales ranging from macroscopic subsidiary faults (shear fractures and small gouge zones), mesoscale fractures (subsidiary faults, fractures, veins) and shear microcracks (and/or opening cracks) (Becker, 2012). For mature, large displacement faults such as the NBSGF (16 – 20 km total displacement), the magnitude of damage is saturated (Becker, 2012), the off-fault inelastic strain computed in numerical models should be interpreted mainly as the reactivation of the existing fractures at various scales while to a less content by new fracture formation. We will show beach balls of inelastic strain tensors, whose trace is zero because of no volumetric strain, to illustrate orientations of the damage, i.e., reactivated/induced shear fractures and microcracks at various scales, associated with earthquake dynamic rupture near the fault bend. It is used in Ma and Andrews (2010). For simplicity, we will mention the reactivated/induced shear fractures at various scales as fractures in the following text.

We follow Ma and Andrews (2010)'s descriptions to find the orientations of the fractures and microcracks based on the beach balls of inelastic strain tensor. We summarize the process in three steps that read as follows: first, the maximum inelastic shear strain will be found in the plane perpendicular to the intermediate principal inelastic strain ε_2^p and at 45˚ with respect to the maximum (or minimum) principle inelastic strain ε_1^p and ε_3^p; second, the nodal planes of the beach balls coincide with directions of maximum inelastic shear strains; third, the orientations of induced shear fractures can be obtained by rotating about 15˚ from the nodal planes of the beach ball such that the compressional quadrants (white in the beach balls) shrink about 30˚ and the dilatational quadrants (red in the beach balls) expand about 30˚. The 15˚ arises from the internal friction $\tan\phi = 0.75$.

4.4.2.1 The distributions and magnitude of inelastic strain around the fault bend

Figure 4.3 show the magnitudes and spatial distributions of inelastic strain (larger than 0.0001) at various depth around the bend for M45. The inelastic strain shows a 'flower-like' distribution such that inelastic deformation occurs on both sides of the fault at the shallow 50 m depth. The range shrinks with increasing depth dramatically. The inelastic strain vanishes at 550 m depth on the compressional side of the fault. In terms of magnitude of inelastic strain, at depths above 550 m, the most severe inelastic strains occur on the dilatational side of the fault and is very close to the bend. The magnitude of inelastic strain on the compressional side of the fault are significantly less than their counterparts on the dilatational side. At deep depth below 550 m, the inelastic strain merely occurs on the dilatational side of the fault. With increasing depths, the area affected by inelastic strain shrinks but the maximum magnitude of inelastic strain increases. The results are caused by depth-dependent stress states and pressure-dependent Drucker-Prager yielding plasticity which increases the yielding strength at deeper depth.

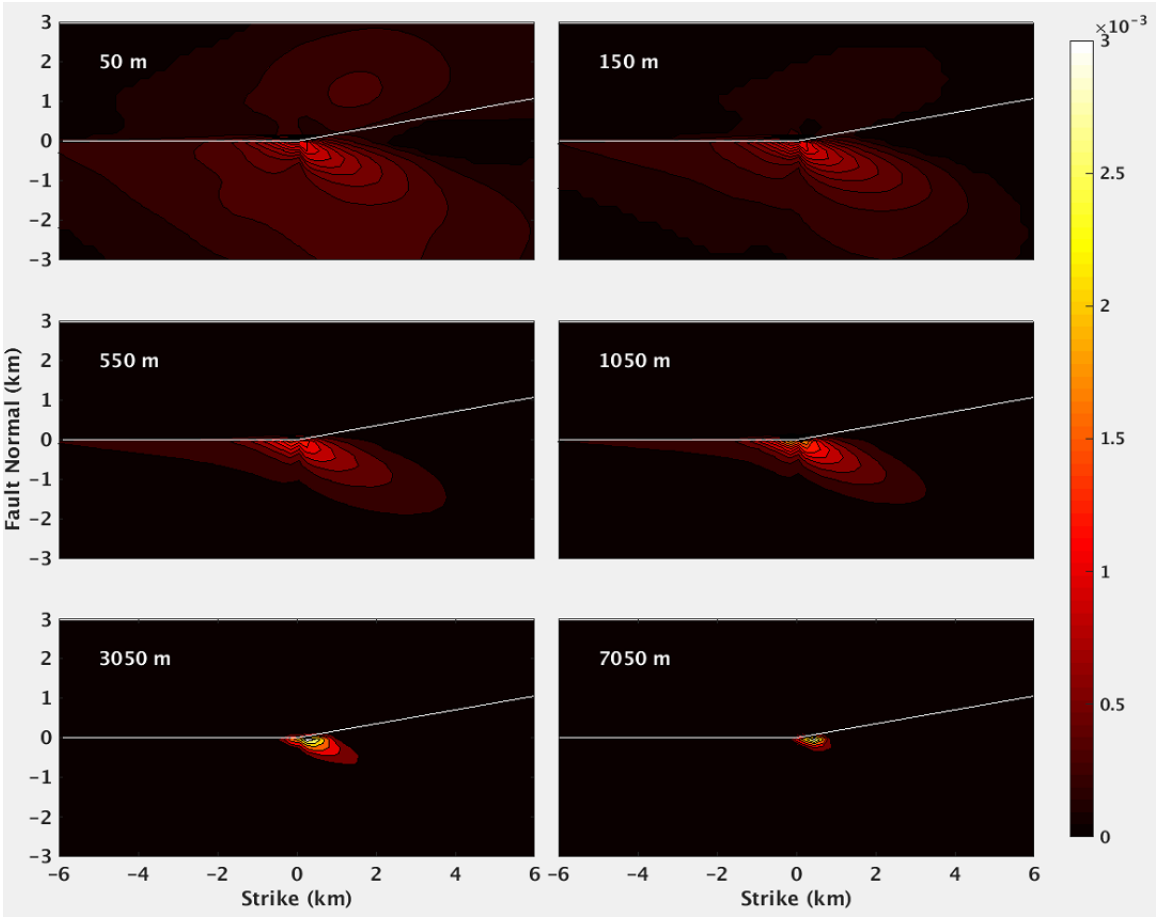

Figure 4.3 Distributions and magnitude of inelastic strain around the bend at 50, 150, 550, 1050, 3050, and 7050 m depths, respectively, for M45. Only inelastic strain that is larger than 0.0001 is shown. In shallow depths above 550m, the inelastic strain is distributed on both the compressional and dilatational side of the fault and is distributed in a wide region. In deep depths below 550 m, the inelastic strain is only distributed on the dilatational side of the fault. The area of inelastic strain shrinks when the depth goes deeper, while the magnitude of inelastic strain increases with depth. The distribution shows a 'flower-like' structure. It results from the depth-dependent stress states and pressure-dependent yielding strength of Drucker-Prager plasticity.

4.4.2.2 The orientations of inelastic strain

Figure 4.4 show us the orientations of inelastic strain tensors of M45 at 50 m depth near the bend using beach balls. In beach balls, the red quadrant is tensional, and the white quadrant is compressional. Following the three-step illustration, the nodal planes of the beach balls coincide

with the planes of maximum inelastic shear strains. The orientations of reactivated/induced shear fractures and microcracks will be rotated about 15˚ from the planes of maximum inelastic shear strains such that the compressional quadrant shrinks about 30˚ in total.

The reason we first present the results of M45 is that the rupture is terminated near the bend because of the high seismic ratio, S=8.784, on the right segment. Later we will see a big difference in the orientations of inelastic strain tensors near the bend in other models M35 and M60, in which ruptures continue through the bend. There are three regions of distinct orientations of inelastic strain as labeled. In region 1 on the compressional side of the fault, the fractures show a conjugate set of vertical shearing planes with the maximum principle inelastic strain perpendicular to the fault strike of the left segment. In region 2 on the dilatational side of the fault, still, a set of conjugate vertical planes is dominant, but the maximum principle inelastic strain is parallel to the fault strike. In region 3 on the dilatational side of the fault, a set of shear fractures that have high dip angles are presented, which indicates an upward pointing maximum principle inelastic strain. We notice the distribution of the third set of orientations ceases where the rupture terminates. It is expected that the third set of orientations will replace the second set of orientations on the dilatational side if the rupture is continued through the bend.

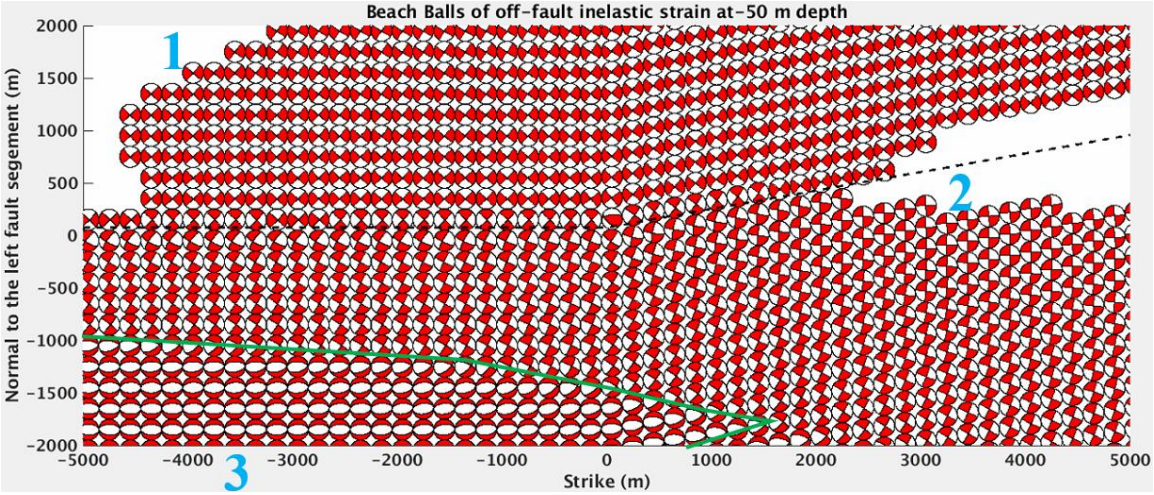

Figure 4.4 Beach ball presentations of inelastic strain tensors induced by the dynamic rupture of M45 near the fault bend at 50 m depth. The inelastic strain that is larger than 0.0001 is shown. The red quadrant is tensional, and the white quadrant is compressional. The nodal planes of the beach balls coincide with the directions of maximum inelastic shear strains. The orientation of reactivated/induced shear fractures and microcracks will be rotated about 15˚ from the maximum inelastic shear strains. Three distinct sets of orientations are identified and labeled.

Figure 4.5 (a) and (b) show beach ball presentations of inelastic strain tensors of M45 at depths of 350 and 3050 m, respectively. Consistent with Figure 4.3, the area of inelastic strain shrinks with the increasing depth and the inelastic strain only occurs on the dilatational side of the fault below 550 m depth. The orientations of the fractures are the same as those at 50 m depth. In other models M35 and M60 with ruptures through the bend, we'll see distinct subhorizontal orientations of fractures at very shallow depths, indicating the effect of dynamic ruptures passing by the fault bend.

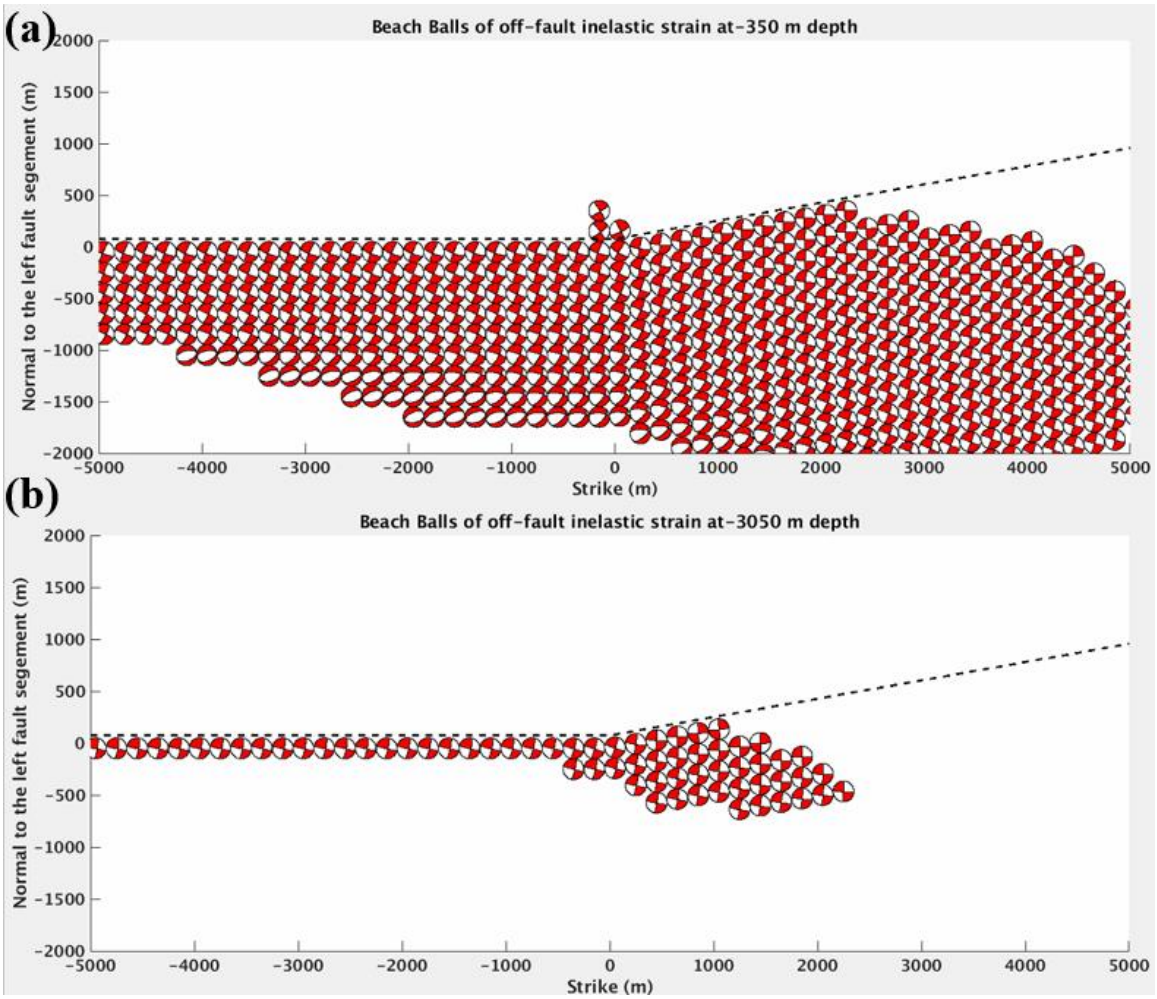

Figure 4.5 Beach ball presentations of inelastic strain tensors induced by the dynamic rupture near the fault bend at 350 m (a) and 3050 m depth (b) of M45, respectively. The inelastic strain that is larger than 0.0001 is shown. The red quadrant is tensional, and the white quadrant is compressional. Because the rupture stops at the fault bend, the orientations of the fractures do not change at various depth. In other models (M35 and M60) with fault ruptures continue through the bend, orientations of fractures show difference at shallow depth of a few hundreds of meters near the bend.

4.4.3 Subhorizontal off-fault shear fractures and their relation to the rupture direction and stress states

Templeton and Rice (2008) demonstrate that the angle from the maximum principle stress σ_1 to the fault strike will shape the spatial distribution of off-fault inelastic strain with their 2D in-plane models. Therefore, we rotate the direction of σ_1 to make $\theta = 35°$ and $60°$ for M35 and M60, respectively. In addition, we put locations of earthquake nucleation on the right segment, which yields two other models M35Nuc2 and M60Nuc2.

Two distinct features of this set of models where ruptures propagate through the fault bend is that 1) the generation of subhorizontal off-fault shear fractures, and 2) their locations depending on the direction of rupture propagation. As shown in the thorough analysis of orientations of mesoscale subsidiary faults and microcracks along the NBSGF and its bend (Becker, 2012), they find subhorizontal fractures existing on both sides of the fault bend with a concentration on the compressional side of the fault (north side).

Figure 4.6 shows the beach ball presentations of off-fault inelastic strain tensors around the bend in M35 (a) and M60 (b), respectively. Orientations of fractures are similar to those in M45 except some special beach balls existing exclusively on the compressional side of the fault as outlined by the black triangles. Following the procedure to shrink the compressional (white) quadrant of the beach ball by about 30˚, the beach balls will yield a set of subhorizontal fractures. By comparing Figure 4.6 (a) and (b), we notice the similarities between the orientations of fractures in the two models. It is because at the shallow depth of 50 m, the Drucker-Prager yielding criterion is mainly determined by the cohesion while the stress states play a less important role. As examined in Ma and Andrews (2010), the inelastic strain at such a depth is perturbed by passing seismic waves. Figure 4.7 shows that the ruptures of M35 and M60

resemble each other in terms of rupture time contours. Therefore, it is reasonable to expect a certain degree of similarities in the off-fault fractures between the two models at the very shallow depth.

The subhorizontal fractures vanish below 450 m depth (not shown). Hence, their occurrence is a feature at the very shallow depth.

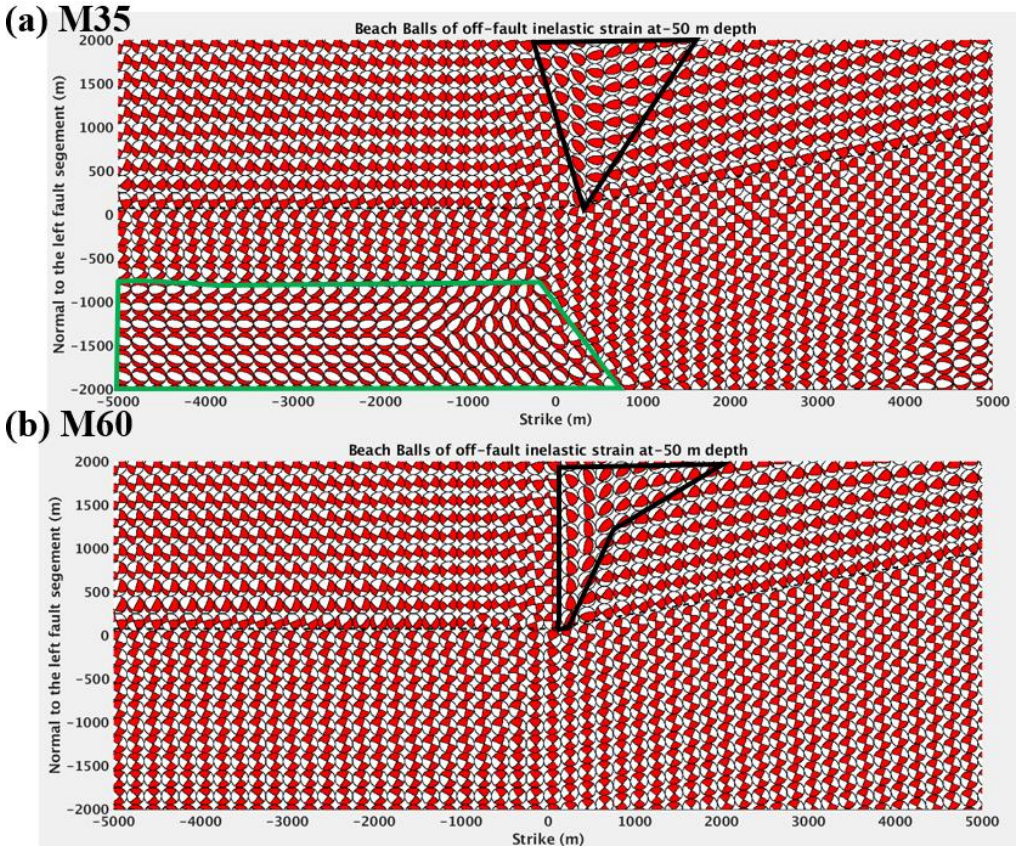

Figure 4.6 Beach ball presentations of inelastic strain tensors induced by the dynamic rupture of M35 (a) and M60 (b) near the fault bend at 50 m depth, respectively. The inelastic strain that is larger than 0.0001 is shown. The red quadrant is tensional, and the white quadrant is compressional. The nodal planes of the beach balls coincide with the directions of maximum inelastic shear strains. The orientation of reactivated/induced shear fractures and microcracks will be rotated about 15˚ from the maximum inelastic shear strains. A distinct set of subhorizontal fractures are outlined by triangles. They exclusively occur on the compressional side of the fault and are very close to the bend.

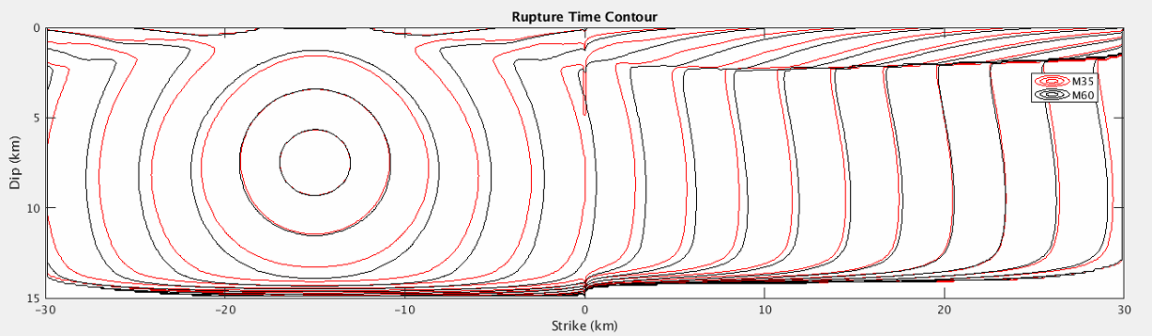

Figure 4.7 Rupture time contours of M35 and M60, respectively. The two ruptures mimic each other because of similar seismic ratio distributions as shown in Table 4.2.

Because the stress states do not have a big impact on the spatial distribution of the subhorizontal factures, we want to switch the location of earthquake nucleation to the right segment. Figure 4.8 shows the beach ball presentations of inelastic strain tensors at the 50 m depth of M35Nuc2 (a) and M60Nuc2 (b), respectively. As outlined by the black polygons, the locations of these subhorizontal fractures exist exclusively on the dilatational side of the fault and are close to the fault bend.

Therefore, we conclude that the off-fault subhorizontal fractures is the result of dynamic rupture through the fault bend and is a shallow depth feature where cohesion weights more than the mean stress in the Drucker-Prager Yielding criterion. Their location depends on the direction of rupture propagation.

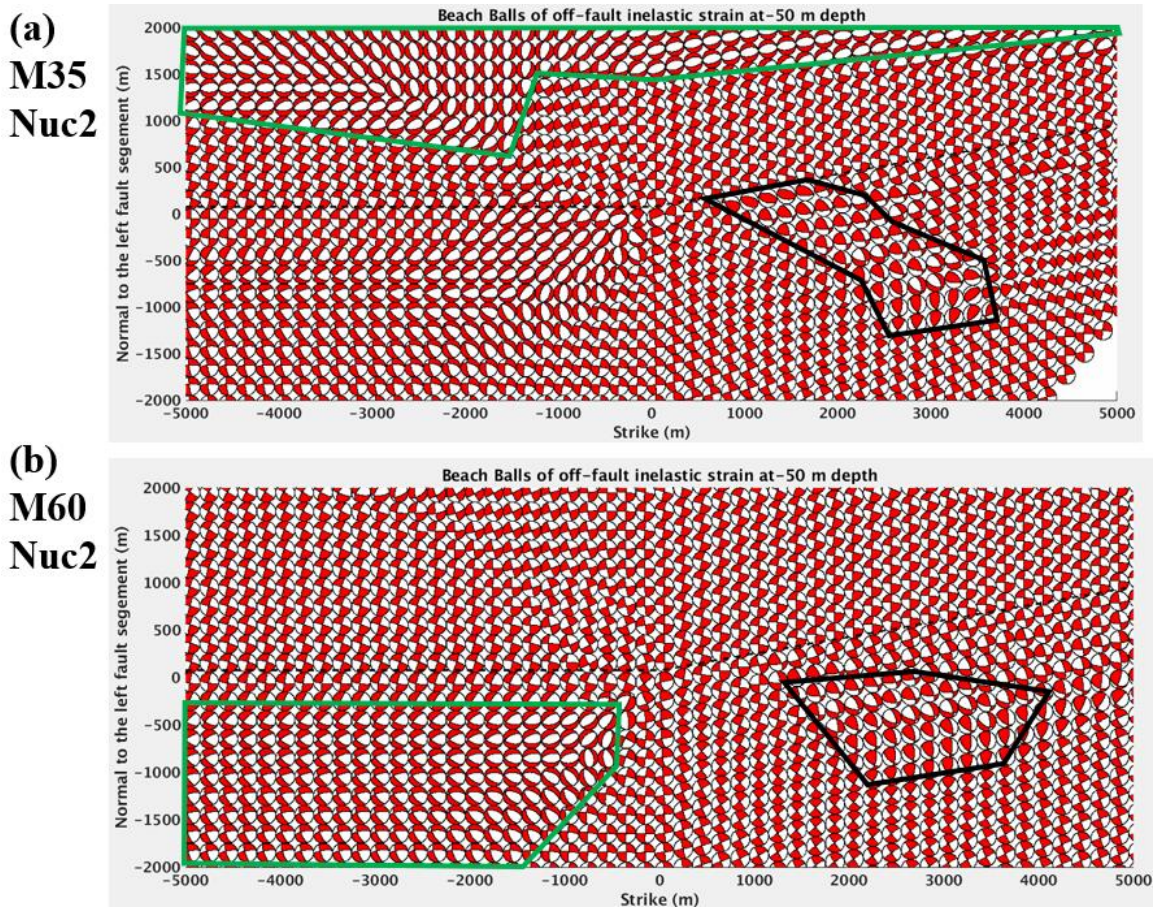

Figure 4.8 Beach ball presentations of inelastic strain tensors induced by the dynamic ruptures of M35Nuc2 (a) and M60Nuc2 (b) near the fault bend at 50 m depth, respectively. The nucleation starts on the right segment. The inelastic strain that is larger than 0.0001 is shown. The red quadrant is tensional, and the white quadrant is compressional. The nodal planes of the beach balls coincide with the directions of maximum inelastic shear strains. The orientation of reactivated/induced shear fractures and microcracks will be rotated about 15˚ from the maximum inelastic shear strains. A distinct set of subhorizontal fractures are outlined by black lines. They exclusively occur on the dilatational side of the fault and are close to the bend.

4.5 Discussion

An objective of the article is to find mechanical explanation to the abundant structure-geological observations of the fractures at various scales in the damage zone of the NBSGF and its bend (Becker, 2012). Becker (2012) concludes that the mesoscale subsidiary fault fabric and kinematics in the NBSGF damage zone within the fault bend region differ from those along

linear segments of the fault. There is a subhorizontal set of subsidiary faults present within the bend, which is significantly more prominent north of the fault than the south. In addition, the subhorizontal set is absent in all of the domains along the linear fault segments. A detailed examination of his data shows that within the bend, the set of subhorizontal subsidiary faults is more prominent while the normal poles of the set of subvertical subsidiary faults are a little scattered. Therefore, we focus mainly on explaining the more prominent presence of subhorizontal subsidiary faults north of the fault (on the compressional side of the fault) and its absent in the linear fault segments. Based on numerical results, the occurrence of subhorizontal orientations of inelastic strain tensors, i.e., fractures, is caused by the dynamic rupture through the fault bend at very shallow depths above 400 meters depth. The subhorizontal fractures exclusively occur near the bend and they are absent in the straight fault segments. The spatial distributions of such subhorizontal fractures depend on the direction of rupture propagation. In M35 and M60, where ruptures propagate from the left segment to the right segment, the subhorizontal fractures occur on the compressional side of the fault (the north side). In M35Nuc2 and M60Nuc2, where ruptures propagate from the right segment to the left one, the subhorizontal fractures exist only on the dilatational side of the fault (south side). Therefore, the observed more prominent concentration of subhorizontal subsidiary faults north of the NBSGF may indicate more ruptures through the fault bend from the west to the east in the long faulting history of the NBSGF.

Along linear fault segments, sets of conjugate strike-slip subsidiary faults and sets of subvertical subsidiary faults are common features in the numerical results, which are also reported in Becker (2012). However, because our focus in this article is near the fault bend and the locations to compare numerical results with field observations approaches the lateral ends of

the fault boundaries, which make the off-fault inelastic deformation affected by the stopping phase of dynamic ruptures, we don't proceed further to explain the results.

4.6 Conclusion

In this study, we simulate dynamic ruptures governed by the slip-weakening law on a 3D strike-slip fault with a bend of 10˚, which is conceptualized from the Northern Branch of San Gabriel Faults (NBSGF), where thorough field and petrological observations of mesoscale subsidiary faults and shear microcracks have been carried out. A depth-dependent regional stress is applied, and the rock yields based on the pressure-dependent Drucker-Prager criterion. Effects of the angle of maximum principle stress with respect to the fault strike and the direction of rupture propagation have been explored. The inelastic deformation in our models resembles reactivated/induced shear fractures at macro-, meso-, and micro- scales, i.e., damage of rocks, associated with dynamic ruptures. The zero-trace inelastic strain tensors are presented in the form of beach balls, whose nodal planes represent the maximum inelastic shear strain. The orientations of shear microcracks are about 15˚ from the nodal planes. We focus on the spatial distribution and the orientation of such inelastic strain near the fault bend. Major results are as below. 1) The numerical models confirm that dynamic ruptures through the bend will induce the prominent set of subhorizontal fractures at shallow depths, which exclusively occurs near the fault bend and are consistent with field observations made at the bend of NBSGF. 2) The direction of rupture propagation determines the locations of the subhorizontal fractures, whether occurring on the compressional or dilatational side of the fault. Based on the numerical results and observations at the NBSGF bend, the fault may experience more west-east ruptures in its history. Stress states play a minor role because of the negligible mean stress at the shallow depth. 3) The spatial distribution of off-fault inelastic strain shows 'flower-like' pattern. Inelastic strain

occurs widely at shallow depth with small magnitudes and it shrinks its range at deeper depth with higher magnitudes.

CHAPTER V

SUMMARY

The dissertation has been devoted to developments of numerical methodologies to simulate physical processes of various earthquake phenomena. We in detail explore three applications to earthquake cycles on geometrically complex faults, ground motion assessed from hypothetical scenario earthquakes in North China Basin, and off-fault damage associated with a fault bend and its linkage to structural-geological observations from Northern Branch of San Gabriel Fault.

In the first project, we develop a dynamic earthquake simulator based on finite element methods (FEM) to model dynamics of geometrically complex faults governed by the rate- and state- friction (RSF) over multiple earthquake cycles. The simulator combines a dynamic FEM code EQdyna and a newly developed static FEM code EQquasi to model quasi-static phases of earthquake nucleation, post-seismic and inter-seismic processes. Both FEM codes are parallelized through MPI to speed up computations. EQdyna and EQquasi exchange on-fault physical quantities including shear and normal stresses, slip-rates and state variables. The two-code scheme shows advantages to reconcile the computational challenges from different deformation phases of an earthquake cycle, which are mainly related to 1) handling time steps ranging from hundredths of a second to a few years based on the variable time stepping scheme and 2) the element size small enough to resolve the cohesive zone at the rupture front of dynamic ruptures. The dynamic earthquake simulator is different from most existing earthquake simulators in the community in the sense that it includes fully dynamic rupture propagation and can handle complex fault geometry. Earthquake cycles on a 3D strike-slip fault with a bend are simulated. The sizes of nucleation patches depend on the normal stress resolved from the

regional stress field and stress heterogeneities induced by previous ruptures near the bend. Complex earthquake event patterns are identified in the fault system.

In the second study, deterministic ground motions up to 0.5 Hz from a set of spontaneous dynamic ruptures of M_w 7.5 scenario earthquakes on a 160-km right-lateral seismic gap in North China Basin (NCB) have been simulated. Self-similar heterogeneous initial stresses on the fault and a high-resolution 3D velocity structure in NCB have been used. Self-similar stresses result in complex rupture behaviors such as jumped/triggered ruptures due to large stress variations. Sedimentary basin-induced waves contribute to these complex rupture behaviors when the fault passes through a basin. The directivity effect on peak ground velocity (PGV) is significantly reduced by self-similar heterogeneous stresses, because of frequent acceleration and deceleration of rupture fronts. Basin induced surface waves from the four bowl-shape basins in the study area amplify and prolongate ground motions, particularly within the one between Tianjin and Beijing.

In the last study, dynamic ruptures of a 3D strike-slip fault with a bend is simulated. Drucker-Prager plasticity is applied to model the off-fault damage associated with stress heterogeneity induced by dynamic ruptures through a fault bend. Off-fault plastic inelastic strain tensors are presented in the form of beach balls. Induced/reactivated shear mesoscale subsidiary faults and microcracks indicated by the beach balls are associated with observed orientations of such features in the Northern Branch of San Gabriel Fault. The numerical models confirm that dynamic ruptures through the bend will induce the prominent set of subhorizontal fractures at shallow depths, which exclusively occurs near the fault bend and are consistent with field observations made at the bend of Northern Branch of San Gabriel Fault. The direction of rupture propagation determines the locations of the subhorizontal fractures, whether occurring on the compressional or dilatational side of the fault. Based on the numerical results and observations at

the NBSGF bend, the fault may experience more west-east ruptures in its history. Pre-stress states play a minor role. The spatial distribution of off-fault inelastic strain shows ‘flower-like’ pattern. Inelastic strain occurs widely at shallow depth with small magnitudes and it shrinks its range at deeper depth with higher magnitude.

For the earthquake cycle simulator, our next step will be to implement domain decomposition methods in the EQquasi to scale up its computational ability and apply it to the Cajon Pass earthquake gate in southern San Andreas Fault, California. Also, because the emphasize of the first study is methodology and the Finite Element simulator, we’ll systematically explore other factors that affect multicycle dynamics of geometrically complex fault systems in the future. The factors may involve the bend angle, nucleation patch size, the angle between the principle stresses and the left segment, pore pressure change, etc. In terms of scenario earthquake ground motion simulation, we want to conduct more scenarios to yield more statistically robust relations of ground motion level v.s. the distance of a station off the fault, basin depth, and frequency, and compare the numerical results to existing empirical ground motion relations in the NCB if there is any. For the last study of off-fault damage associated with the fault bend, we plan to adjust key parameters such as bend angle, stress drop, and seismic ratio S to see their effects on the conclusion yielded in this study.

REFERENCES

Aagaard, B. T., Knepley, M. G. & Williams, C. A. 2013. A domain decomposition approach to implementing fault slip in finite-element models of quasi-static and dynamic crustal deformation. *Journal of Geophysical Research: Solid Earth,* 118**,** 3059-3079.

Amestoy, P. R., Duff, I. S., L'excellent, J.-Y. & Koster, J. 2001. A Fully Asynchronous Multifrontal Solver Using Distributed Dynamic Scheduling. *SIAM Journal on Matrix Analysis and Applications,* 23**,** 15-41.

Amestoy, P. R., Guermouche, A., L'excellent, J.-Y. & Pralet, S. 2006. Hybrid scheduling for the parallel solution of linear systems. *Parallel Computing,* 32**,** 136-156.

Andrews, D. J. 1980. A Stochastic Fault Model .1. Static Case. *Journal of Geophysical Research,* 85**,** 3867-3877.

Andrews, D. J. 1981. A stochastic fault model: 2. Time-dependent case. *Journal of Geophysical Research: Solid Earth,* 86**,** 10821-10834.

Andrews, D. J. 1989. Mechanics of fault junctions. *Journal of Geophysical Research: Solid Earth,* 94**,** 9389-9397.

Andrews, D. J. 2004. Rupture models with dynamically determined breakdown displacement. *Bulletin of the Seismological Society of America,* 94**,** 769-775.

Andrews, D. J. 2005. Rupture dynamics with energy loss outside the slip zone. *Journal of Geophysical Research,* 110.

Andrews, D. J. & Barall, M. 2011. Specifying Initial Stress for Dynamic Heterogeneous Earthquake Source Models. *Bulletin of the Seismological Society of America,* 101**,** 2408-2417.

Anooshehpoor, A. & Brune, J. N. 1994. Frictional heat generation and seismic radiation in a foam rubber model of earthquakes. *pure and applied geophysics,* 142**,** 735-747.

Becker, A. 2012. *Off-fault damage associated with a localized bend in the North Branch San Gabriel Fault, California.* M.S. Thesis, Texas A&M University.

Ben-Zion, Y. 1998. Properties of seismic fault zone waves and their utility for imaging low-velocity structures. *Journal of Geophysical Research-Solid Earth,* 103**,** 12567-12585.

Berenger, J.-P. 1994. A perfectly matched layer for the absorption of electromagnetic waves. *Journal of Computational Physics,* 114**,** 185-200.

Biasi, G. P. & Wesnousky, S. G. 2016. Steps and Gaps in Ground Ruptures: Empirical Bounds on Rupture Propagation. *Bulletin of the Seismological Society of America*.

Biasi, G. P. & Wesnousky, S. G. 2017. Bends and Ends of Surface Ruptures. *Bulletin of the Seismological Society of America,* 107**,** 2543-2560.

Bielak, J., Graves, R. W., Olsen, K. B., Taborda, R., Ramirez-Guzman, L., Day, S. M., Ely, G. P., Roten, D., Jordan, T. H., Maechling, P. J., Urbanic, J., Cui, Y. F. & Juve, G. 2010. The ShakeOut earthquake scenario: Verification of three simulation sets. *Geophysical Journal International,* 180**,** 375-404.

Brocher, T. A. 2005. Empirical relations between elastic wavespeeds and density in the earth's crust. *Bulletin of the Seismological Society of America,* 95**,** 2081-2092.

Caine, J. S., Evans, J. P. & Forster, C. B. 1996. Fault zone architecture and permeability structure. *Geology,* 24**,** 1025-1028.

Chester, F. M. & Chester, J. S. 1998. Ultracataclasite structure and friction processes of the Punchbowl fault, San Andreas system, California. *Tectonophysics,* 295**,** 199-221.

Chester, F. M., Evans, J. P. & Biegel, R. L. 1993. Internal structure and weakening mechanisms of the San Andreas Fault. *Journal of Geophysical Research: Solid Earth,* 98**,** 771-786.
Collino, F. & Tsogka, C. 2001. Application of the perfectly matched absorbing layer model to the linear elastodynamic problem in anisotropic heterogeneous media. *Geophysics,* 66**,** 294-307.
Day, S. M. 1982. Three-dimensional simulation of spontaneous rupture: the effect of nonuniform prestress. *Bulletin of the Seismological Society of America,* 72**,** 1881-1902.
Day, S. M. 1998. Efficient simulation of constant Q using coarse-grained memory variables. *Bulletin of the Seismological Society of America,* 88**,** 1051-1062.
Day, S. M., Dalguer, L. A., Lapusta, N. & Liu, Y. 2005. Comparison of finite difference and boundary integral solutions to three-dimensional spontaneous rupture. *Journal of Geophysical Research,* 110.
Day, S. M. & Ely, G. P. 2002. Effect of a Shallow Weak Zone on Fault Rupture: Numerical Simulation of Scale-Model Experiments. *Bulletin of the Seismological Society of America,* 92**,** 3022-3041.
Day, S. M., Gonzalez, S. H., Anooshehpoor, R. & Brune, J. N. 2008a. Scale-Model and Numerical Simulations of Near-Fault Seismic Directivity. *Bulletin of the Seismological Society of America,* 98**,** 1186-1206.
Day, S. M., Graves, R., Bielak, J., Dreger, D., Larsen, S., Olsen, K. B., Pitarka, A. & Ramirez-Guzman, L. 2008b. Model for basin effects on long-period response spectra in southern California. *Earthquake Spectra,* 24**,** 257-277.
Day, S. M. & Minster, J. B. 1984. Numerical simulation of attenuated wavefields using a Padé approximant method. *Geophysical Journal International,* 78**,** 105-118.
Dieterich, J. H. 1979. Modeling of Rock Friction .1. Experimental Results and Constitutive Equations. *Journal of Geophysical Research,* 84**,** 2161-2168.
Drucker, D. C. & Prager, W. 1952. Soil Mechanics and Plastic Analysis or Limit Design. *Quarterly of Applied Mathematics,* 10**,** 157-165.
Duan, B. 2010. Role of initial stress rotations in rupture dynamics and ground motion: A case study with implications for the Wenchuan earthquake. *Journal of Geophysical Research,* 115.
Duan, B. 2012. Dynamic rupture of the 2011 Mw 9.0 Tohoku-Oki earthquake: Roles of a possible subducting seamount. *Journal of Geophysical Research,* 117.
Duan, B. & Day, S. M. 2008. Inelastic strain distribution and seismic radiation from rupture of a fault kink. *Journal of Geophysical Research,* 113.
Duan, B., Liu, D. & Yin, A. 2017. Seismic shaking in the North China Basin expected from ruptures of a possible seismic gap. *Geophysical Research Letters,* 44**,** 4855-4862.
Duan, B. & Oglesby, D. D. 2005. Multicycle dynamics of nonplanar strike‐slip faults. *Journal of Geophysical Research: Solid Earth (1978–2012),* 110.
Duan, B. & Oglesby, D. D. 2006. Heterogeneous fault stresses from previous earthquakes and the effect on dynamics of parallel strike‐slip faults. *Journal of Geophysical Research,* 111.
Duan, B. & Oglesby, D. D. 2007. Nonuniform prestress from prior earthquakes and the effect on dynamics of branched fault systems. *Journal of Geophysical Research,* 112.
Dunham, E. M., Belanger, D., Cong, L. & Kozdon, J. E. 2011a. Earthquake Ruptures with Strongly Rate-Weakening Friction and Off-Fault Plasticity, Part 1: Planar Faults. *Bulletin of the Seismological Society of America,* 101**,** 2296-2307.

Dunham, E. M., Belanger, D., Cong, L. & Kozdon, J. E. 2011b. Earthquake Ruptures with Strongly Rate-Weakening Friction and Off-Fault Plasticity, Part 2: Nonplanar Faults. *Bulletin of the Seismological Society of America,* 101**,** 2308-2322.

Erickson, B. A. & Day, S. M. 2016. Bimaterial effects in an earthquake cycle model using rate-and-state friction. *Journal of Geophysical Research: Solid Earth,* 121**,** 2480-2506.

Festa, G. & Nielsen, S. 2003. PML absorbing boundaries. *Bulletin of the Seismological Society of America,* 93**,** 891-903.

Graves, R. W. 1995. Preliminary analysis of long‐period basin response in the Los Angeles Region from the 1994 Northridge Earthquake. *Geophysical research letters,* 22**,** 101-104.

Graves, R. W. & Day, S. M. 2003. Stability and accuracy analysis of coarse-grain viscoelastic simulations. *Bulletin of the Seismological Society of America,* 93**,** 283-300.

Graves, R. W., Pitarka, A. & Somerville, P. G. 1998. Ground-motion amplification in the Santa Monica area: Effects of shallow basin-edge structure. *Bulletin of the Seismological Society of America,* 88**,** 1224-1242.

Guatteri, M. & Spudich, P. 2000. What Can Strong-Motion Data Tell Us about Slip-Weakening Fault-Friction Laws? *Bulletin of the Seismological Society of America,* 90**,** 98-116.

Hanks, T. C. & Bakun, W. H. 2002. A bilinear source-scaling model for M-log A observations of continental earthquakes. *Bulletin of the Seismological Society of America,* 92**,** 1841-1846.

Hanks, T. C. & Bakun, W. H. 2008. M-logA Observations for Recent Large Earthquakes. *Bulletin of the Seismological Society of America,* 98**,** 490-494.

Harris, R. A., Barall, M., Aagaard, B., Ma, S., Roten, D., Olsen, K., Duan, B., Liu, D., Luo, B., Bai, K., Ampuero, J. P., Kaneko, Y., Gabriel, A. A., Duru, K., Ulrich, T., Wollherr, S., Shi, Z., Dunham, E., Bydlon, S., Zhang, Z., Chen, X., Somala, S. N., Pelties, C., Tago, J., Cruz‐Atienza, V. M., Kozdon, J., Daub, E., Aslam, K., Kase, Y., Withers, K. & Dalguer, L. 2018a. A Suite of Exercises for Verifying Dynamic Earthquake Rupture Codes. *Seismological Research Letters,* 89**,** 1146-1162.

Harris, R. A., Barall, M., Aagaard, B., Ma, S., Roten, D., Olsen, K., Duan, B., Luo, B., Liu, D., Bai, K., Ampuero, J., Kaneko, Y., Gabriel, A., Duru, K., Ulrich, T., Wollherr, S., Shi, Z., Dunham, E., Bydlon, S., Zhang, Z., Chen, X., Somala, S., Pelties, C., Tago, J., Cruz-Atienza, V., Kozdon, J., Daub, E., Aslam, K., Kase, Y., Withers, K. & Dalguer, L. 2018b. A suite of exercises for verifying dynamic earthquake rupture codes. *Seismological Research Letters*.

Harris, R. A., Barall, M., Andrews, D. J., Duan, B., Ma, S., Dunham, E. M., Gabriel, A.-A., Kaneko, Y., Kase, Y., Aagaard, B. T., Oglesby, D. D., Ampuero, J.-P., Hanks, T. C. & Abrahamson, N. 2011. Verifying a Computational Method for Predicting Extreme Ground Motion. *Seismological Research Letters,* 82**,** 638-644.

Harris, R. A., Barall, M., Archuleta, R., Dunham, E., Aagaard, B., Ampuero, J. P., Bhat, H., Cruz-Atienza, V., Dalguer, L., Dawson, P., Day, S., Duan, B., Ely, G., Kaneko, Y., Kase, Y., Lapusta, N., Liu, Y., Ma, S., Oglesby, D., Olsen, K., Pitarka, A., Song, S. & Templeton, E. 2009. The SCEC/USGS Dynamic Earthquake Rupture Code Verification Exercise. *Seismological Research Letters,* 80**,** 119-126.

Harris, R. A. & Day, S. M. 1993. Dynamics of fault interaction: parallel strike-slip faults. *Journal of Geophysical Research,* 98**,** 4461.

Herrmann, R. B. 2013. Computer Programs in Seismology: An Evolving Tool for Instruction and Research. *Seismological Research Letters,* 84**,** 1081-1088.

Ida, Y. 1972. Cohesive force across the tip of a longitudinal-shear crack and Griffith's specific surface energy. *Journal of Geophysical Research,* 77**,** 3796-3805.
Kang, J. & Duan, B. 2015. Elastic and inelastic responses of compliant fault zones to nearby earthquakes in three dimensions: a parameter-space study. *Geophysical Journal International,* 201**,** 1195-1214.
Kawase, H. 1996. The Cause of the Damage Belt in Kobe: "The Basin-Edge Effect," Constructive Interference of the Direct S-Wave with the Basin-Induced Diffracted/Rayleigh Waves. *Seismological Research Letters,* 67**,** 25-34.
Kawase, H. 2003. Site effects on strong ground motions. *International Geophysics Series,* 81**,** 1013-1030.
Kawase, H. & Aki, K. 1989. A Study on the Response of a Soft Basin for Incident S-Waves, P-Waves and Rayleigh-Waves with Special Reference to the Long Duration Observed in Mexico-City. *Bulletin of the Seismological Society of America,* 79**,** 1361-1382.
Kosloff, D. & Frazier, G. A. 1978. Treatment of Hourglass Patterns in Low Order Finite-Element Codes. *International Journal for Numerical and Analytical Methods in Geomechanics,* 2**,** 57-72.
Lapusta, N. & Liu, Y. 2009. Three-dimensional boundary integral modeling of spontaneous earthquake sequences and aseismic slip. *Journal of Geophysical Research: Solid Earth,* 114.
Lapusta, N., Rice, J. R., Ben-Zion, Y. & Zheng, G. 2000. Elastodynamic analysis for slow tectonic loading with spontaneous rupture episodes on faults with rate- and state-dependent friction. *Journal of Geophysical Research: Solid Earth,* 105**,** 23765-23789.
Lavallee, D., Liu, P. C. & Archuleta, R. J. 2006. Stochastic model of heterogeneity in earthquake slip spatial distributions. *Geophysical Journal International,* 165**,** 622-640.
Liu, C., Zhu, B. & Shi, Y. 2016. Lithospheric rheology and Moho upheaval control the generation mechanism of the intraplate earthquakes in the North China Basin. *Journal of Asian Earth Sciences,* 121**,** 153-164.
Liu, D. & Duan, B. 2018. Scenario Earthquake and Ground‐Motion Simulations in North China: Effects of Heterogeneous Fault Stress and 3D Basin Structure. *Bulletin of the Seismological Society of America*.
Liu, H., Housner, G. W., Xie, L. & He, D. 2002. The Great Tangshan Earthquake of 1976.
Liu, P. C. & Archuleta, R. J. 2006. Efficient modeling of Q for 3D numerical simulation of wave propagation. *Bulletin of the Seismological Society of America,* 96**,** 1352-1358.
Liu, Q. H. & Tao, J. P. 1997. The perfectly matched layer for acoustic waves in absorptive media. *Journal of the Acoustical Society of America,* 102**,** 2072-2082.
Lozos, J. C., Oglesby, D. D., Duan, B. C. & Wesnousky, S. G. 2011. The Effects of Double Fault Bends on Rupture Propagation: A Geometrical Parameter Study. *Bulletin of the Seismological Society of America,* 101**,** 385-398.
Luo, B. & Duan, B. 2018. Dynamics of Nonplanar Thrust Faults Governed by Various Friction Laws. *Journal of Geophysical Research: Solid Earth,* 123**,** 5147-5168.
Ma, S. & Andrews, D. J. 2010. Inelastic off-fault response and three-dimensional dynamics of earthquake rupture on a strike-slip fault. *Journal of Geophysical Research-Solid Earth,* 115.
Ma, S. & Liu, P. C. 2006. Modeling of the perfectly matched layer absorbing boundaries and intrinsic attenuation in explicit finite-element methods. *Bulletin of the Seismological Society of America,* 96**,** 1779-1794.

Mai, P. M. & Beroza, G. C. 2002. A spatial random field model to characterize complexity in earthquake slip. *Journal of Geophysical Research,* 107.

Narayan, J. P. 2012. Effects of P-Wave and S-Wave Impedance Contrast on the Characteristics of Basin Transduced Rayleigh Waves. *Pure and Applied Geophysics,* 169**,** 693-709.

Oglesby, D. 2008. Rupture Termination and Jump on Parallel Offset Faults. *Bulletin of the Seismological Society of America,* 98**,** 440-447.

Oglesby, D. D. & Day, S. M. 2002. Stochastic fault stress: Implications for fault dynamics and ground motion. *Bulletin of the Seismological Society of America,* 92**,** 3006-3021.

Olsen, K. B. 1997. Three-Dimensional Dynamic Simulation of the 1992 Landers Earthquake. *Science,* 278**,** 834-838.

Olsen, K. B., Day, S. M. & Bradley, C. R. 2003. Estimation of Q for long-period (> 2 sec) waves in the Los Angeles basin. *Bulletin of the Seismological Society of America,* 93**,** 627-638.

Olsen, K. B., Day, S. M., Dalguer, L. A., Mayhew, J., Cui, Y., Zhu, J., Cruz-Atienza, V. M., Roten, D., Maechling, P., Jordan, T. H., Okaya, D. & Chourasia, A. 2009. ShakeOut-D: Ground motion estimates using an ensemble of large earthquakes on the southern San Andreas fault with spontaneous rupture propagation. *Geophysical Research Letters,* 36.

Olsen, K. B., Day, S. M., Minster, J. B., Cui, Y., Chourasia, A., Okaya, D., Maechling, P. & Jordan, T. 2008. TeraShake2: Spontaneous Rupture Simulations of Mw 7.7 Earthquakes on the Southern San Andreas Fault. *Bulletin of the Seismological Society of America,* 98**,** 1162-1185.

Oskin, M. E., Elliott, A. J., Duan, B., Liu-Zeng, J., Liu, Z., Shao, Y., Prush, V., Morelan, A., Chester, J. S. & Elizondo, D. 2015. Earthquake Gates: Linking Rupture Length To Geologically Constrained Dynamics of Fault Complexity, with Examples from the Altyn Tagh and San Andreas Faults.

Petra, C. G., Schenk, O. & Anitescu, M. 2014a. Real-Time Stochastic Optimization of Complex Energy Systems on High-Performance Computers. *Computing in Science & Engineering,* 16**,** 32-42.

Petra, C. G., Schenk, O., Lubin, M. & Gäertner, K. 2014b. An Augmented Incomplete Factorization Approach for Computing the Schur Complement in Stochastic Optimization. *SIAM Journal on Scientific Computing,* 36**,** C139-C162.

Pitarka, A., Dalguer, L. A., Day, S. M., Somerville, P. G. & Dan, K. 2009. Numerical Study of Ground-Motion Differences between Buried-Rupturing and Surface-Rupturing Earthquakes. *Bulletin of the Seismological Society of America,* 99**,** 1521-1537.

Pitarka, A., Irikura, K., Iwata, T. & Sekiguchi, H. 1998. Three-dimensional simulation of the near-fault ground motion for the 1995 Hyogo-ken Nanbu (Kobe), Japan, earthquake. *Bulletin of the Seismological Society of America,* 88**,** 428-440.

Rojas, O., Dunham, E. M., Day, S. M., Dalguer, L. A. & Castillo, J. E. 2009. Finite difference modelling of rupture propagation with strong velocity-weakening friction. *Geophysical Journal International,* 179**,** 1831-1858.

Romanowicz, B. 1992. Strike-slip earthquakes on quasi-vertical transcurrent faults: Inferences for general scaling relations. *Geophysical Research Letters,* 19**,** 481-484.

Ruina, A. 1983. Slip Instability and State Variable Friction Laws. *Journal of Geophysical Research,* 88**,** 359-370.

Sato, T., Graves, R. W. & Somerville, P. G. 1999. Three-dimensional finite-difference simulations of long-period strong motions in the Tokyo metropolitan area during the

1990 Odawara earthquake (MJ 5.1) and the great 1923 Kanto earthquake (MS 8.2) in Japan. *Bulletin of the Seismological Society of America,* 89**,** 579-607.
Scholz, C. H. 1998. Earthquakes and friction laws. *Nature,* 391**,** 37-42.
Scholz, C. H. 2002. *The mechanics of earthquakes and faulting*, Cambridge university press.
Somerville, P. 2006. Review of magnitude-area scaling of crustal earthquakes. *Rep. to WGCEP,* 22.
Somerville, P., Irikura, K., Graves, R., Sawada, S., Wald, D., Abrahamson, N., Iwasaki, Y., Kagawa, T., Smith, N. & Kowada, A. 1999. Characterizing Crustal Earthquake Slip Models for the Prediction of Strong Ground Motion. *Seismological Research Letters,* 70**,** 59-80.
Somerville, P. G., Smith, N. F., Graves, R. W. & Abrahamson, N. A. 1997. Modification of Empirical Strong Ground Motion Attenuation Relations to Include the Amplitude and Duration Effects of Rupture Directivity. *Seismological Research Letters,* 68**,** 199-222.
Templeton, E. L. & Rice, J. R. 2008. Off-fault plasticity and earthquake rupture dynamics: 1. Dry materials or neglect of fluid pressure changes. *Journal of Geophysical Research-Solid Earth,* 113.
Tse, S. T. & Rice, J. R. 1986. Crustal Earthquake Instability in Relation to the Depth Variation of Frictional Slip Properties. *Journal of Geophysical Research-Solid Earth and Planets,* 91**,** 9452-9472.
Wei, W., Ye, G., Jin, S., Deng, M. & Jing, J. 2007. Three Dimensional P-Wave Velocity Structure of the Crust of North China. *Earth Sci. J. China Univ. Geosci.,* 32**,** 441-452.
Wesnousky, S. G. 2006. Predicting the endpoints of earthquake ruptures. *Nature,* 444**,** 358-360.
Wesnousky, S. G. 2008. Displacement and geometrical characteristics of earthquake surface ruptures: Issues and implications for seismic-hazard analysis and the process of earthquake rupture. *Bulletin of the Seismological Society of America,* 98**,** 1609-1632.
Yang, F. & Huang, J. L. 2013. High precision 3D P-wave velocity model of the upper crust under the Chinese captial region based on oil seismic stack velocity and deep seismic sounding. *Chinese Journal of Geophysics* 56**,** 1487-1496.
Yin, A., Yu, X., Shen, Z. K. & Liu-Zeng, J. 2014. A possible seismic gap and high earthquake hazard in the North China Basin. *Geology,* 43**,** 19-22.

APPENDIX A

VALIDATION OF NUMERICAL IMPLEMENTATIONS OF COARSE-GRAINED Q MODELING AND PERFECTLY MATCHED LAYER ABSORBING BOUNDARY

The implementation of coarse-grained Q modeling is validated against the same benchmark problem in Ma and Liu (2006). A double-couple point source is located at (0, 0, 2) km in a Cartesian coordinate system (x, y, z) with positive z downwards. The double couple source has a strike (along x) of 90°; a dip of 90° and a rake of 0°. The moment rate function is given by $\dot{M}(t) = (M_0/T)(1 - \cos(2\pi t/T))$, when $0 \le t \le T$. Otherwise $\dot{M}(t) = 0$. $T = 0.2\ s$. The model consists of two layers. The top layer is 1 km thick. Its density, Vp, Vs, Qp and Qs are 2600 kg/m^3, 2800 m/s, 1500 m/s, 20 and 10, respectively. The bottom layer has density, VP, Vs, Qp and Qs of 2700 kg/m^3, 6000 m/s, 3464 m/s, 100 and 50, respectively. The station is on the free surface at coordinates of (8, 6, 0) km. The model is constructed by uniform hexahedron elements with the edges of 100-m long. The analytical Green function is calculated using the computer software for seismology (CPS) (Herrmann, 2013). Both the simulated and analytical results are filtered by a 4th-order Butterworth filter with a cutoff frequency of 3 Hz.

Figure A1 shows the comparison of the radial, transverse and vertical velocity synthetics between the simulation of EQdyna and the analytical solution from CPS. The good match of peaks and troughs indicate the correctness and robustness of the numerical implementation of coarse-grained Q modeling.

The dimensions of our finite element model are 20 km along x and y, and 12 km along z. Based on the faster Vp of 6000 m/s in the model, reflections from boundaries would be expected in less than 3 s in the simulation without PML. We run the simulation up to 20 s and no observable reflections can be seen, indicating that PML has been successfully implemented.

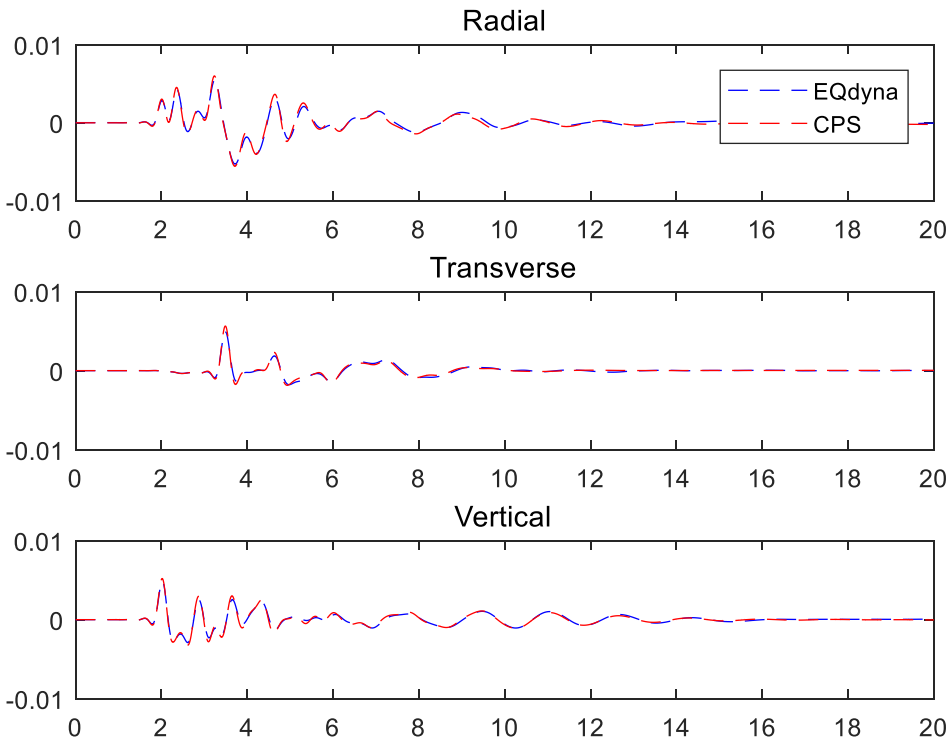

Figure A.1 Comparisons of radial, transverse and vertical velocity synthetics from EQdyna with coarse-grained Q modeling and PML to those computed by CPS. The good match of peaks and troughs indicate the correctness and robustness of the numerical implementation of coarse-grained Q modeling. No reflections from the model boundaries in the seismograms suggest the correct implementation of PML. The results are low-pass filtered below 3 Hz. The unit of velocity synthetics is m/sec.